THESIS FOR THE DEGREE OF DOCTOR OF PHILOSOPHY

in

Thermo and Fluid Dynamics

Studies on Diesel sprays under non-reacting and reacting conditions

CHENGJUN DU

Department of Mechanics and Maritime Sciences
CHALMERS UNIVERSITY OF TECHNOLOGY
Gothenburg, Sweden, 2017

Studies on Diesel sprays under non-reacting and reacting conditions

CHENGJUN DU
ISBN 978-91-7597-629-7

Doktorsavhandlingar vid Chalmers tekniska högskola
Ny serie nr 4310
ISSN: 0346-718X

Department of Mechanics and Maritime Sciences
Chalmers University of Technology
SE-412 96 Gothenburg
Sweden
Telephone +46 (0)31 7721000

Chalmers Reproservice
Gothenburg, Sweden 2017

더 좋은 세상 그리고 삶을 위하여

Abstract

Methods for reducing engine-out emissions are urgently needed to mitigate climate change and air pollution. In diesel engines, the quality of fuel-air mixing and the subsequent combustion process strongly affect fuel efficiency and engine-out emissions. However, fuel-air mixing, the subsequent combustion processes, and their dependence on the operating conditions are not yet fully understood. This thesis aims to address this deficiency by analyzing the effects of various orifice geometries and high injection pressures on the characteristics of diesel sprays.

The thesis briefly reviews the fundamental physics governing the flow of pressurized fuel through the internal nozzle of a diesel injector, the subsequent formation of the liquid and vapor spray, and the turbulent diffusion combustion processes. The experimental work presented in this thesis can be divided into three main parts. The first focuses on the effects of geometry-induced cavitation on the liquid/vapor phase spray and injection rate evaluation. To this end, a light absorption and scattering technique (LAS) was used to measure the distributions of liquid and vapor sprays formed using nozzles with various geometries. It was found that the vaporization of the diesel spray was controlled by turbulent air mixing. The effects of geometry-induced cavitation on the spray properties were mainly due to differences in the fuel mass flow rate, spray momentum and spreading angle. In addition, the injection rates of cavitating and non-cavitating nozzles were evaluated using the momentum flux measurement method. It was found that failure to account for cavitation caused the injection rate to be overestimated for the cavitating nozzle but not for the non-cavitating nozzle.

The second part of the experimental campaign investigates the effect of the injection pressure and nozzle geometry on soot formation and oxidation. A two-dimensional laser extinction method was used to measure time-resolved soot concentrations and soot volume fractions; OH^* chemiluminescence (CL) imaging was used to measure the lift-off length and measure the distributions of the OH radicals qualitatively; soot luminosity images were used to identify the sooting area in the soot shadowgraph images. It was found that the equivalence ratio in the jet center at the lift-off length (ϕ_{CL}), which is influenced by the operating conditions, played a critical role in soot formation. Reductions in ϕ_{CL} thickened the OH zone in the upstream region of the jet, reducing the volume corresponding to the maximum soot volume fraction. The expansion of the OH zone also helped reduce the sooting zone's width. However, under high sooting conditions (e.g. ϕ_{CL}>3.5), the sooting zone width in the downstream jet was independent of ϕ_{CL}.

The third part of the thesis investigates combusting and non-combusting sprays formed from different blends of ethanol with diesel fuel. Using 0%-20% ethanol blended with diesel fuels, liquid/vapor phase spray images were captured, the ignition delay was measured, the lift-off length was measured, and natural soot luminosity images were captured. It was found that the differences in the fuels' composition did not significantly affect the liquid/vapor phase sprays. However, as the ethanol content of the fuel was increased from 0% to 20%, the lift-off length increased and the detectable soot luminescence decreased. This indicates that soot formation declines as the fuel's ethanol content increases.

Acknowledgement

I am grateful to many people who have directly and indirectly contributed to this work. First, I would like to thank my supervisors Mats Andersson and Sven Andersson. I am very grateful that I had a chance to work out a project together with them. Sven Andersson was my main supervisor during the first half of my study period, and I would like to thank him for giving me this opportunity to pursue my PhD studies. Mats Andersson was my main supervisor during the last half of my study period, and he was also a co-worker with me in the spray lab. I am deeply grateful to him for the time we spent together in the spray lab. Without him, the quality of the spray images in this thesis would have been far lower, and the optical set-ups would not have been created. I thank them both for their many helpful comments on my work, which greatly improved its quality. We had a fantastic time working together, for which I am very grateful.

Professor Ingemar Denbratt, the head of the combustion division, is acknowledged for taking me on as a student and giving me the opportunity to work in the division. I also thank the other senior researchers at the Combustion Division for constructive discussions and comments. In addition, I thank CERC and its parent companies for their financial support, which made my PhD studies possible. Members from 'Optical Methods for Spray and Combustion Diagnostics' reference group are also acknowledged for their comments on my work. In particular, I am grateful to Scania CV AB, who provided the fuel injection system and injectors used in my experiments. I also would like to thank my contact person at Scania CV AB, Kim Kylström, who helped to measure the nozzle geometries and assemble the nozzles.

Further thanks go to past and current colleagues in the lab, who helped me whenever I had difficulties preparing experiments: research engineers Patrik Wåhlin, Eugenio De Benito Sienes, Alf Magnusson, Anders Mattsson, Timothy Benham, and Jan Möller. I am also thankful for the electro-technical support of Robert and Lars Jernqvist, and for the administrative support I have received over the years from Elenor Norberg and Ulla Lindberg-Thieme.

Many thanks to the past and current PhD students at the division who helped me indirectly or directly. I will never forget the fun time we spent together during lunches, at fika, and after work. All of you have made my time in Sweden more cheerful.

Finally, I would like to express my gratitude to my parents and my sister's family, who have always been supportive. Last of all, I thank Sonam Ragbang for her love, for always supporting my work, and for being with me. I am also very grateful to have met her lovely family.

List of publications

Papers are appended in the thesis.

I. **Chengjun Du**, Sven Andersson, Mats Andersson, "The effect of cavitation on the estimation of fuel injection rates based on momentum flux measurements," *Submitted to the publication*, 2017.

II. **Chengjun Du**, Mats Andersson, Sven Andersson, "Effect of Nozzle Geometry on Diesel Spray Characteristics under Non-Evaporating and Evaporating Conditions," *ICLASS 2015, 13th Triennial International Conference on Liquid Atomization and Spray Systems*, Tainan, Taiwan, August 23-27, 2015.

III. **Chengjun Du**, Mats Andersson, Sven Andersson, "Effects of Nozzle Geometry on the Characteristics of an Evaporating Diesel Spray," *SAE Int. J. Fuels Lubr*. 9(3):493-513, 2016.

IV. **Chengjun Du**, Sven Andersson, Mats Andersson, "Time-Resolved Liquid and Vapor Phase Distribution Measurement in Diesel Sprays Using a Light Absorption Scattering Technique," *ILASS – Europe 2016, 27th Annual Conference on Liquid Atomization and Spray Systems*, Brighton, UK, September 4-7, 2016.

V. **Chengjun Du**, Sven Andersson, Mats Andersson, "Soot formation and oxidation in a turbulent diffusion diesel flame: the effect of injection pressure," *Submitted to the publication*, 2017.

VI. **Chengjun Du**, Sven Andersson, Mats Andersson, "Two-dimensional measurements of soot in a turbulent diffusion diesel flame: the effects of injection pressure, nozzle orifice diameter and gas density," *Submitted to the publication*, 2017.

VII. **Chengjun Du**, Mats Andersson, Sven Andersson, "The Influence of Ethanol Blending in Diesel fuel on the Spray and Spray Combustion Characteristics," *SAE Int. J. Fuels Lubr*. 7(3):823-832, 2014.

Other papers (not included in the thesis).

VIII. **Chengjun Du**, Mats Andersson, Sven Andersson, "Ignition Delay, Lift-off and Soot Luminescence in Diesel-Ethanol Spray Combustion," *Sustainable Automotive Technologies 2014*. Springer, Cham, 2015, p. 85-91.

IX. **Chengjun Du**, Mats Andersson, Sven Andersson, "An analysis of image evaluation procedures for measurements of diesel spray characteristics," *ILASS – Europe 2014, 26th Annual Conference on Liquid Atomization and Spray Systems*, Bremen, Germany, Sep 8-10, 2014.

Nomenclature

A	Cross-sectional area
A_{eff}	Cross-sectional area of flow
A_o	Area of the geometry orifice exit
α	Velocity or fuel volume fraction profile factor
β	Velocity or fuel volume fraction profile factor
c	Subscript denoting along the jet centerline
C_a	Area contraction coefficient
CN_s	Sou's cavitation number
D_o, d_o	Outlet diameter of orifice
D_{dif}	Thermal diffusivity
$E(m)$	Cross-sectional absorption function
f_v	Vapor volume fraction
θ	Spreading angle of spray
I	Transmitted light intensity
I_0	Incident light intensity
K	Dimensional extinction coefficient
K_a	Karlovitz flame stretch factor
K_e	Dimensionless extinction coefficient
l	Subscript denoting liquid phase fuel or droplets
L	Optical path length or liquid spray length
LOL	Lift-off length
$\dot{m}_f$	Fuel mass flow rate
$\dot{m}_a$	Gas or air mass flow rate
μ_l	Liquid kinematic viscosity
ξ	Non-dimensional radial coordinate
o	Subscript denoting at the nozzle orifice exit
P_a	Ambient pressure
P_{in}	Injection pressure
P_s	Partial pressure of the vapor fuel
P_v	Fuel vapor pressure
ρ_a	Ambient gas density
ρ_f	Fuel density
σ_s	Surface tension
σ	Standard deviation
R	Jet width
R_e	Reynolds number
Re_t	Local turbulent Reynolds number
S_L	Laminar flame velocity
S_t	Local turbulent premixed flame velocity
T	Temperature
T_a	Ambient temperature
T_f	Fuel temperature
T_s	Saturation temperature
u'	RMS of the axial velocity fluctuations

u_o	Velocity at the nozzle exit
u_l	Velocity of the liquid jet
We_g	Gas Weber number
We_l	Liquid Weber number
$\bar{X}_f$	Turbulent mean volume fraction
$\bar{\bar{X}}_f$	Cross-sectionally averaged fuel volume fraction
Z	Ohnesorge number
Z_{st}	Stoichiometric fuel fraction
ϕ	Equivalence ratio
ϕ_{CL}	Equivalence ratio in the jet center at the lift-off length

1-MN	1-methylnaphthalene
ASOI	After start of injection
CL	Chemiluminescence
DPF	Diesel particulate filter
EGR	Exhaust gas recirculation
HCCI	Homogeneous charge compression ignition
HCHO	Formaldehyde
HP/HT	High pressure / high temperature
KH	Kelvin–Helmholtz
LAS	Light absorption and scattering
LII	Laser-induced incandescence
LIS	Laser induced scattering
PAH	Polycyclic aromatic hydrocarbon
PLIF	Planar laser induced fluoresce
RMS	Root mean square of standard deviation from the mean value
R-T	Rayleigh–Taylor
UV	Ultraviolet

Contents

Chapter 1

Introduction

1.1 Climate change and the role of internal combustion engines

The environmental impact of global climate change is observable around the world; its direct effects include losses of sea ice and mountain snow, rising sea levels, and more intense heat waves. This climate change (i.e. global warming) is primarily due to human activity. Over the last century, the burning of fossil fuels has significantly increased the atmospheric concentration of greenhouse gases such as carbon dioxide (CO_2), methane (CH_4), and Nitrous Oxide (N_2O). The transportation sector is responsible for around 14% of global greenhouse gas emissions, and 95% of the world's transportation energy comes from petroleum-based fuels – primarily gasoline and diesel [1]. In the European Union (EU), more than two thirds of transport-related greenhouse gas emissions originate from road transport [2]. Therefore, reducing transport-related greenhouse gas emissions must be a central objective of any effective effort to control climate change.

Transport is important for daily life in modern societies. The internal combustion (IC) engine was the main source of power for transportation over the last century, and will probably remain so for the foreseeable future [3]: while the contributions of non-fossil-fueled alternatives such as electric motors and hydrogen-powered engines are rapidly increasing, they remain negligible compared to that of IC engines powered by conventional liquid fuels. Reducing greenhouse gas emissions will therefore require a deeper understanding of physical combustion processes in IC engines.

The studies presented in this thesis all relate to conventional compression ignition (diesel) engines. Diesel engines dominate the commercial road transport and marine sectors, and are more efficient than spark ignition (SI) engines. However, they suffer from high engine-out emissions of particulate matter (PM) and NO_x (nitrogen oxides). Soot particles formed during combustion are the primary sources of particulate matter, while NO_x is generated from the reaction of oxygen with nitrogen at high temperatures and pressures. Both soot particles and NO_x can cause significant public health problems because they increase the risk of respiratory conditions and exacerbate lung conditions, among other things. In addition, NO_x contributes to fine particle formation. Regulations concerning emissions of particulates and NO_x are therefore becoming more stringent all over the world, necessitating the use of increasingly complex engine after-treatment control systems. While such systems can significantly reduce engine-out emissions, it is also vital to minimize the formation of these emissions using in-cylinder strategies to reduce the after-treatment burden. Therefore, this thesis focuses on improving the understanding of fuel-air mixing and spray combustion process under diesel engine-like conditions.

1.2 Motivation

In conventional diesel engines, the quality of fuel-air mixing profoundly affects the combustion process, which in turn affects fuel efficiency and engine-out emissions. Figure 1.1 depicts the fuel-air mixing process and the subsequent formation of a reacting spray (combustion) during the main injection event. During this period, gas in the combustion chamber reaches high pressures and temperatures, and the

oxygen concentration (ζ_{O_2}) may be reduced by introducing exhaust gas recirculation (EGR) to reduce NO_x emissions.

Broadly speaking, spray formation involves the following steps: pressurized liquid fuel flows through a micro nozzle orifice with a high injection velocity; the injected liquid fuel is atomized into fine liquid drops, forming a kind of cone-structure spray with a solid angle; and finally, the liquid droplets rapidly vaporize because of thermodynamic heat transfer between surrounding gases and liquid droplets. This occurs because of HP/HT gas entrainment driven by momentum exchange between the liquid spray and the surrounding gases; near the liquid spray tip region, the lifted diffusion flame stabilizes and extends to the tip of spray head. In the meantime, chemical reactions within the spray release thermal energy, allowing the engine to perform mechanical work. When the ambient temperature and the fuel concentration are high enough, soot particles form and are emitted as exhaust emissions if they are not sufficiently oxidized. NO may also form where the local temperature of the reacting spray is high.

To minimize emissions while maintaining or improving fuel efficiency, it is necessary to have a short liquid jet breakup length, rapid fuel vaporization (i.e. a high mixing rate) and a low combustion temperature. The evolution of non-reacting and reacting sprays is highly sensitive to operating parameters such as the injection pressure (which determines the fuel injection rate and spray velocity), nozzle geometry, gas conditions, cylinder gas motion (e.g. swirl), and fuel properties. However, the effects of operating parameters on fundamental spray processes are not fully understood. Detailed information on the temporal and spatial characteristics of spray processes under realistic engine-like conditions is needed to predict spray formation and to develop engine systems that can control it effectively to reduce engine-out emissions. The internal flow inside the nozzle orifice is depicted in Figure 1.1. Cavitation is known to play an important role in primary jet break-up and subsequent processes, but its effects are poorly understood, partly because the transient flow inside the nozzle is highly turbulent and the flow outside the nozzle orifice is optically dense. The effects of nozzle geometry, gas conditions and fuel injection conditions on the diesel sprays have been investigated extensively using in-situ optical methods. However, there is little information on the two-dimensional structure of diesel sprays under practically relevant conditions. Therefore, the work presented in this thesis used various two-dimensional optical methods to study spray formation and combustion under various conditions in an optically accessible continuous-flow type HP / HT chamber.

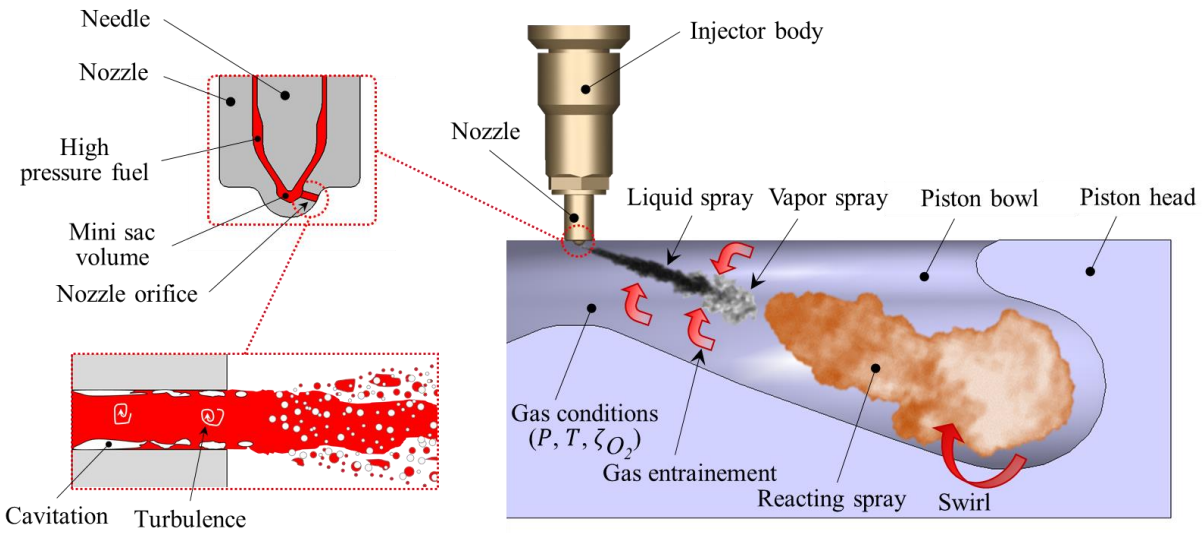

Figure 1.1. The evolution of fuel-air mixing in diesel engines and internal flow inside the nozzle orifice.

1.3 Research questions

Sections 2.1 and 2.2 introduced the causes of cavitation and reviewed previous studies on this phenomenon and its effects in diesel engines. This introduction was provided to help the reader understand the effects of cavitation on liquid jet break-up and to complement the original research presented in this thesis by providing insight into aspects of this phenomenon not covered in the appended papers. As shown by most of the experimental examples discussed in Sections 2.1 and 2.2, the effect of cavitation on the internal flow and near the nozzle exit can be studied by direct observation of internal or near-nozzle flows. One of studies included in this thesis investigated the effect of cavitation on internal flows indirectly. As shown in Figure 2.4, the cavitation films adhere to the wall of the nozzle orifice, giving rise to a non-uninform velocity distribution just downstream of the cavitation films. This could reduce the accuracy of injection rate estimates based on momentum flux measurements. Two different methods for measuring fuel injection rates based on momentum flux measurements have been reported. The first does not account for the occurrence of cavitation in the nozzle orifice, and has been used by several research groups; the second accounts for cavitation bubbles or foaming in the nozzle orifice by reducing the effective orifice area. To date, these approaches have not been compared using reference experimental data for cavitating and non-cavitating nozzles. Therefore, one of the research questions of this thesis was:

(1) How does the nozzle geometry-induced cavitation influence the evaluation of fuel injection rate based on momentum flux measurements?

To answer this question, experiments were performed with two nozzles, one having a cylindrical orifice with a strong tendency to induce cavitation and another having a convergent orifice that tends to suppress cavitation. In addition, near-field microscopic images were captured to investigate the effect of cavitation on the liquid jet at the nozzle exit. This work is presented in Appended Paper I.

Another focus of the thesis is the effect of geometry-induced cavitation on the far downstream regions of liquid and vapor phase diesel sprays. As reviewed in Section 2.2, cavitation in the internal flow enhances primary break-up. Moreover, CFD studies reported by Som et al. [4] suggested that the nozzles with cavitation-inducing geometries (i.e. sharp inlet and cylindrical holes) enhanced primary break-up and reduced liquid spray penetration under evaporating conditions compared to conical nozzles (which produce much less or no cavitation). However, this contradicts the experimental finding of Payri et al. [5], who found that a cavitating cylindrical nozzle exhibited longer liquid spray penetration under evaporating conditions than a conical non-cavitating one. They also concluded that fuel vaporization is controlled by fuel/air mixing. There is no consensus concerning the effect of geometry-induced cavitation on the vaporization of the liquid phase spray. Therefore, another research question of this thesis was:

(2) Do cavitating nozzles enhance primary break-up and thereby accelerate vaporization (resulting in shorter liquid penetration) compared to non-cavitating nozzles?

To answer this question, experiments were performed with three different nozzle geometries. A difference between these experiments and previous works is that two of the tested nozzles (one cylindrical and one conical) had similar mass flow rates. These studies are presented in Appended Paper II, which focuses exclusively on liquid phase spray data acquired under evaporating and non-evaporating conditions.

Previous studies on the effect of geometry-induced cavitation on spray properties were mostly based on measurements of the liquid/vapor length and the spray's spreading angle. To better understand the effect of geometry-induced cavitation on the properties of vapor sprays, qualitative measurements of the vapor volume fraction were performed using a light absorption and scattering approach. The research question addressed in this work was:

(3) How does geometry-induced cavitation influence the distribution of vapor phase sprays?

To qualitatively compare the vapor volume fractions formed with different nozzles, Musculus and Kattke's variable mixture model [6] was used to explain the experimental results. This part of the work is presented in Appended Paper III, and is a continuation of the work presented in Appended Paper II.

Various methods for performing vapor spray measurements have been developed, each of which has its advantages and disadvantages. The light absorption and scattering (LAS) technique developed by Suzuki et al. [7] has a high signal-to-noise ratio, low ambient temperature dependence, and no fluorescence quenching. However, it can only be used to perform single-shot measurements, i.e. only one spray image is captured in each injection event. To capture the complete development of the liquid and vapor phases, a time-resolved LAS method was developed. In addition, two different percentages of the tracer fuel (1-methylnaphthalene) blended with n-dodecane fuel were investigated at various ambient conditions. The research question addressed in this part of the work was:

(4) How does varying the concentration of the tracer compound affect the vapor phase concentration under various operating conditions using the LAS technique?

It was demonstrated that the modified LAS method can provide useful time-resolved vapor phase concentration measurements, as described in Appended Paper IV. In fact, the LAS technique was even successfully applied to a commercial diesel fuel, as discussed in Appended Paper III.

The spray experiments discussed above were performed under non-combusting conditions. Additional studies on spray characteristics were performed under combustion conditions. Conventional diesel spray combustion involves typical lifted turbulent diffusion flames, which produce soot particles. Various methods for reducing soot formation during diesel spray combustion have been proposed, one of which is to increase the injection pressure. The focus of this study is on the relationship between the injection pressure and soot formation and oxidation. It is well known that the cross-sectionally averaged equivalence ratio at the lift-off length declines as the injection pressure increases, which reduces soot formation. In addition, the soot volume fraction has only been measured along the spray axis using a point laser extinction method [8]; there is a lack of studies on the relationship between the injection pressure and the soot volume fraction using two-dimensional measurement techniques. To fill this gap, two additional research questions were investigated:

(5) How does the injection pressure influence the soot volume fraction when measured using two-dimensional methods?
(6) How does the injection pressure influence the local equivalence ratio at the lift-off length and OH radical distribution? Moreover, what is the relationship between these two factors and soot formation and oxidation?

To answer these questions, time-resolved two-dimensional soot shadowgraph, nature flame (soot) luminosity and OH^* chemiluminescence images were captured simultaneously. Soot volume fraction and OH radical distribution images were obtained using a tomographic inversion algorithm, and the local equivalence ratio in the lift-off length region was predicted using the variable mixture profile model. These studies are presented in Appended Paper V. One finding of this study was that the sooting zone width decreased as the injection pressure increased. This contradicts a previous report [7] that the sooting zone width was independent of the injection pressure. However, the experiments presented in Paper V used only a single nozzle orifice diameter and were conducted under fixed ambient conditions. Therefore, to better understand the studied processes, a new research question was posed:

(7) How do the nozzle orifice diameter, injection pressure, and ambient gas density influence soot formation and oxidation when measured using two-dimensional methods?

This part of study is presented in Appended Paper VI. In addition to the studies described above using the diesel fuels, a new investigation was conducted to investigate how the use of ethanol-diesel blends affected the characteristics of combusting and non-combusting sprays. There are several reports on engine experiments with diesel-ethanol blends fuels and spray studies using diesel-ethanol blends under non-combusting conditions. However, there is a lack of spray studies on such blends under combusting conditions even though such investigations could provide important data on the effects of ethanol on soot formation during diesel combustion. Therefore, the penultimate research question was:

(8) How do ethanol-diesel blends influence combusting and non-combusting spray behavior, and particularly soot formation in combusting sprays?

To this end, liquid/vapor spray penetration, liquid spray cone angles, ignition delay, OH^* chemiluminescence, lift-off lengths, and soot luminescence were measured. This study is presented in Appended Paper VII.

Line-of-sight OH^* chemiluminescence imaging has been widely used in diesel spray studies. OH^* chemiluminescence images can be used to measure lift-off lengths or to determine the ignition delay and delineate the high temperature reaction zone. Additionally, the intensities of OH^* chemiluminescence images have been used to analyze reaction rates [9]. However, soot incandescence and CO_2^* chemiluminescence may contribute to the observed light emissions in the OH^* chemiluminescence wavelength range, and soot particles can absorb light emissions in this wavelength range as well. To better understand the behavior of OH^* chemiluminescence in sooting diesel flames, OH^* chemiluminescence images were recorded from two orthogonal directions simultaneously, together with spectral data. The research question addressed in this study was:

(9) To what extent is the OH^* chemiluminescence absorbed by the soot particles, and does soot incandescence contribute to the light emissions in the OH^* chemiluminescence wavelength range?

The results of this study are presented in Chapter 5 of this thesis ("Unpublished findings – OH^* chemiluminescence investigation").

1.4 Structure of the thesis

Most of the studies conducted during my work on this thesis are presented in detail in the appended papers. Each paper includes detailed background information and the motivation for the presented study in its 'Introduction' section. The chapters of this thesis are intended to complement the appended papers by providing additional background information and more extensive discussions of certain aspects that could not be covered in the published papers for the sake of brevity. A conscious effort was made to avoid repeating the contents of the appended papers in the thesis chapters.

Chapter 1 introduces the role of internal combustion engines in modern societies and its effects on the global climate, and presents the motivation for the thesis work and the research questions addressed by the studies. Chapter 2 reviews the fundamental physics governing pressurized liquid fuel flowing through a nozzle orifice, spray formation, and the final turbulent diffusion combustion processes. Section 2.1 reviews previous studies on cavitating internal flows and introduces the causes of cavitation and its effects on the internal flow. Section 2.2 uses regime maps for liquid jet primary break-up and the secondary break-up of liquid sprays to introduce the basic mechanisms of jet break-up. In addition, the effect of cavitation on primary break-up is reviewed. Together, these two sections help the reader understand what cavitation is and why it is important to understand its effects on injection rate measurements and the

behavior of liquid/vapor phase sprays. The experimental results presented in Appended Paper III are explained using the variable mixture profile, which was also used to predict local equivalence ratios in the studies presented in Appended Papers V and VI. Therefore, Musculus and Kattke's variable mixture profile is briefly reviewed in Section 2.3, together with the equations used to predict local equivalence ratios in Papers V and VI. In Papers V and VI, the reduced air entrainment caused by reaction was taken into account when predicting local equivalence ratios for reacting jets. Therefore, Section 2.3 reviews the differences between reacting and non-reacting jets in terms of penetration and air entrainment. During the diffusion combustion phase, a reacting diesel spray becomes a typical lifted turbulent flame. This strongly influences diesel spray combustion. Section 2.4 therefore reviews the properties of lifted flames in diesel sprays. This will help readers to understand the dominant factors governing lifted flame behavior and why the partially premixed combustion concept should be considered when analyzing lifted combustion flames. The effects of operating conditions on soot formation in reacting diesel sprays are discussed extensively in Papers V-VII. To complement these discussions, Section 2.5 reviews the fundamental mechanisms of soot formation and oxidation, and some strategies for reducing soot formation in diesel sprays. Section 2.6 reviews several conceptual models for the diffusion combustion phase. This will help readers to interpret the two-dimensional reacting diesel spray structures presented in Appended Papers V and VI. Finally, Section 2.7 reviews various combustion modes for diesel engines based on the '$\phi - T$ coordinate map'. This provides guidelines for achieving diesel combustion that simultaneously produces low emissions of soot and NO_x. In addition, a combustion mode similar to that studied in the experiments is discussed, using an injector with a small orifice diameter, high injection pressures, and low ambient temperatures.

The focus of this work is mainly on improving the understanding of the effects of operating conditions on diesel spray characteristics. The development of optical diagnostic methods is not a major focus, so the theoretical principles of optics are not discussed in Chapter 3. The main equipment used in this work, the high pressure / high temperature chamber, is described extensively in Appended Papers V and VII. In addition, Section 3.1 briefly introduces the HP/HT spray chamber. Section 3.2 provides a mathematical description of the theory of Abel inversion for line-of-sight images, which is not covered in Papers V and VI. Section 3.4 focuses on the choice of laser wavelength in the experiments and the beam steering effects on soot measurements using two-dimensional laser extinction. This is also not covered in Papers V and VI, and it will help the reader understand the limitations of the new soot measurement technique described in those papers. Chapter 4 summarizes the appended papers, and Chapter 5 presents unpublished findings from studies on line-of-sight OH^* chemiluminescence images. Finally, Chapter 6 presents the outlook for future work in this field.

References

[1] Global Greenhouse Gas Emissions Data, https://www.epa.gov/ghgemissions/global-greenhouse-gas-emissions-data

[2] European Commission, "Reducing emissions from transport," http://ec.europa.eu/clima/policies/transport/index_en.htm.

[3] Kalghatgi GT. "Fuel/engine interactions," *Warrendale, PA: SAE International*, 2013.

[4] Som, S., Ramirez, A. I., Longman, D. E., & Aggarwal, S. K. (2011). Effect of nozzle orifice geometry on spray, combustion, and emission characteristics under diesel engine conditions. *Fuel*, *90*(3), 1267-1276.

[5] Payri, R., Salvador, F. J., Gimeno, J., & Zapata, L. D. (2008). Diesel nozzle geometry influence on spray liquid-phase fuel penetration in evaporative conditions. *Fuel*, *87*(7), 1165-1176.

[6] Musculus, M. P., & Kattke, K. (2009). Entrainment waves in diesel jets. *SAE International Journal of Engines*, *2*(2009-01-1355), 1170-1193.

[7] Suzuki, M., Nishida, K., & Hiroyasu, H. (1993). Simultaneous concentration measurement of vapor and liquid in an evaporating diesel spray (No. 930863). *SAE Technical Paper*.

[8] Pickett, L. M., & Siebers, D. L. (2004). Soot in diesel fuel jets: effects of ambient temperature, ambient density, and injection pressure. *Combustion and Flame*, *138*(1), 114-135.

[9] Zhang, J., Jing, W., & Fang, T. (2012). High speed imaging of OH^* chemiluminescence and natural luminosity of low temperature diesel spray combustion. *Fuel*, *99*, 226-234.

Chapter 2

Theoretical background

This chapter introduces some fundamental physical processes involved in the combustion of fuel sprays and describes the events that occur during a combustion cycle, starting with the flow of pressurized liquid fuel through the internal nozzle orifice and concluding with the subsequent turbulent diffusion combustion process. Because this thesis includes studies on the effect of geometry-induced cavitation on non-reacting jets and the estimation of injection rates, this chapter also presents general background information on cavitating flows through nozzle orifices. In addition, the basic mechanisms governing the primary break-up of liquid jets are introduced, followed by those governing secondary break-up of the liquid spray. These discussions emphasize the variable mixture profile model and the difference in air entrainment between reacting and non-reacting jets. Finally, some properties of lifted turbulent diffusion flames, the mechanisms of soot formation and degradation, and conceptual models developed by different authors are presented.

2.1 Cavitation in the nozzle orifice

Cavitation is a process of nucleation in a liquid flow. In terms of basic physics, nucleation is a phase change from the liquid phase to the gas phase. There are two kinds of nucleation processes: cavitation processes and superheat processes. If a liquid at constant temperature is subjected to a pressure below its saturated vapor pressure, P_v, its surface will rupture; this process is called cavitation. Likewise, if a liquid at constant pressure is heated above its saturation temperature, T_s, its surface will also rupture; this process is called boiling [1]. In real diesel engines, the injector nozzle is cooled by the coolant, whose temperature is around 353 K, which is lower than the distillation range of diesel fuel [2]. Therefore, boiling-type nucleation processes are not considered in this work.

In modern light- or heavy-duty diesel engines, the liquid fuel may be pressurized to over 2000 bar. The pressurized fuel is then delivered to a solenoid or piezo-activated injector. High pressure fuel flows through the nozzle orifice into a region of ambient pressure, which is substantially lower than the pressure of the fuel. The diameter of the nozzle orifice is normally around 0.15-0.20 mm. The flow velocity during an injection event is on the order of several hundred meters per second, and the flow is transient, with an injection duration of a few milliseconds. In addition, the flow inside the nozzle is highly turbulent and exhibits transient two-phase behavior. This makes direct observation of the internal flow difficult, and the physics of the internal flow are not fully understood. However, it is well established that nozzle geometry strongly affects the occurrence of cavitation, and particularly that cavitation is strongly favored by nozzles whose orifice inlets have sharp corners (e.g. nozzles without hydro-grinding) or cylindrical nozzles [3, 4]. This type of cavitation occurs when the pressure of the liquid at the entrance of the holes falls below its vapor pressure, leading to the initiation of cavitation at the point where the liquid must turn sharply into the nozzle entrance and accelerate. Figure 2.1 depicts this cavitation mechanism.

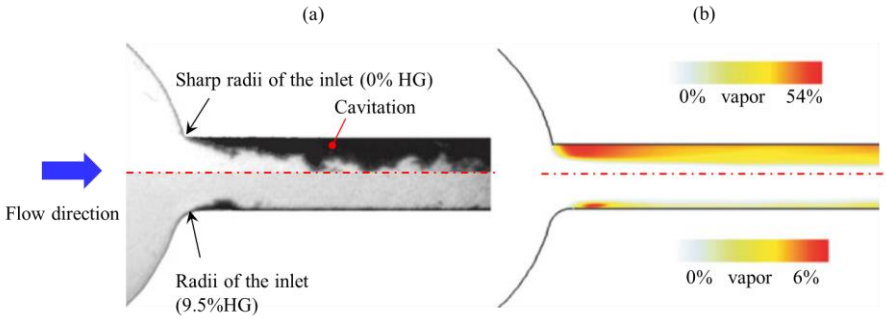

Figure 2.1. Geometry induced cavitation. (a) Shadowgraph image of flows through single-hole sac-type axisymmetric nozzles with 0% (top) and 9.5% (bottom) hydro-grinding, respectively (taken from the work of König and Blessing [5]). (b) Simulated temporal mean cavitation volume percentage distributions (from the work of Giannadakis et al. [4]). Conditions: $P_{in} = 500\ bar, P_a = 1\ bar$, orifice exit diameter ≈0.2 mm.

Another type of cavitation is 'string' or 'vortex' cavitation [6, 7], which is depicted in Figure 2.2. Andriotis et al. [6] described this type of cavitation in a transparent real-sized nozzle for low-speed two-stroke diesel engines. Later, Gavaises et al. [7] reported string cavitation in an enlarged transparent nozzle with convergent orifices for a VCO-type diesel injector. Both studies concluded that the string cavitation originated either from pre-existing geometry-induced cavitation sites or from trapped air at a point downstream of the orifice exit. String cavitation occurs inside vortex structures because of the non-uniform flow distribution upstream of the nozzle orifices [7]. Recently, Mitroglou el al. [8] observed string-type cavitation in a transparent mini-sac type diesel injector nozzle. They concluded that this string cavitation was due to the trapping of pre-existing bubbles, which altered the flow of the subsequent injection. It is well-established that nozzles with hydro-ground inlets and convergent orifices suppress geometry-induced cavitation, and free cavitation has been observed inside such nozzles [3, 9]. However, both Andriotis et al. and Gavaises et al. [6, 7] observed string cavitation in nozzles of this kind. These findings indicate a need for a better understanding of cavitation mechanisms and their effect on the subsequent primary jet break-up.

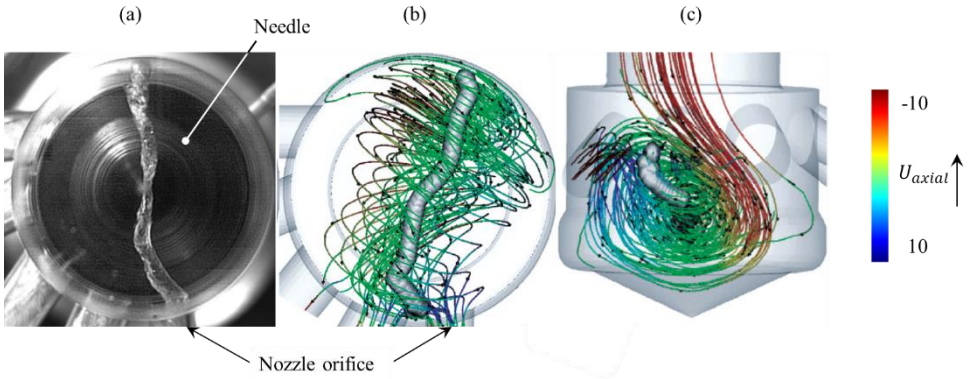

Figure 2.2. Demonstration of string cavitation as reported by Andriotis et al [6]. (a) experimental image of string cavitation formed inside the nozzle volume (bottom view), (b) and (c) three-dimensional reconstruction of the visualized string cavitation superimposed on the calculated flow field, (b) seen from below, (c) seen from side. Conditions: adequate needle lift, R_e =68,000, orifice exit diameter = 1.5 mm.

Many images of cavitation in transparent diesel injector nozzles have been captured using line-of-sight techniques such as shadowgraph imaging or X-ray imaging. Badock et al. [10] observed the detailed structure of cavitation films in a transparent cylindrical orifice using thin laser sheet measurements. The shadowgraph image presented in Figure 2.3 (a) suggests that the entire orifice is filled with bubbles

because of cavitation. However, the corresponding laser sheet image (Figure 2.3 (b)) clearly shows that the intact liquid core is surrounded by cavitation films or bubbles near the orifice wall, which is completely different to the conclusion suggested by the shadowgraph image.

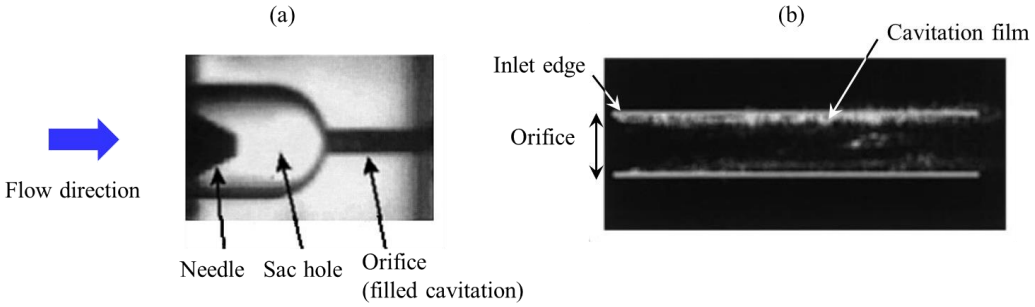

Figure 2.3. Shadowgraph (a) and laser sheet images (b) of cavitation in a diesel injector acquired by Badock et al. [9]. Conditions: P_{in} = 250 bar, P_a = 15 bar, diameter of orifice 0.2 mm, orifice length 1.0 mm, needle lifted sufficiently.

Cavitation in the orifice also influences the velocity profile in the orifice exit. In an early study, Chaves et al. [11, 12] measured the velocity of the internal flow in a transparent nozzle with an orifice exit diameter of 0.2 mm by tracking the cavitation bubbles. They showed that the velocity at the orifice exit near to the orifice wall was close to the geometric mean velocity, and the velocity in the center of the nozzle was much higher than the geometric mean velocity. The geometric mean velocity was defined as the theoretical maximum velocity divided by the discharge coefficient. Sou et al. [13] measured the velocity distribution in a cavitating enlarged transparent rectangle-hole nozzle using a laser Doppler velocimetry technique. Figure 2.4 shows the distribution of the mean liquid velocity for different cavitating film lengths. The velocity distribution is non-uniform downstream of the cavitation film; this is consistent with the velocity measurements of Chaves et al. [11]. This non-uniform distribution of liquid at the orifice exit will affect jet atomization and break-up, which is discussed in the next section. It should be noted that Sou et al. [13] used an enlarged nozzle, and enlarged nozzles exhibit different cavitation behavior to real-size transparent nozzles [14, 15]. However, Arcoumanis et al. [14] have shown that the cavitation structures formed in enlarged nozzles are reasonably similar to those in real-sized nozzles. Therefore, results obtained with enlarged transparent nozzles can be useful for understanding cavitation phenomena in a real-size nozzle.

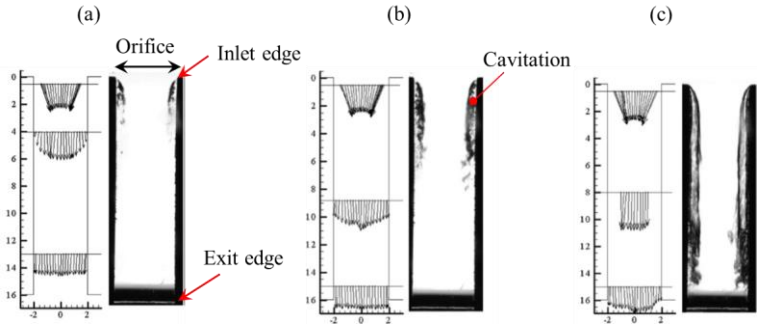

Figure 2.4. Distributions of the mean liquid velocity in a cavitating nozzle as reported Sou et al. [13]. Experimental conditions: (a) R_e =58,000, (b), R_e =64,000, (c), R_e =70,000. Nozzle width = 4 mm, nozzle length = 16 mm, liquid was water.

2.2. Primary and secondary break-up processes

Break-up is the process whereby the liquid jet created during the injection event is fragmented into smaller jets known as ligaments or isolated droplets. The initial break-up of the jet is termed primary break-up, and the further fragmentation of the droplets and ligaments formed by primary break-up is known as secondary break-up. Upon injection, the liquid fuel interacts with the gas phase. The behavior of the liquid-gas interface is highly sensitive to two key boundary conditions: the stress balance and the kinematic conditions. These conditions depend on the relative velocity and properties of the liquid and surrounding gases. The break-up mechanism for a given jet can be classified on the basis of non-dimensional numbers describing its properties, such as the liquid Reynolds number R_e, liquid Weber number We_l, and Ohnesorge number Z. The Reynolds number and liquid Weber number represent the ratio of the inertia to the viscous forces of the liquid and the ratio of the inertia to surface tension forces at the liquid/gas interface, respectively. The Ohnesorge number is the ratio of the Reynolds number and Weber number, and represents the ratio of the viscous force to the surface tension. More precisely, these non-dimensional numbers are defined as follows:

$$R_e = \frac{\rho_l u_l D_o}{\mu_l} \tag{2-1}$$

$$We_l = \frac{\rho_l u_l^2 D_o}{\sigma} \tag{2-2}$$

$$Z = \frac{\sqrt{We_l}}{R_e} = \frac{\mu_l}{\sqrt{\sigma_s \rho_l D_o}} \tag{2-3}$$

where ρ_l is the density of the liquid, u_l is the mean velocity of the liquid jet, μ_l is the liquid kinematic viscosity, σ_s is the surface tension, and D_o is the nozzle's orifice exit diameter. Reitz [16] suggested that the ambient gas density should also be accounted for when analyzing jet break-up regimes, yielding the qualitative description shown in Figure 2.5 (a). The diesel jet's break-up behavior is within the atomization regime, which is depicted in Figure 2.5 (b).

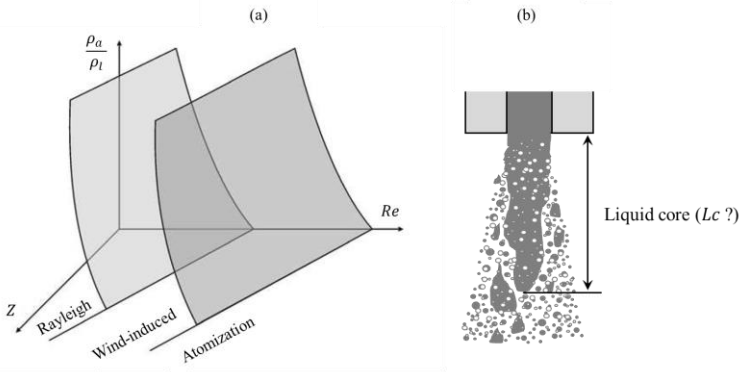

Figure 2.5. The regime of jet primary break-up regime (a) presented by Reitz [16], and a description of jet break-up in the atomization regime (b).

Under conventional diesel-engine like conditions, the liquid fuel is injected into a relatively high gas density, and the gas density strongly influences the jet atomization. Early studies by Reitz et al. [17] and Hiroyasu et al. [18] indicated that the jet's dispersion was proportional to the ratio of the gas and liquid densities. Hiroyasu et al. also found that the Sauter mean diameter decreased as the ambient gas density increased. X-ray measurements conducted by Leick et al. [19] indicated that (at the studied gas density) the liquid mixed rapidly with the surrounding gas near the nozzle exit, and suggested that the liquid core

length must be less than 2 mm. This stands in contrast to the findings of Paciaroni et al. [20], who observed a dense core near the nozzle exit with no evidence of break-up in a water jet using the ballistic imaging technique.

The break-up regime depicted in Figure 2.5 does not account for the effect of nozzle geometry on the break-up process. Two separate groups [17, 18] have shown that the jet break-up process is affected by the nozzle geometry, i.e. the effect of cavitation on the primary break-up. Hiroyasu et al. [18] derived an empirical equation for the break-up length, Lc. However, there have been no exact determinations of the liquid core length of dense diesel jets and their primary break-up mechanism remains poorly understood [21].

The key mechanisms of primary break-up processes for jets formed by high pressure diesel injection are the aerodynamic-induced, turbulence-induced and cavitation-induced mechanisms, which are depicted in Figure 2.6. The injected liquid jet with a high injection velocity induces aerodynamic shear forces at the liquid/gas interfaces, creating unstable waves that grow at the liquid surfaces. Droplets are sheared off from the liquid surfaces because of the unstable growth of these waves. This break-up mechanism is known as the aerodynamic-induced mechanism and can be simulated using the well-known Kelvin–Helmholtz (KH) instability model. The highly turbulent liquid flow inside the orifice generates a radial velocity at the jet's surface, and the highly turbulent eddies can overcome the liquid's surface tension, leading to the turbulence-induced separation of droplets from the jet. As discussed in Section 2.1, cavitation films or bubbles may form inside the orifice. These structures collapse near the jet exit, causing droplets to separate from the jet; this process is known as the cavitation-induced primary break-up mechanism and is described in more detail elsewhere [22, 23]. Som and Aggarwal [24] reported that the inclusion of cavitation in their KH-ACT model yielded better agreement with experimentally observed liquid and vapor lengths than was achieved using a model that disregards cavitation.

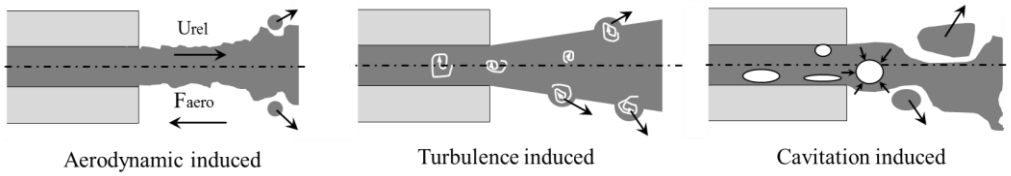

Figure 2.6. Schematic of the primary break-up mechanism.

It should be noted that the collapse of bubbles near the orifice exit could also induce the turbulence in the jet. Sou et al. [13] found that the turbulence induced by bubble collapse contributed to the formation of ligaments near the nozzle exit, as depicted in Figure 2.7. In this figure, CN_s is the cavitation number defined by Sou et al. as

$$CN_s = \frac{P_a - P_v}{0.5\rho_l {u_o}^2} \tag{2-4}$$

Several cavitation numbers have been defined by different authors. Sou et al. reported that the cavitation number CN_s defined by them strongly affected the cavitation and the liquid jet near the nozzle exit. In Figure 2.7 (a), the CN_s=0.65 and CN_s=0.78 cases correspond to the 'super cavitation' and 'developing cavitation' regimes defined by Sou et al. Under the 'super cavitation' regime, the cavitation film extends almost to the orifice exit, whereas under the 'developing cavitation' regime, it does not. As shown in Figure 2.7 (a), there are more ligaments formed at the jet periphery in the 'super cavitation' case than in the 'developing cavitation' one. This is due to the greater radial velocity and turbulence intensity in the radial direction near the orifice exit for the 'super cavitation' case, as shown in Figure 2.7 (b) and (c).

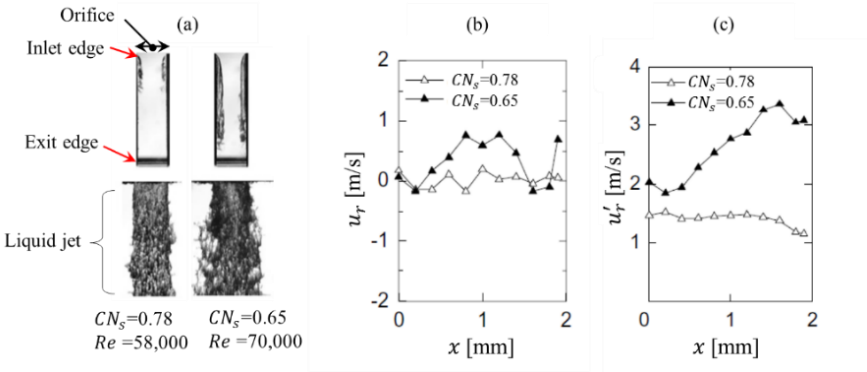

Figure 2.7. The effect of cavitation on the liquid jet near the orifice exit as reported by Sou et al. [13]. (a): cavitation inside the orifice and liquid jet near the orifice exit, (b): the mean radial velocity, and (c): turbulence intensity in the radial direction. The x-axis 'x' in (b) and (c) is above the orifice exit. Experimental conditions: width of nozzle = 4 mm, length of nozzle = 16 mm, liquid was water.

Similar findings were recently reported by Moon et al. [25], who captured liquid jet images near the orifice exit using the X-ray measurement technique with an axial single-hole nozzle as well as 3-hole and 6-hole nozzles. As shown in Figure 2.8, the multi-hole nozzles produced more droplets and ligament break-up than the single-hole nozzle. The authors concluded that this enhancement of primary break-up was due to a higher radial velocity and turbulent structure in the liquid jet, which originated from the instability of the internal liquid flow rather than being induced by aerodynamic factors.

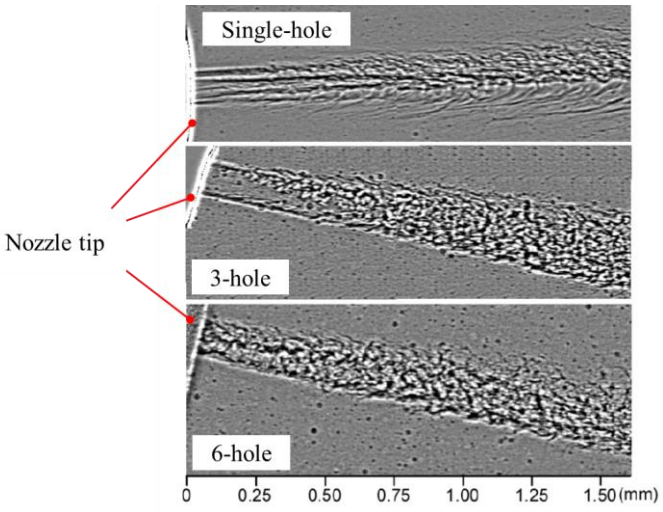

Figure 2.8. Liquid jet images near the orifice exit for the single-hole, 3-hole and 6-hole nozzles from the work of Moon et al. [25]. Experimental conditions: P_{in} = 1500 bar, P_a = 1 bar, diameter of orifice exit 0.12 mm, needle lifted sufficiently.

As summarized above, the understanding of primary break-up processes has been deepened by advances in measurement techniques and modeling methods. However, quantitative measurements of liquid diesel jets near the orifice exit are challenging to acquire because of their high turbulence and optical density [26]. Further work is therefore needed to properly understand the mechanisms of primary break-up.

The above discussion briefly introduced the known primary break-up mechanisms. Secondary break-up is the process by which the droplets or ligaments that separate from the jet during primary break-up are themselves broken up. A regime map of droplet break-up mechanisms created by Faeth et al. [27] is

shown in Figure 2.9 (a). These workers showed that the liquid/gas density ratio (for values > 8) and Reynolds number (for values >50) had relatively minor effects on droplet secondary break-up. Therefore, the secondary break-up regime is determined primarily by the gas Weber (We_g) number. This implies that under diesel-like conditions (high ambient temperature and thus low droplet viscosity, Z<0.1), droplet breakup and deformation are highly sensitive to aerodynamic forces. Chryssakis and Assanis [30] showed that for injection pressures of 400-1500 bar, the shear and catastrophic droplet break-up mechanisms were dominant at an ambient temperature and pressure of 400 K and 30 bar. These two mechanisms are depicted in Figure 2.9 (b). Chryssakis and Assanis [30] also showed that the number of droplets undergoing break-up via the catastrophic mechanism increased with the injection pressure. This implies that aerodynamic forces have significant effects on droplet break-up in jet formed by high pressure diesel injectors. Further details of these studies can be found in Refs. [27-30].

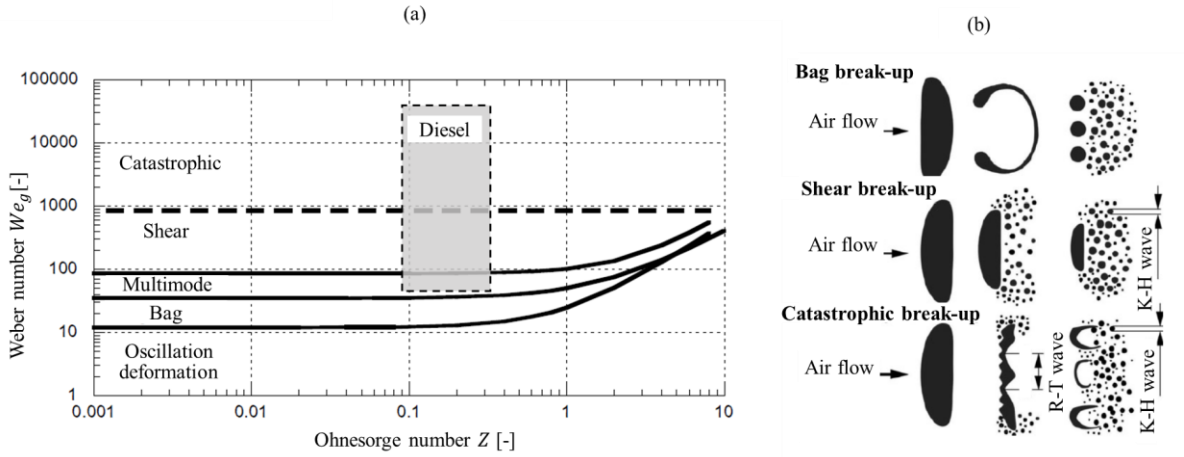

Figure 2.9. The droplet break-up regime map (a) presented Faeth et al. [27], and depictions of droplet break-up mechanisms from the work of Chryssakis et al. [28] (b). The shaded gray box in Figure (a) highlights the break-up conditions encountered in a typical diesel engine, based on the work of Chryssakis et al. [28]. The R-T wave shown in (b) corresponds to droplet break up caused by Rayleigh–Taylor instability.

2.3 Variable mixture profile model and air entrainment

The previous section introduced some of the basic physical processes governing mixture formation. The equations describing these processes are complemented by empirical equations that have emerged from experimental studies on diesel sprays. Empirical equations can be used to predict the liquid/vapor spray penetration, spray cone angle, and average/local cross-sectional equivalence ratio, making it possible to model some of the unknown or poorly understood processes affecting diesel spray behavior. An early study by Wakuri et al. [31] introduced an empirical equation for the spray penetration based on the conservation of the momentum. Using a similar approach, Naber and Siebers [33] derived an empirical spray penetration equation that is applicable to non-vaporizing sprays across a wide range of experimental conditions. This equation makes two severe assumptions: that the velocity profile is uniform across all axial locations, and that there is a quasi-steady flow with a uniform growth rate. While these assumptions are not consistent with a real jet's transient mixture profile, the predicted penetrations agree well with experimental results. Siebers [34] later used this uniform mixture profile model to develop a scaling law that successfully predicted the liquid penetration of a vaporizing spray based on the mixing-limited assumption.

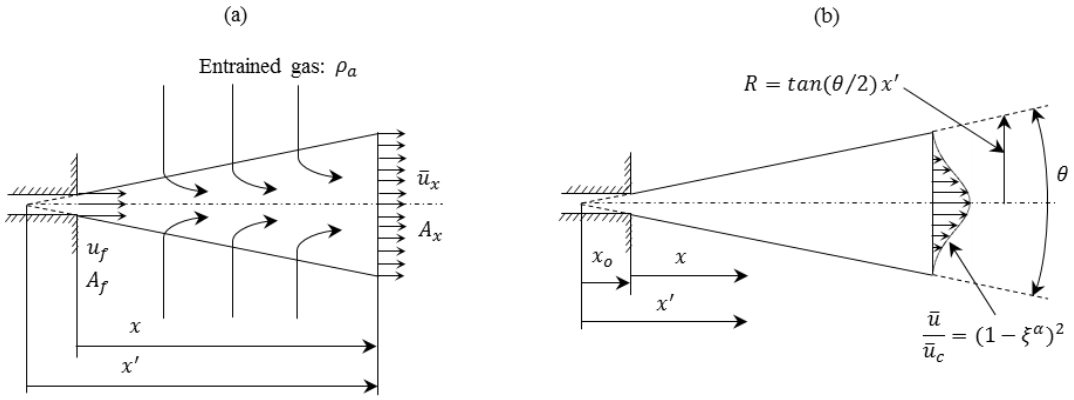

Figure 2.10. Key variables and parameters of the uniform mixture profile developed by Naber and Siebers [32] (a) and the variable mixture profile model of Musculus and Kattke [33] (b).

To provide a realistic radial distribution of fuel mass and velocity, the one-dimensional transient diesel jet model was developed by Musculus and Kattke [33] by extending the uniform-profile spray/jet model of Naber and Siebers [32]. The variable mixture profile model was validated by Pickett et al. [35] using quantitative experimental data on the fuel-vapor mass distribution in transient diesel sprays. A depiction of the variable mixture profile model and its key variables is shown in Figure 2.10 (b). The variable mixture profile model was used in the work presented in this thesis with a simplified analytical solution for the spray penetration (i.e. a constant-β solution). In the transition region, β varies linearly with the axial distance x. A fully variable-β solution would be identical to the 'exact' solution presented by Pickett et al. [35], but the resulting model would be much more computationally demanding, and the results obtained using the simplified solution were very close to the exact solutions for the downstream parts of the jet. Details of the full-variable β model and the exact solution can be found in Ref. [35]. By considering the conservation of the injected fuel momentum and mass, the cross-sectionally averaged fuel volume fraction $\bar{\bar{X}}_f$ can be related to the axial velocity u and the mass flow rate $\dot{m}_{f,o}$:

$$\bar{\bar{X}}_f = \frac{\dot{m}_{f,o}}{\rho_f \beta \bar{\bar{u}} A} \tag{2-5}$$

where the double overbars signify cross-sectionally averaged values, the subscript 'o' indicates conditions at the orifice exit, and $\dot{m}_f$, ρ_f and A are the mass flow rate, fuel density and cross-sectional area, respectively. For a fully developed jet, β = 105/52, but β varies in the transition region as discussed later. The cross-sectionally averaged velocity $\bar{\bar{u}}$ is

$$\bar{\bar{u}} = \dot{m}_{f,o} \frac{-\left(1-\frac{\rho_a}{\rho_f}\right) + \sqrt{(1-\frac{\rho_a}{\rho_f})^2 + 4\beta\frac{\rho_a}{\rho_f}\frac{A}{A_o}}}{2\beta\rho_a A} \tag{2-6}$$

where the ρ_a and A_o are the ambient gas density and the effective orifice flow area, respectively. A_o and the cross-sectional area A are defined as:

$$A_o = \frac{C_a \pi d_o^2}{4} \tag{2-7}$$

$$A = \pi R^2 = \pi(tan(\theta/2)x')^2 \tag{2-8}$$

where C_a is the measured area contraction coefficient, d_o is the diameter of the orifice exit, and θ is the spreading angle measured in the downstream part of the jet. Combining Equations (2-5) – (2-8) gives

$$\bar{\bar{X}}_f = \frac{2\frac{\rho_a}{\rho_f}}{-(1-\frac{\rho_a}{\rho_f}) + \sqrt{(1-\frac{\rho_a}{\rho_f})^2 + \frac{16\beta}{C_a}\frac{\rho_a}{\rho_f}\frac{(tan(\theta/2)x')^2}{d_o^2}}} \tag{2-9}$$

Using Equation (2-9), the $\bar{\bar{X}}_f$ can be calculated with respect to any distance from the nozzle tip. The centerline fuel volume fraction $\bar{X}_{f,c}$ is related to $\bar{\bar{X}}_f$ as

$$\bar{X}_{f,c} = \frac{(\alpha+1)(\alpha+2)}{\alpha^2}\bar{\bar{X}}_f \tag{2-10}$$

where α = 1.5 for a fully developed jet, and the subscript 'c' donates the value on the jet centerline. For the transition region, it will be discussed later. The turbulent mean fuel volume fraction $\bar{X}_f$ is related to $\bar{X}_{f,c}$ as

$$\frac{\bar{X}_f}{\bar{X}_{f,c}} = (1-\xi^{\alpha})^2 \tag{2-11}$$

where $\xi = r/R$, and $R = tan(\theta/2)\,x'$. Equation (2-11) can be used to compute the turbulent mean fuel volume fraction $\bar{X}_f$ at a given radial coordinate r. The local fuel-ambient mass ratio is defined as

$$\frac{m_f}{m_a} = \frac{\rho_f \bar{X}_f}{\rho_a(1-\bar{X}_f)} \tag{2-12}$$

We know that the stoichiometric fuel/air ratio $(m_f/m_a)_{st}$, for diesel fuel is 14.6. The local equivalence ratio can be calculated as:

$$\phi = \frac{m_f/m_a}{(m_f/m_a)_{st}} \tag{2-13}$$

For the transition region, according to Equations (B5) and (B6) in Ref. [35]:

$$\frac{A}{A_o} = \frac{(x_{tran}+x_o)^2}{(x_o)^2} = \frac{52}{27} + \frac{\rho_f}{\rho_a}\left(\frac{1352}{243}\right) \tag{2-14}$$

$$\beta = \frac{53}{52}\frac{x}{x_{tran}} + 1 \tag{2-15}$$

where $x_o = (d_o/2)cot(\theta/2)$. The transition distance x_{tran} can be obtained solving Equation (2-14), and β can be calculated at various axial distances x up to the transition distance x_{tran} using Equation (2-15). The parameter α is related to β as

$$\beta = \frac{6(\alpha+1)(\alpha+2)}{(3\alpha+2)(2\alpha+1)} \tag{2-16}$$

By solving Equation (2-16), one obtains a value of α for the transition region. The values of all unknown parameters can thus be calculated in the transition region, allowing the local equivalence ratio to be calculated in the same way as for the fully developed jet. Ultimately, this makes it possible to predict the local equivalence ratio across the entire jet. One of the most important inputs for the variable mixture profile model is the spreading angle. As suggested by Pickett et al. [35], an appropriate spreading angle for the model can be determined from the measured penetration; the relationship between the penetration length and the spreading angle is discussed in Ref. [35].

Pickett et al. [35] used the variable profile model for non-reacting jets to correlate the predicted local equivalence ratio in the lift-off region (which is discussed in the next section) with soot formation in the corresponding reacting jets. The ϕ_c values predicted in this way (which were <2) agreed very well with results for soot-free jets. This is reasonable at first glance, but it should be noted that there are important differences in air entrainment between reacting and non-reacting jets. In an early study, Han and Mungal [36] concluded that the air entrainment in the near field of turbulent reacting jets was around 2.5 times weaker (for a typical hydrocarbon fuel in air) than in a non-reacting jet. In addition, García-Oliver et al. [37] recently measured the air entrainment rate in reacting and non-reacting jets under diesel-like conditions. As shown in Figure 2.11 (a), even upstream of the lift-off length, the air entrainment rate was lower for the reacting jet than the non-reacting one. These authors concluded that this was due to the effect of large-scale flow recirculation (see Figure 2.11 (b)). Notably, the air-entrainment near the lift-length was significantly lower for the reacting jet than the non-reacting one. These observations suggest that air entrainment predictions based on results for non-reacting jets may overestimate the air entrainment for reacting jets, and that this should be accounted for when predicting local ϕ values for reacting jets.

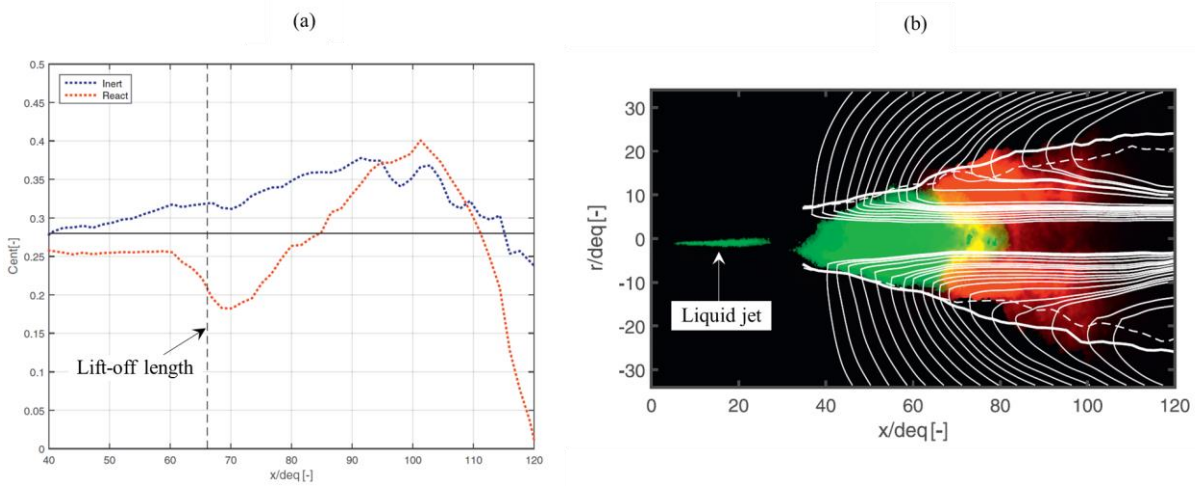

Figure 2.11. Air entrainment rates for the inert (non-reacting) and reacting jets averaged over 2800–4400 μs ASOI, and air entrainment streamlines for the reacting jet (b) at 1517 μs ASOI from the work of García-Oliver et al. [37] (reproduced with the permission). In the right hand figure (b), the red and green areas indicate regions where OH radicals and formaldehyde (HCHO) were detected, respectively. Overlaid contours are determined from 1% axial velocity for inert (dashed) and reacting (solid) jets. Experimental conditions: T_a = 780 K, ρ_a = 14.8 kg/m^3, P_{in} = 1500 bar, O_2 = 15%, n-dodecane, ρ_f = 703 kg/m^3, D_o = 0.0886 mm, dep = $D_o\sqrt{\rho_f/\rho_a}$.

In the studies presented in this thesis, the spreading angle for the variable profile model was predicted based on the reacting penetration length (which was determined by analyzing OH* chemiluminescence images). This was done because the reacting penetration length was reported to be about 10% longer than the non-reacting penetration length by Desantes et al. [37], as shown in Figure 2.12. It was found that an

increase of around 10% in the penetration reduced the spreading angle by around 25% when using the variable mixture model. Therefore, a reduction of around 25% in the air entrainment in the lift-off length region was factored in when predicting the local equivalence ratio using the variable profile model. Detailed descriptions of this approach are presented in appended Papers V and VI.

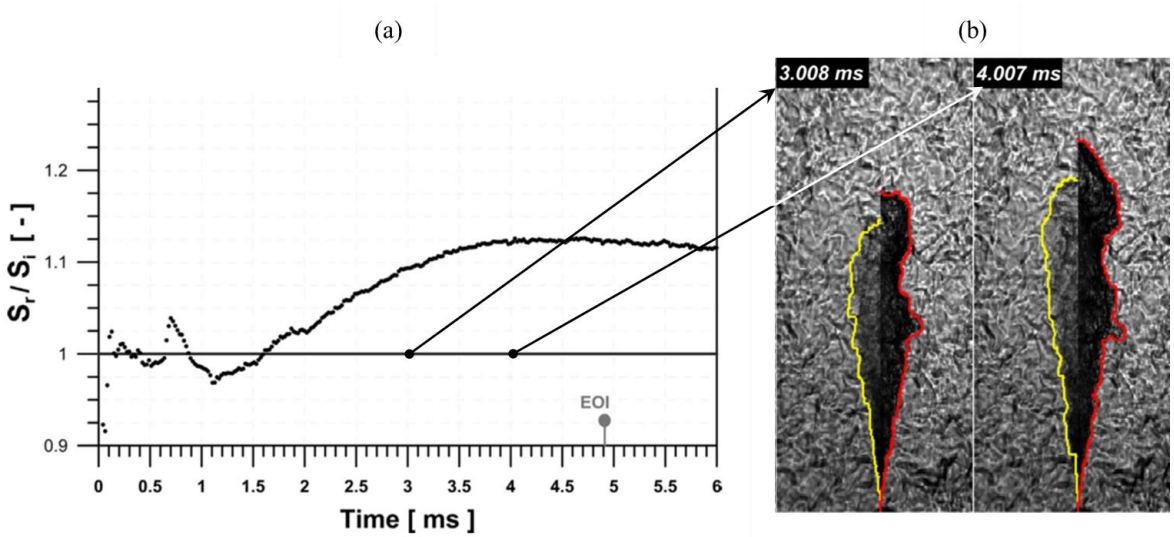

Figure 2.12. Comparison of the reacting penetration length ($\mathbf{S_r}$) and non-reacting ($\mathbf{S_i}$) penetration lengths (a), and comparison of a reacting jet contour (red) with a non-reacting jet contour (yellow) (b), from the work of Desantes et al.[38]. Experimental conditions: T_a = 826 K, ρ_a = 28.4 kg/m^3, P_{in} = 500 bar, n-heptane, D_o = 0.082 mm.

2.4 Lift-off length in reacting diesel sprays

In conventional diesel engines, after the auto-ignition (or premixed ignition) has occurred, the combustion is controlled by diffusion (i.e. it is mixing-controlled), meaning that the chemical reactions are much faster than the transport processes (e.g. mixing) and the rate of the combustion process is limited by the time required for mixing. During the diffusion combustion phase, the reacting diesel jet becomes a typical lifted turbulent diffusion flame. The lift-off of the flame allows the diesel fuel and air to be premixed before reaching the initial combustion region in the reacting diesel jet. This strongly affects the diesel combustion and emission processes. Therefore, it is very important to understand how lift-off affects reacting diesel jets. This section briefly introduces some key properties of lift-off phenomena in laboratory diffusion flames, to facilitate understanding of the behavior of the lift-off length in diesel flames. More detailed treatments of these topics can be found in reviews [39, 40] and the book by Peters [47].

Lawn [39] divided the published theories describing turbulent lifted flames into three groups based on their conceptual underpinnings: (a) the premixed model, (b) the extinction model (or the critical scaler dissipation model of Lyons [40]), and (c) the large eddy model. Lyons [40] further divided the premixed model (a) into turbulence intensity theory and the ‘edge flame’ concept. However, in an early paper [41] and a later review [39], Lawn concluded that the ‘premixed model’ should be adequate if the jet velocity is high enough to lift the flame to a height of at least around 20 times the orifice exit diameter (D_o). However, the large eddies generated by Kelvin-Helmholtz instabilities play a crucial role on the stabilization of lift-off lengths when lift-off lengths are less than 20 D_o. For conventional diesel sprays, D_o is in the range of 0.1-0.2 mm and the exit velocity is in the hundreds of meters per second, so the lift-off length is much greater than 20 D_o. Therefore, the premixed model can adequately stabilize the lift-off lengths of diesel sprays. It should be noted that if the stretch rate is high (see below), the influence of quenching should be accounted for, which can compete with the premixed model [39]. In the premixed model, as shown by the schematic in Figure 2.13, flame stabilization results from a balance between the

local jet velocity and the local turbulent premixed flame velocity, S_t, which is a function of the laminar flame velocity S_L.

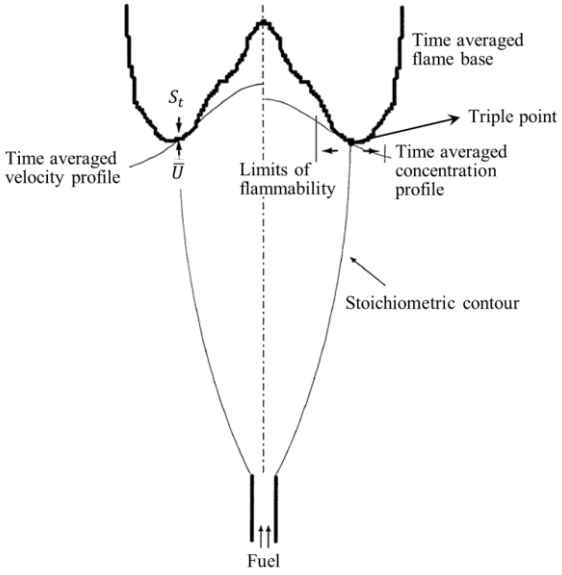

Figure 2.13. Schematic of a lifted diffusion flame from the work of Burgess and Lawn [41].

The expression for calculating the S_t was adapted from Ref. [41],

$$S_t = 0.875 u' K_a^{-0.392} \tag{2-17}$$

where u' is the RMS of the axial velocity fluctuations and K_a is the Karlovitz flame stretch factor, which can be evaluated as shown by Abdel-Gayed et al. [42]

$$K_a = 0.157 \left(\frac{u'}{S_L}\right)^2 Re_t^{-0.5} \tag{2-18}$$

Here, the Re_t is the local turbulent Reynolds number, $Re_t = u'L/v$, where L is the integral length scale and v is the kinematic viscosity. Equations (2-17) and (2-18) can be used to estimate the local turbulent velocity S_t of the mixture at the flame base; Burgess and Lawn [41] compared such estimates to the mean velocity of the turbulent eddies, U_{tur}, at the estimated radius of maximum flame velocity. For brevity, this section provides only a brief introduction to these concepts; more comprehensive descriptions can be found in Refs. [39, 41, 42]. Burgess and Lawn calculated S_t and U_{tur} values based on 200 published experimental measurements, and showed that $S_t/U_{tur} \approx 1.7$ (±40%) when the lift-off length is 20 D_o, decreasing to unity as the lift-off increases. This implies that the lift-off length stabilization is well-described by the premixed model when the lift-off length is > 20 D_o.

Several studies have investigated the lift-off lengths of reacting diesel sprays [38, 43-46] because soot formation is strongly dependent on the lift-off length. According to the scaling law proposed by Peters [47]

$$LOL \propto \frac{u_o Z_{st} D_{dif}}{S_L^2(Z_{st})} \tag{2-19}$$

where LOL is the measured lift-off length, Z_{st} is the stoichiometric fuel fraction, u_o is the fuel injection velocity at the orifice exit, $S_L(Z_{st})$ is the laminar flame velocity of a stoichiometric fuel-air mixture and

D_{dif} is the thermal diffusivity. Based on the scaling law shown in Equation (2-19), Siebers and coworkers [44, 45] derived the following equation for predicting the lift-off length for #2 diesel fuel:

$$LOL = CT_a^{-3.74}\rho_a^{-0.85}D_o^{0.34}u_o Z_{st}^{-1} \quad (2\text{-}20)$$

where C is a proportionality constant with a value of $7.04\cdot10^8$ [46]. The empirical Equation (2-20) was developed based on extensive experimental data obtained in a constant vessel (i.e. under quasi-steady conditions). For actual diesel engine conditions, Fuyuto et al. [48] found that the backward flow of hot burned gas shortened the lift-off length compared to that predicted by the single-free jet empirical Equation (2-20). This is mainly because the hot burned gases raise the temperature of the gas surrounding the spray. Lequien et al. [49] later added swirl and injector jet angle terms to Equation (2-20) based on experimental findings obtained using an optical heavy-duty diesel engine. It is thus clear that the form of the empirical Equation (2-20) is influenced by the boundary conditions.

2.5 Soot processes

In thermodynamic terms, soot formation should occur when, in

$$\mathrm{C}_m\mathrm{H}_n + y\mathrm{O}_2 = 2y\mathrm{CO} + \frac{n}{2}\mathrm{H}_2 + (m-2y)\mathrm{C}_s \quad (2\text{-}21)$$

the C/O ratio exceeds unity, i.e. m becomes larger than $2y$. In fact, the experimentally observed limiting C/O ratio is less than unity. The critical C/O for the soot formation has been found to range between 0.5 and 1 in Bunsen burner flames, flat flames, and stirred reactors [50], and depends on both the flame structure and the fuel type. Diesel fuel typically consists of compounds with 12-25 carbon atoms and a H/C of around 2. The critical fuel/air equivalence ratio (which can be related to the C/O ratio) can be estimated using the following expression [51]:

$$\phi = 2\left(\frac{\mathrm{C}}{\mathrm{O}}\right)(1+2\delta) \quad (2\text{-}22)$$

Here, $\delta = n/(4m)$. Using an extensive experimental data set, Siebers and Higgins [44] showed that the soot incandescence disappeared when the predicted cross-sectional average equivalence ratio at the lift-off length, ϕ_{LOL}, was in the range of 1.8-2.2 for #2 diesel fuel. This corresponds to a C/O range of 0.62-0.76 with $n/m = 1.8$.

The empirical Equation (2-21) is useful for identifying C/O conditions under which soot may form, but the soot formation process is rather complicated and the detailed mechanisms involved are not yet understood. Interested readers are referred to three excellent review articles on this topic [50, 52, 53]. Here, we briefly describe the soot formation process. Soot formation is commonly described as a stepwise process involving six distinct stages: fuel pyrolysis, nucleation, coagulation, surface growth, aggregation, and oxidation. Figure 2.14 shows the key known pathways of soot formation that are relevant in diesel combustion (adapted from the work of Smith [52]). Oxidation may occur in parallel to all of these soot formation processes, causing the hydrocarbons to be converted into CO, CO_2 and H_2O [54]. The growth steps involving large aromatic structures that lead to soot nucleation were found to be significantly faster than the initial ring formation steps [55]. Therefore, the formation of the initial aromatic rings (i.e. one- and two-ring structures) plays a significant role in controlling the rate of soot formation [56]. This implies that it is important to suppress the initial steps of soot formation by efficiently oxidizing fuel molecule species [52].

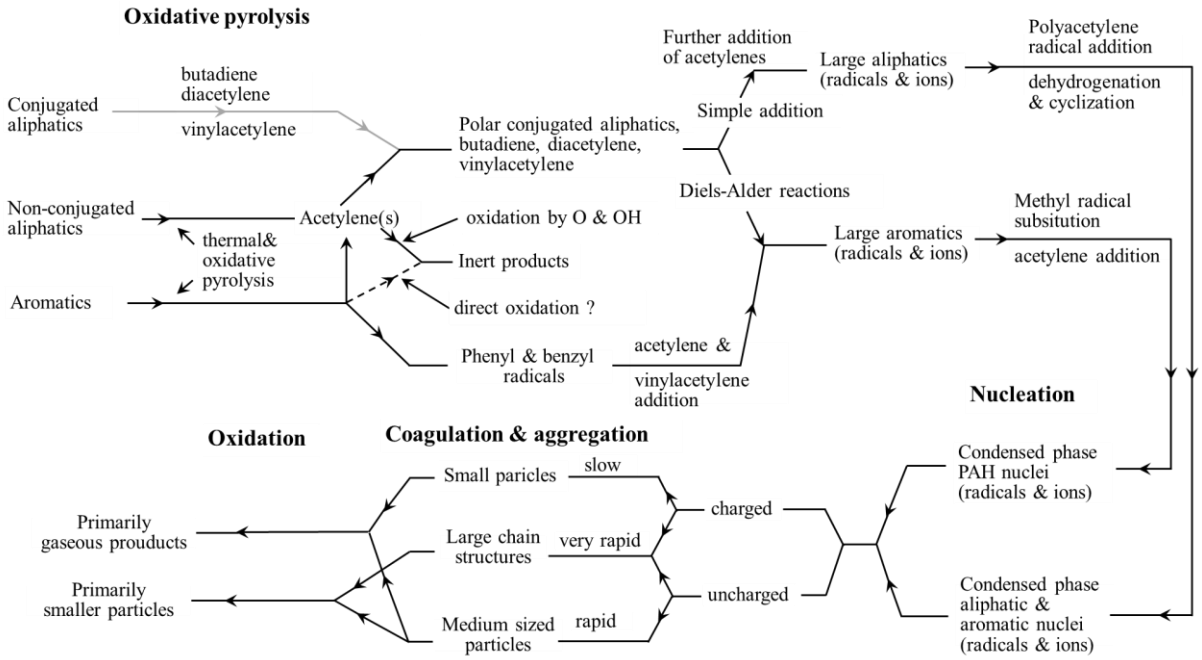

Figure 2.14. Key processes in soot formation, adapted from the work of Smith [52].

Fuel pyrolysis is an endothermic process that is highly temperature-dependent. At high temperatures, non-conjugated aliphatic fuel molecules are converted into acetylene by thermal oxidative pyrolysis; acetylene is the last stable acyclic molecular species on the pathway that leads to the initial formation of aromatic rings. During this process, if enough O and OH are present, some acetylene will be oxidized to relatively inert products [52]. It should be noted that the levels of O and OH in flames are temperature-dependent: soot formation in premixed flames decreases as the temperature increases, but the opposite is true in diffusion flames because of the lack of oxidizing species in the latter case [52, 56]. At high temperatures, aromatic fuels pyrolyze by ring fracture to form acetylene; at low temperatures, they quickly form aromatic rings (soot precursors). Soot particles are formed by the gradual addition of mass to soot precursors. During the processes of coalescence and agglomeration, soot particles combine to form chain-like structures with sizes ranging from 100 nm to 2 μm. The ultimate emissions of soot particles are much lower than the total quantity produced in the engine because many of the formed soot particles are quickly oxidized. As noted above, the oxidation of soot precursors and particles may occur in regions of the flame where oxidizing species are present. An important process in soot oxidation is the attack of OH radicals on soot. As stated by Haynes and Wagner [50], soot oxidation is primarily controlled by OH; O_2 is only expected to be an important oxidant under very lean conditions, which yield very low OH concentrations at lower temperatures. This is consistent with the results of experimental observations of diesel flames.

Reacting diesel jets are very turbulent, and turbulence affects soot formation and oxidation in various ways. An early study by Magnussen [57] found that the amount of soot in a turbulent flame could not be predicted simply by applying a laminar rate equation. This was attributed to the turbulent interactions between eddies containing oxygen and soot particles' surfaces. Recent studies using direct numerical simulation (DNS) [58, 59], and experimental work [60] showed that soot formation and growth are strongly affected by turbulent factors such as soot transportation and fluid convection.

There are several practical ways of reducing soot formation in diesel flames. One is to reduce the ϕ_{LOL}, which was found to reduce the soot volume fraction. It should be noted that a decrease in the ambient temperature would reduce ϕ_{LOL}. However, detailed physical and chemical mechanism modeling performed by Kitamura et al. [61] suggested that extensive formation of fine particles (with diameters below 10 nm) would occur at lower temperatures, but that the amount of particles would decrease steeply (and the diameter of the remaining particles would increase sharply) once the temperature exceeded 1800-1900 K. They therefore suggested that leaner mixtures (i.e. mixtures with lower ϕ values) should be used to suppress soot formation while maintaining a suitable temperature. For a reacting diesel flame, this would necessitate an increased injection pressure (and thus a higher jet velocity) or a decrease in the orifice exit diameter to reduce the local ϕ. Another approach is to use oxygenated fuels because it was shown that oxygenated fuel reduced the inception and number density of soot particles [61]. Reducing the oxygen concentration (simulating EGR in an engine) is another viable approach: it was found that soot formation declined with the oxygen concentration [62, 63]. However, this would also increase the size of the soot aggregates by suppressing soot oxidation [62].

2.6 Conceptual models of reacting diesel jets

Several conceptual models of reacting diesel jets have been proposed [64-68], and the development and elaboration of these models has substantially improved our understanding of reacting diesel jets. This section reviews some conceptual models relevant to conventional [64, 65] and low temperature [66, 67] operating conditions that are helpful for understanding fundamental combustion phenomena in mixing-controlled reacting diesel jets. Musculus et al. [68] recently proposed a conceptual model for partially premixed low-temperature diesel combustion, which is not discussed here. In addition, the discussion focuses on the models' descriptions of the typical mixing controlled period; discussions of the premixed combustion phase (or auto-ignition phase) can be found in Refs. [64-67].

In early 1997, Dec proposed a conceptual model [64] for reacting diesel jets formed under conventional diesel operating conditions such as might result from a single injection through an orifice diameter of ~0.2 mm with no EGR and fuel injection occurring shortly before top dead center (TDC). This model is depicted in Figure 2.15 (a). During the mixing-controlled period, the diffusion flame (formed under near-stoichiometric conditions) remains some distance from the nozzle tip, exhibiting a typical lift-off length for a lifted turbulent reacting jet. The liquid jet's penetration also establishes some distance from the nozzle tip because the injected liquid fuel entrains the surrounding hot and highly pressurized gas, rapidly vaporizing the liquid fuel (i.e. the rate of fuel vaporization is limited by the mixing). In the downstream region of the liquid spray, the fuel-rich premixed reaction (shown in light blue) coincides with the region where the equivalence ratio is 3-5 and the temperature is above 1600 K. Under such conditions, soot precursors (PAH) form and soot particles become distributed across the entire jet, producing high soot concentrations in the jet head. Dec also predicted the soot oxidation occurs only in the thin diffusion flame zone, as a result of OH radical attack. This stands in contrast to the conceptual model of Kosaka et al. [66], which is discussed in the next paragraph. In Dec's model, the vapor phase fuel mixture occupies the region between the liquid phase tip and fuel-rich premixed flame. However, later on, under low-soot and moderate sooting conditions, Idicheria and Pickett [65] observed that a cool flame (evidenced by the formation of formaldehyde, HCHO) exists prior to the fuel-rich premixed flame, as shown in Figure 2.15 (b). Under low sooting conditions, the formaldehyde was consumed by the fuel-rich premixed flame, and the soot precursors and soot form just downstream of the fuel-rich premixed reaction. In the jet center under moderate sooting conditions, the consumption of formaldehyde by the fuel-rich premixed reaction occurs in parallel with PAH formation. An interesting point not shown in Figure 2.15 (a) is that

the soot particle size increases on moving downstream along the jet, while the soot number density decreases.

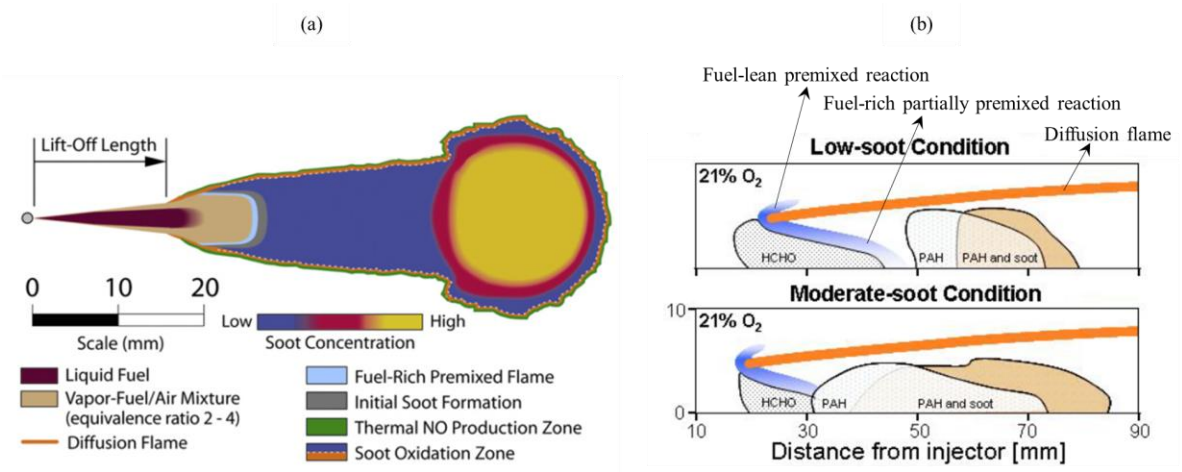

Figure 2.15. Depiction of Dec's conceptual model during the mixing controlled period (a) from the work of Dec [64], and a conceptual model of HCHO, PAH and soot formation at the lift-off region under low and moderate sooting conditions (b) from the work of Idicheria and Pickett [65].

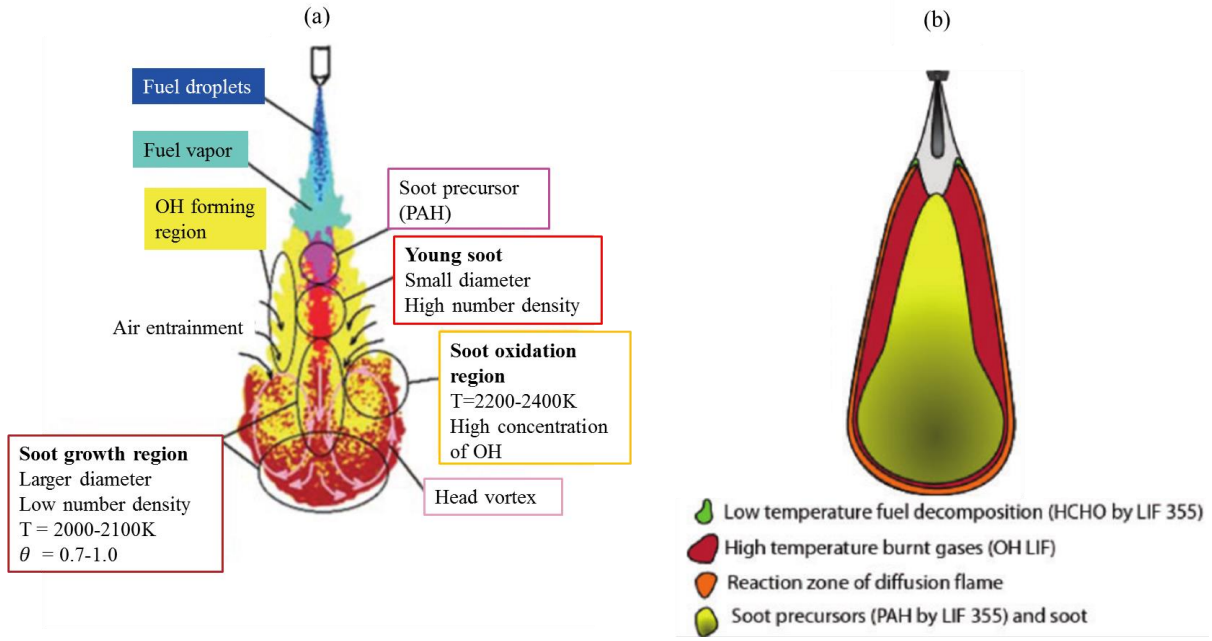

Figure 2.16. Conceptual model of the soot formation and oxidation (a) from the work of Kosaka et al. [66], and conceptual model of HCHO, OH radicals, PAH, and soot formation (b) from the work of Bruneaux [67].

In the conceptual models proposed by Kosaka et al. [66] and Bruneaux [67], the liquid phase penetration is shorter than the lift-off length. This differs with Dec's model that the liquid phase penetration is longer than the lift-off length. This difference is mostly likely due to a smaller orifice diameter (0.15 mm) and a lower ambient temperature operating conditions implemented by Kosaka et al. [66] and Bruneaux [67]. In both conceptual models (see Figure 2.16), a thick OH zone exists around the sooting zone, and the soot

particles are oxidized (or attacked) by OH radicals, rather than the very thin diffusion flame proposed by Dec. Kosaka et al. also proposed the existence of a vortex in the jet head, which transports the soot particles into the lean side of jet, where they are oxidized by the high concentration of OH radicals. Soot oxidation in the jet head consistent with this model was observed in the experimental studies presented in this thesis. Kosaka et al. also described the evolution of the soot particle size and number density along the jet's axis. Unlike the conceptual models developed by Idicheria and Pickett (see Figure 2.15 (b)) and Bruneaux (see Figure 2.16 (b)), formaldehyde is not included in the conceptual model of Kosaka et al. (see Figure 2.16 (a)). In addition, formaldehyde is formed in the jet center in the conceptual model shown in Figure 2.15 (b), but no formaldehyde region exists in Figure 2.16 (b). This difference probably reflects the conceptual model affected by operating conditions.

The conceptual models discussed above have greatly enhanced our understanding of diesel combustion during the mixing controlled phase. However, each of these models on the basis of different operating conditions with respect to variables such as the orifice exit diameter and the use of low-sooting fuel or pure single-component fuels, low or high ambient temperatures, and the injection pressures. This is important because the operating conditions strongly influence the combustion characteristics. Further work is needed to improve and extend existing conceptual models to account for a wider range of operating conditions, phenomena such as swirl flow in the engine, and the use of oxygenated fuel.

2.7 Combustion modes on the $\phi - T$ coordinate map

The mechanism of soot formation in diesel sprays is discussed at length above. However, soot is not the only important pollutant produced by diesel engines: NO_x emissions are another very important kind of air pollution. The formation of soot and NO_x in diesel engines can be analyzed using $\phi - T$ coordinate maps, which are useful for understanding the process of combustion and the formation of emissions. Figure 2.17 shows a using $\phi - T$ coordinate map for conventional diesel combustion. After the premixed combustion phase, the mapped system enters a typical mixing-controlled combustion phase. During this period, soot is formed in the region where the combustion temperature is high (over 1600 K) and the ϕ is above the soot formation threshold of 2.0. In addition, NO_x is formed when the combustion temperature is high. Low temperature combustion provides a way of minimizing the emissions of these two pollutants. This can be achieved through efficient premixing of the fuel and gas before the start of combustion, and by ensuring that the local ϕ is below unity throughout the combustion chamber. Combustion under these conditions is known as homogeneous charge compression ignition (HCCI). In HCCI combustion strategies, the ignition time is kinetically controlled, and is thus decoupled from the fuel injection timing. Unfortunately, current HCCI combustion strategies produce high CO and HC emission and are only applicable over a limited load range. However, if the fuel and gas are well premixed upstream of the lift-off length region where the local ϕ is sufficiently lean, this combustion mode can eliminate soot emissions while producing only very small quantities of NO_x [70]. This strategy can be implemented by using a small injector orifice diameter with a low ambient oxygen concentration (as low as 10%) or by reducing the ambient gas temperature to around 850 K [70]. Such combustion mode is achieved in this work using an injector with a small orifice diameter coupled with high injection pressures at low ambient temperature (823 K), the results are shown in the Appended Paper VI. Another class of low temperature combustion strategies are modulated kinetics (MK) combustion strategies [71], which use a moderate EGR rate with a retarded injection timing and a low compression ratio. This approach has been shown to strongly reduce NO_x and particulate matter emissions [71]. It should also be noted that the preceding discussion assumes that there is a fixed soot formation threshold; in reality, soot formation is strongly dependent on the fuel type. The use of highly oxygenated fuels could increase the ϕ required for soot formation [61], making it easier to achieve soot-free diesel combustion. There are also a number of other strategies for simultaneously reducing soot formation and NOx emissions that are not discussed here; the aim of this section was to briefly introduce

some of the most important and widely studied combustion modes for achieving low soot and NOx emissions in diesel engines rather than to provide a comprehensive overview of the field.

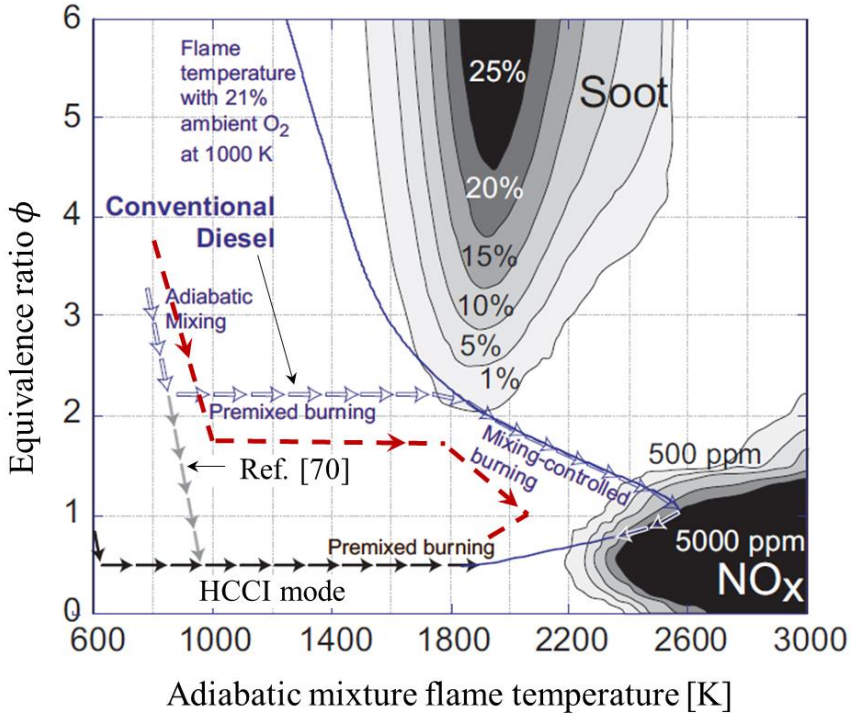

Figure 2.17. Different combustion modes on a $\phi - T$ coordinate map from the work of Kook et al. [69]. The simulation of soot and NO_x formation regimes in $\phi - T$ coordinates is from Ref. [61]. The simulation was performed for n-heptane at an ambient pressure of 60 bar with a reaction time of 2 ms. Soot contours are soot yields expressed as the percentage of fuel carbon converted into soot. The dark red dashed line is the low temperature combustion mode referred to in the work of Kimura et al. [71]. The dark blue solid line overlaid is the maximum flame temperature for a liquid fuel temperature of 373 K at an ambient temperature of 1000 K with 21% O_2.

References

[1] Brennen, C. E. (2013). Cavitation and bubble dynamics. *Cambridge University Press*.

[2] Pasadakis, N., Sourligas, S., & Foteinopoulos, C. (2006). Prediction of the distillation profile and cold properties of diesel fuels using mid-IR spectroscopy and neural networks. *Fuel*, *85*(7), 1131-1137.

[3] Duke, D., Swantek, A., Tilocco, Z., Kastengren, A., Fezzaa, K., Neroorkar, K., & Schmidt, D. (2014). X-ray imaging of cavitation in diesel injectors. *SAE International Journal of Engines*, 7(2014-01-1404), 1003-1016.

[4] Giannadakis, E., Gavaises, M., & Arcoumanis, C. (2008). Modelling of cavitation in diesel injector nozzles. *Journal of Fluid Mechanics*, 616, 153-193.

[5] König, G. & Blessing, M. 2000 Database of cavitation effects in nozzles for model verification: geometry and pressure effects on cavitating nozzle flow. *DaimlerChrysler AG*.

[6] Andriotis, A., Gavaises, M., & Arcoumanis, C. (2008). Vortex flow and cavitation in diesel injector nozzles. *Journal of Fluid Mechanics*, *610*, 195-215.

[7] Gavaises, M., Andriotis, A., Papoulias, D., Mitroglou, N., & Theodorakakos, A. (2009). Characterization of string cavitation in large-scale Diesel nozzles with tapered holes. *Physics of fluids*, *21*(5), 052107.

[8] Mitroglou, N., McLorn, M., Gavaises, M., Soteriou, C., & Winterbourne, M. (2014). Instantaneous and ensemble average cavitation structures in Diesel micro-channel flow orifices. *Fuel*, *116*, 736-742.

[9] Blessing, M., Konig, G., Kruger, C., Michels, U., & Schwarz, V. (2003, May). Analysis of flow and cavitation phenomena in diesel injection nozzles and its effects on spray and mixture formation. In *Fuel Injection Systems 2003: IMechE Conference Transactions* 2003 (Vol. 2, p. 21).

[10] Badock, C., Wirth, R., Fath, A., & Leipertz, A. (1999). Investigation of cavitation in real size diesel injection nozzles. *International journal of heat and fluid flow*, *20*(5), 538-544.

[11] Chaves, H., Knapp, M., Kubitzek, A., Obermeier, F., & Schneider, T. (1995). Experimental study of cavitation in the nozzle hole of diesel injectors using transparent nozzles (No. 950290). *SAE technical paper*.

[12] Chaves, H., Knapp, M., Kubitzek, A., & Obermeier, F. (1993, August). High-speed flow measurements within an injection nozzle. In *Laser Anemometry: Advances and Applications--Fifth International Conference* (pp. 265-272). International Society for Optics and Photonics.

[13] Sou, A., Hosokawa, S., & Tomiyama, A. (2007). Effects of cavitation in a nozzle on liquid jet atomization. *International journal of heat and mass transfer*, *50*(17), 3575-3582.

[14] Arcoumanis, C., Flora, H., Gavaises, M., & Badami, M. (2000). *Cavitation in real-size multi-hole diesel injector nozzles* (No. 2000-01-1249). *SAE Technical Paper*.

[15] Soteriou, C., Andrews, R., & Smith, M. (1995). Direct injection diesel sprays and the effect of cavitation and hydraulic flip on atomization (No. 950080). *SAE technical paper*.

[16] Reitz, R. D. (1978). Atomization and other breakup regimes of a liquid jet. *Ph.D. Thesis*, Princeton University.

[17] Reitz, R. D., & Bracco, F. B. (1979). On the dependence of spray angle and other spray parameters on nozzle design and operating conditions (No. 790494). *SAE technical paper*.

[18] Hiroyasu, H., & Arai, M. (1990). Structures of fuel sprays in diesel engines (No. 900475). *SAE Technical Paper*.

[19] Leick, P., Riedel, T., Bittlinger, G., Powell, C. F., Kastengren, A., & Wang, J. (2007). X-ray measurements of the mass distribution in the dense primary break-up region of the spray from a standard multi-hole common-rail diesel injection system. In *21st Annual ILASS-Europe Conference, Mugla, Turkey*.

[20] Paciaroni, M., Hall, T., Delplanque, J. P., & Parker, T. (2006). Single-shot two-dimensional ballistic imaging of the liquid core in an atomizing spray. *Atomization and sprays*, 16(1).

[21] Dumouchel, C. (2008). On the experimental investigation on primary atomization of liquid streams. *Experiments in fluids*, *45*(3), 371-422.

[22] Baumgarten, C. (2006). Mixture formation in internal combustion engines. *Springer Science & Business Media*.
[23] Ashgriz, N. (Ed.). (2011). Handbook of atomization and sprays: theory and applications. *Springer Science & Business Media*.
[24] Som, S., & Aggarwal, S. K. (2010). Effects of primary breakup modeling on spray and combustion characteristics of compression ignition engines. *Combustion and Flame*, 157(6), 1179-1193.
[25] Moon, S., Gao, Y., Park, S., Wang, J., Kurimoto, N., & Nishijima, Y. (2015). Effect of the number and position of nozzle holes on in-and near-nozzle dynamic characteristics of diesel injection. *Fuel*, *150*, 112-122.
[26] Linne, M. (2013). Imaging in the optically dense regions of a spray: a review of developing techniques. *Progress in Energy and Combustion Science*, *39*(5), 403-440.
[27] Faeth, G. M., Hsiang, L. P., & Wu, P. K. (1995). Structure and breakup properties of sprays. *International Journal of Multiphase Flow*, *21*, 99-127.
[28] Chryssakis, C. A., Assanis, D. N., & Tanner, F. X. (2011). Atomization models. In *Handbook of Atomization and Sprays* (pp. 215-231). Springer US.
[29] Faeth, G. M. (2002). Dynamics of secondary drop breakup rate controlling processes in dense sprays. *Ilasse-Erope 2002, Zaragoza, September*.
[30] Chryssakis, C., & Assanis, D. N. (2008). A unified fuel spray breakup model for internal combustion engine applications. *Atomization and Sprays*, *18*(5).
[31] Wakuri, Y., Fujii, M., Amitani, T., & Tsuneya, R. (1960). Studies on the penetration of fuel spray in a diesel engine. *Bulletin of JSME*, *3*(9), 123-130.
[32] Naber, J. D., & Siebers, D. L. (1996). Effects of gas density and vaporization on penetration and dispersion of diesel sprays (No. 960034). *SAE technical paper*.
[33] Musculus, M. P., & Kattke, K. (2009). Entrainment waves in diesel jets. *SAE International Journal of Engines*, *2*(2009-01-1355), 1170-1193.
[34] Siebers, D. L. (1999). Scaling liquid-phase fuel penetration in diesel sprays based on mixing-limited vaporization (No. 1999-01-0528). *SAE technical paper*.
[35] Pickett, L. M., Manin, J., Genzale, C. L., Siebers, D. L., Musculus, M. P., & Idicheria, C. A. (2011). Relationship between diesel fuel spray vapor penetration/dispersion and local fuel mixture fraction. *SAE International Journal of Engines*, 4(2011-01-0686), 764-799.
[36] Han, D., & Mungal, M. G. (2001). Direct measurement of entrainment in reacting/nonreacting turbulent jets. *Combustion and flame*, *124*(3), 370-386.
[37] García-Oliver, J. M., Malbec, L. M., Toda, H. B., & Bruneaux, G. (2017). A study on the interaction between local flow and flame structure for mixing-controlled Diesel sprays. *Combustion and Flame*, *179*, 157-171.
[38] Desantes, J. M., Pastor, J. V., García-Oliver, J. M., & Briceño, F. J. (2014). An experimental analysis on the evolution of the transient tip penetration in reacting Diesel sprays. *Combustion and Flame*, *161*(8), 2137-2150.
[39] Lawn, C. J. (2009). Lifted flames on fuel jets in co-flowing air. *Progress in Energy and Combustion Science*, *35*(1), 1-30.
[40] Lyons, K. M. (2007). Toward an understanding of the stabilization mechanisms of lifted turbulent jet flames: experiments. *Progress in Energy and Combustion Science*, 33(2), 211-231.
[41] Burgess, C. P., & Lawn, C. J. (1999). The premixture model of turbulent burning to describe lifted jet flames. *Combustion and Flame*, *119*(1), 95-108.
[42] Abdel-Gayed, R. G., Bradley, D., & Lawes, M. (1987, December). Turbulent burning velocities: a general correlation in terms of straining rates. In *Proceedings of the Royal Society of London A: Mathematical, Physical and Engineering Sciences* (Vol. 414, No. 1847, pp. 389-413). The Royal Society.
[43] Chomiak, J., & Karlsson, A. (1996, January). Flame liftoff in diesel sprays. In *Symposium (International) on Combustion* (Vol. 26, No. 2, pp. 2557-2564). Elsevier.

[44] Siebers, D. L., & Higgins, B. (2001). Flame lift-off on direct-injection diesel sprays under quiescent conditions (No. 2001-01-0530). *SAE Technical Paper*.
[45] Siebers, D. L., Higgins, B., & Pickett, L. (2002). Flame lift-off on direct-injection diesel fuel jets: oxygen concentration effects (No. 2002-01-0890). *SAE Technical Paper*.
[46] Pickett, L. M., Siebers, D. L., & Idicheria, C. A. (2005). Relationship between ignition processes and the lift-off length of diesel fuel jets (No. 2005-01-3843). *SAE Technical Paper*.
[47] Peters, N. (2000). Turbulent combustion. *Cambridge university press*.
[48] Fuyuto, T., Hattori, Y., Yamashita, H., Toda, N., & Mashida, M. (2016). Set-off length reduction by backward flow of hot burned gas surrounding high-pressure diesel spray flame from multi-hole nozzle. *International Journal of Engine Research*, 1468087416640429.
[49] Lequien, G., Li, Z., Andersson, O., & Richter, M. (2015). Lift-Off Length in an Optical Heavy-Duty Diesel Engine: Effects of Swirl and Jet-Jet Interactions. *SAE International Journal of Engines*, 8(2015-24-2442), 2188-2198.
[50] Haynes, B. S., & Wagner, H. G. (1981). Soot formation. *Progress in energy and combustion science*, *7*(4), 229-273.
[51] Heywood, J. B. (1988). Internal combustion engine fundamentals (Vol. 930). *New York: Mcgraw-hill*.
[52] Smith, O. I. (1981). Fundamentals of soot formation in flames with application to diesel engine particulate emissions. *Progress in Energy and Combustion Science*, *7*(4), 275-291.
[53] Richter, H., & Howard, J. B. (2000). Formation of polycyclic aromatic hydrocarbons and their growth to soot—a review of chemical reaction pathways. *Progress in Energy and Combustion science*, *26*(4), 565-608.
[54] Tree, D. R., & Svensson, K. I. (2007). Soot processes in compression ignition engines. *Progress in Energy and Combustion Science*, *33*(3), 272-309.
[55] Stein, S. (1978). On the high temperature chemical equilibria of polycyclic aromatic hydrocarbons. *The Journal of Physical Chemistry*, 82(5), 566-571.
[56] Glassman, I., Yetter, R. A., & Glumac, N. G. (2014). Combustion. *Academic press*.
[57] Magnussen, B. F. (1971, January). The rate of combustion of soot in turbulent flames. *In Symposium (International) on Combustion* (Vol. 13, No. 1, pp. 869-877). Elsevier.
[58] Bisetti, F., Blanquart, G., Mueller, M. E., & Pitsch, H. (2012). On the formation and early evolution of soot in turbulent nonpremixed flames. *Combustion and Flame*, 159(1), 317-335.
[59] Attili, A., Bisetti, F., Mueller, M. E., & Pitsch, H. (2014). Formation, growth, and transport of soot in a three-dimensional turbulent non-premixed jet flame. *Combustion and Flame*, 161(7), 1849-1865.
[60] Qamar, N. H., Alwahabi, Z. T., Chan, Q. N., Nathan, G. J., Roekaerts, D., & King, K. D. (2009). Soot volume fraction in a piloted turbulent jet non-premixed flame of natural gas. *Combustion and Flame*, *156*(7), 1339-1347.
[61] Kitamura, T., Ito, T., Senda, J., & Fujimoto, H. (2002). Mechanism of smokeless diesel combustion with oxygenated fuels based on the dependence of the equivalence ration and temperature on soot particle formation. *International Journal of Engine Research*, *3*(4), 223-248.
[62] Kuribayashi, M., Mizutani, Y., Ishizuka, Y., Taki, N., & Aizawa, T. (2014). Effects of ambient oxygen concentration on soot processes in diesel spray flame-A qualitative comparison between TEM analysis and LII/Scattering laser measurements. *SAE International Journal of Fuels and Lubricants*, *7*(2014-01-2642), 693-703.
[63] Pickett, L. M., Caton, J. A., Musculus, M. P. B., & Lutz, A. E. (2006). Evaluation of the equivalence ratio-temperature region of diesel soot precursor formation using a two-stage Lagrangian model. *International Journal of Engine Research*, *7*(5), 349-370.
[64] Dec, J. E. (1997). A conceptual model of DI diesel combustion based on laser-sheet imaging (No. 970873). *SAE Technical paper*.
[65] Idicheria, C. A., & Pickett, L. M. (2006). Formaldehyde visualization near lift-off location in a diesel jet (No. 2006-01-3434). *SAE Technical Paper*.

[66] Kosaka, H., Aizawa, T., & Kamimoto, T. (2005). Two-dimensional imaging of ignition and soot formation processes in a diesel flame. *International Journal of Engine Research*, *6*(1), 21-42.
[67] Bruneaux, G. (2008). Combustion structure of free and wall-impinging diesel jets by simultaneous laser-induced fluorescence of formaldehyde, poly-aromatic hydrocarbons, and hydroxides. *International Journal of Engine Research*, *9*(3), 249-265.
[68] Musculus, M. P., Miles, P. C., & Pickett, L. M. (2013). Conceptual models for partially premixed low-temperature diesel combustion. *Progress in Energy and Combustion Science*, *39*(2), 246-283.
[69] Kook, S., Bae, C., Miles, P. C., Choi, D., & Pickett, L. M. (2005). The influence of charge dilution and injection timing on low-temperature diesel combustion and emissions (No. 2005-01-3837). *SAE Technical Paper*.
[70] Pickett, L. M., & Siebers, D. L. (2004). Non-sooting, low flame temperature mixing-controlled DI diesel combustion (No. 2004-01-1399). *SAE Technical Paper*.
[71] Kimura, S., Aoki, O., Kitahara, Y., & Aiyoshizawa, E. (2001). Ultra-clean combustion technology combining a low-temperature and premixed combustion concept for meeting future emission standards (No. 2001-01-0200). *SAE Technical Paper*.

Chapter 3

Experimental methods

Chapter 2 introduced the fundamental physics governing the evolution of sprays. To investigate the effect of various parameters on the spray characteristics under reacting and non-reacting conditions, a high pressure / high temperature (HP/HT) chamber and various optical diagnostic methods were used in the papers presented in this thesis. This chapter begins with a brief description of the HP/HT spray chamber and then presents the optical methods used in the appended papers.

3.1 HP/HT spray chamber

A continuous flow type chamber was used to generate diesel-like conditions. An advantage of using a continuous flow type chamber is that many injections can be performed within a short period of time once the desired experimental conditions have been established. A schematic of the spray chamber is presented in Figure 3.1. As can be seen in the cross-section shown in Figure 3.1 (b), pressurized air (up to 100 bar) from a compressor flows through the two 15 KW heaters, allowing the air to be heated to as much as 900 K. In all studies other than those described in appended papers IV and VII, the injector was mounted at the bottom of the spray chamber as shown Figure 3.1 (b). The velocity of the air flow was maintained at less than ~ 1 m /s, which is much smaller than the velocity of fuel injection (over a few hundred meters per second). The flow inside the spray chamber can thus be considered to be in a quasi-steady state. A detailed description of chamber is presented in appended Paper VII.

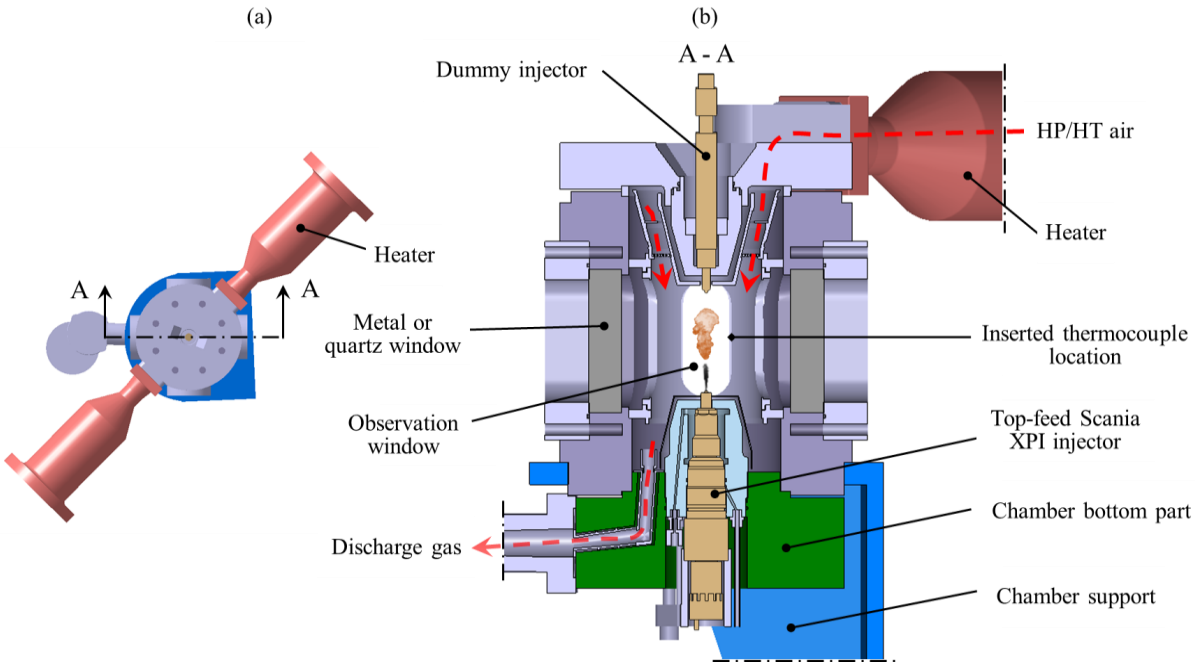

Figure 3.1. Top-view of the spray chamber with a small scale (a) and cross-sectional view of the spray chamber with a large scale (b).

3.2 Optical arrangement and line-of-sight technique

The spray chamber is compatible with a range of different optical methods for studying different variables. Figure 3.2 shows a real experimental set-up for conducting measurements under reacting conditions, featuring a continuous 532 nm Nd:YAG laser beam that was aligned for measuring the soot concentration by the laser extinction method. Filters and mirrors were arranged in front of cameras to collect desired light wavelength intensities on a high speed video CMOS cameras and a CCD camera. A schematic of the optical set-up corresponding to Figure 3.2 is shown in Figure 5.3 and described in Chapter 5.

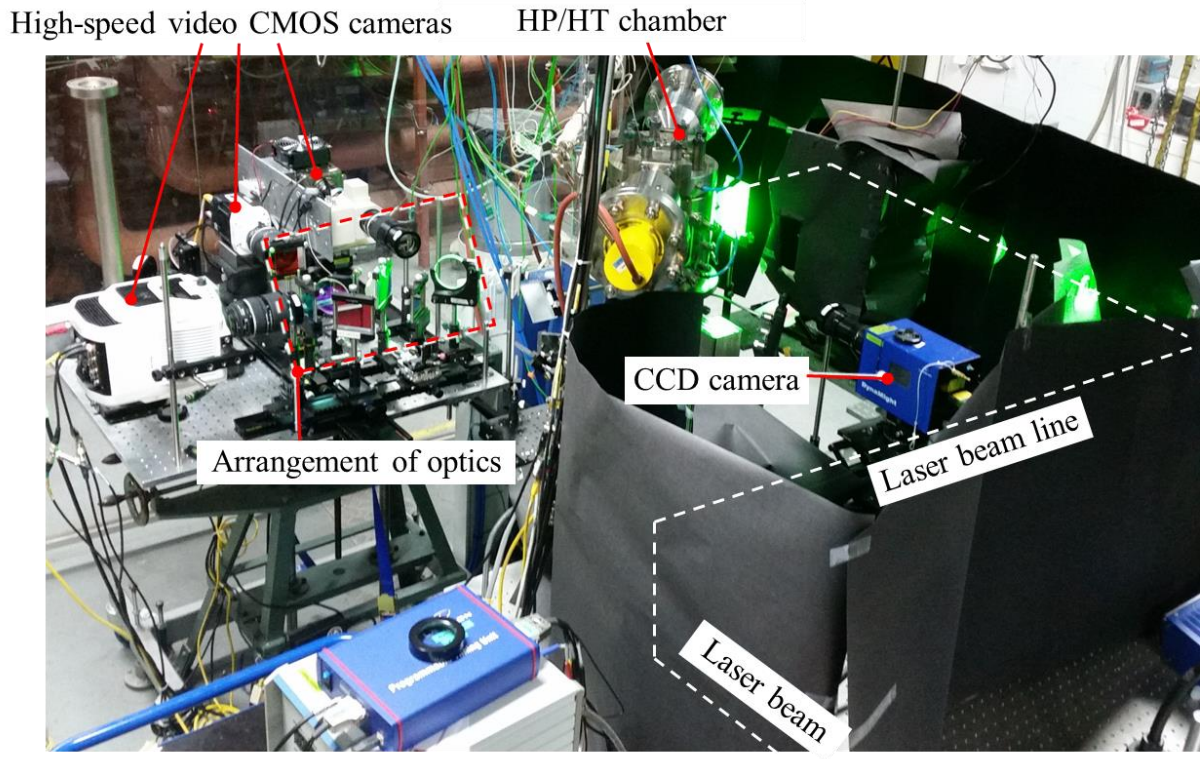

Figure 3.2. An experimental set-up used to study reacting jets.

Because several line-of-sight techniques were used in this thesis, a brief introduction of line-of-sight techniques is given. Line-of-sight techniques collect the light emission or absorption along the entire spray. Tomographic techniques thereby necessitate reconstructions of spatially resolved spray parameters. If one assumes the field distribution in the spray is cylindrically symmetrical, the Abel inversion can be used to reconstruct the spatial distribution of spray parameters, e.g. the soot volume fraction and OH radical distribution in the reacting sprays in this thesis. In this thesis, a three point Abel deconvolution method was selected because of its easy and low noise [1]. As shown in Figure 3.3, the unknown field distribution parameters $F(r)$ is integrated along the infinitely thin parallel rays, and the integral profile $h(y)$ is expressed as

$$h(y) = \int_{-\infty}^{\infty} F\left[\left(x^2 + y^2\right)^{1/2}\right] dx \tag{3-1}$$

Using the Abel transform, the unknown field distribution $F(r)$ can be inverted analytically from the integral projection data $h(y)$:

$$F(r) = -\frac{1}{\pi}\int_r^{\infty} \frac{h'(y)}{(y^2 - r^2)^{1/2}} dy \tag{3-2}$$

where $h'(y) = dh/dy$. There are several deconvolution techniques available to perform this inversion, such as, Abel inversion methods, onion-peeling, and filtered back-projection methods. However, these three methods are fairly similar [1]. In the actual measurements, the infinite field distribution parameter is replaced with a discrete ring-structure form. As shown in Figure 3.3, the projection data is a trapezoid sum at data spacing Δr. According to the work of Dasch [1], all the deconvolution techniques can be expressed as a linear operator:

$$F(r_i) = \frac{1}{\Delta r}\sum_{j=0}^{\infty} D_{ij} h(r_j) \tag{3-3}$$

where $r_i = i\Delta r$ is the distance from the center of the spray, D_{ij} is the linear operator coefficient and is independent of Δr. Readers can refer to the Ref. [1] for the detailed descriptions of D_{ij}. The light absorption techniques used in this thesis, the unknown $F(r_i)$ can be correlated to the dimensional extinction coefficient K for the soot volume fraction or vapor fuel volume fraction. The soot volume fraction measurements in this thesis were obtained using an Abel inversion method. Using line-of-sight techniques, a mole fraction profile of CH^* and OH^* in a low sooting laminar diffusion could be also obtained [2]. In this thesis, using the line-of-sight light emission of OH^* chemiluminescence, the unknown $F(r_i)$ is only related to the spatially-resolved OH radical distribution. This aspect is discussed in details in Chapter 5.

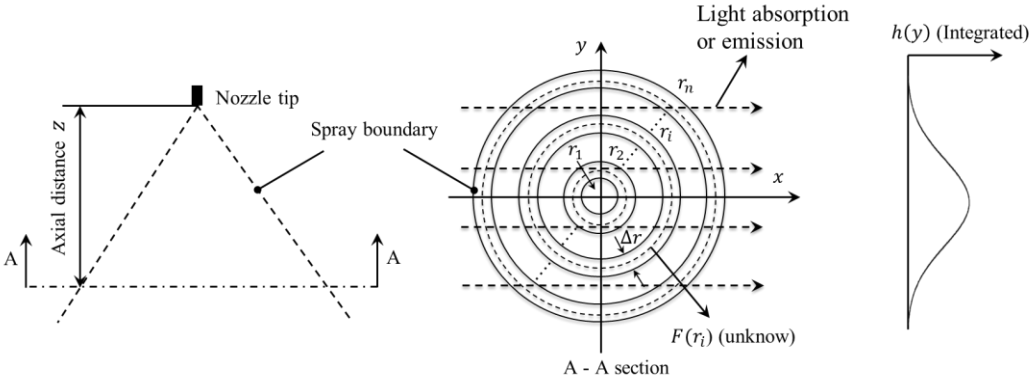

Figure 3.3. Illustration of line-of-sight measurement in a spray.

Using the line-of-sight technique is one approach to obtain the field distribution of spray parameters. The other approach is using planer laser sheet techniques to obtain quantitative measurements directly. The distribution of vapor concentration can be measured by laser induced fluorescence technique [3], laser induced exciplex fluorescence technique [4], and elastic Rayleigh scattering [5]. A compressive review of these techniques are not attempt, and readers recommend to read a review paper [6] for the detailed descriptions. In a reacting diesel jet, it is hard to obtain the quantitative measurements of soot volume fraction. One of the reasons for this is that relatively high soot concentrations which attenuate the incoming laser sheet intensity significantly. However, relatively spatial-resolved soot parameters could be achieved using the planer laser sheet techniques. The relative soot volume fractions were measured using the laser-induced incandescence technique (LII), the relative soot particle sizes were measured by means of obtaining the ratio of laser induced scattering (LIS) intensity to the LII intensity, and the relative soot number densities were obtained as the ratio of the square of LII intensity to the LIS intensity by Kosaka

and co-workers [7]. The optical set-up used by them is shown in Figure 3.4. Using these techniques, low sooting/pure fuels were usually used instead of commercial diesel fuels [7, 8].

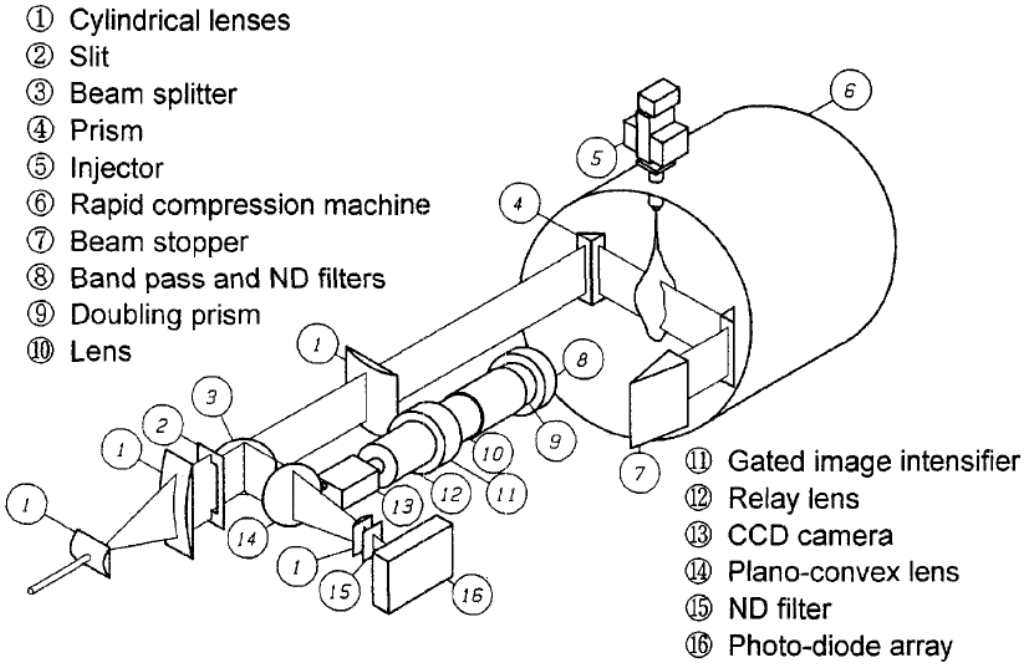

Figure 3.4. Optical set-up for the spatial-resolved soot measurements from the work of Kosaka et al. [7].

3.3 Light absorption technique

Since line absorption techniques were used in this study, the principles of these techniques will be briefly reviewed. A more detailed treatment of light scattering and absorption by small particles is beyond the scope of this thesis, but can be found in Refs. [9-11]. Figure 3.5 depicts the attenuation of light by a cloud of soot particles or fuel vapor. When light beams with an intensity of I_0 pass through the cloud, the transmitted light is attenuated by absorption and scattering. The attenuated light intensity can be calculated using the Beer-Lambert law, defined as

$$I = I_0 \cdot \exp(-(-\int_0^L K\, ds) \tag{3-4}$$

where I_0 is the incident light intensity, K is the local dimensional extinction coefficient, and s is the spatial location along the path length (L) through the soot cloud or vaporized/liquid fuel. For the techniques used in this thesis, such as, laser extinction and light scattering and absorption technique, light absorption makes a much greater contribution to attenuation than does scattering. Laser extinction can be used to measure soot concentrations because soot particles behave like black bodies and strongly attenuate transmitted light. Light absorption and scattering (LAS) measurements were performed using fuels that contain a UV light absorbent, and provide information on the fuel vapor; in this case, the attenuation is due to UV light absorption, and the contribution of scattering can be neglected. The UV absorption of a given hydrocarbon or fuel (e.g. 1-methylnaphthalene in appended Paper IV) depends on its molecular structure; the principles of molecular fluorescence are discussed in detail in Refs. [12, 13] for the detailed description about the principle of light absorption by the molecules. The LAS technique is described at length in appended Paper IV, so no further details are given here.

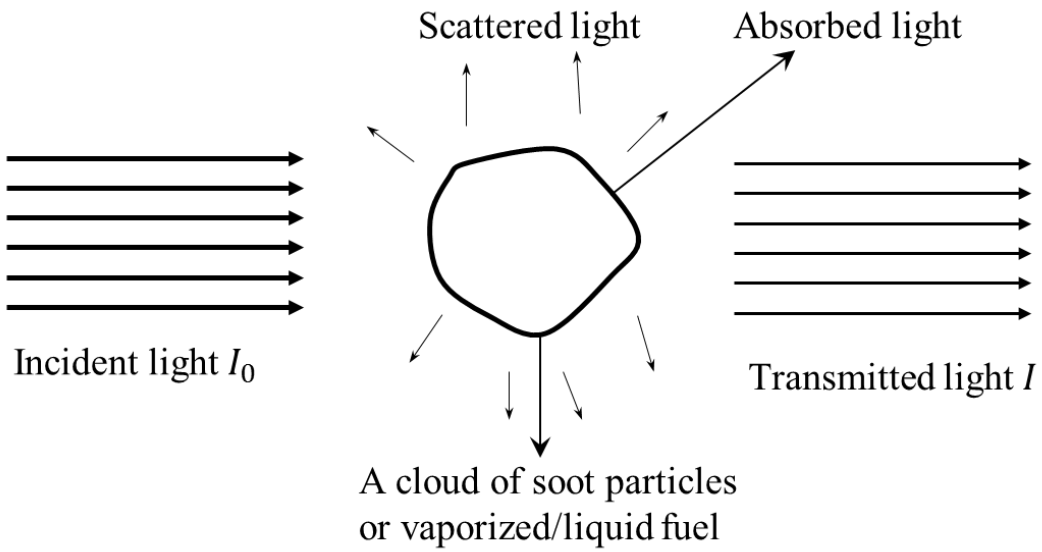

Figure 3.5. Light attenuation by a cloud of soot particles or vaporized/liquid fuel.

3.4 Laser extinction for the soot measurements

Particulate matter is an important air pollutant that is harmful to the environment and human health. Soot is a major component of the particulate matter emitted by diesel engines. One way is to reduce or eliminate these emissions to use a diesel particulate filter (DPF) in the engine aftertreatment system. Another way is to reduce or eliminate the net formation of soot particles within the combustion chamber inside the engine, which requires a detailed understanding of the mechanisms of soot formation. *In situ* soot measurements have been carried out in engines for several decades using various optical measurement methods; the application of optical measurement methods in diesel engines, such as two color pyrometry, laser induced scattering (LIS), and laser induced incandescence (LII) has been reviewed by Zhao and Ladommatos [14]. This section provides a brief overview of the use of two-dimensional laser extinction methods for measuring soot concentrations and soot volume fractions, which is not covered in appended papers V and VI.

The first use of laser extinction to measure soot concentrations under diesel-engine like conditions was performed in the early 1970s [14]. This method is simple and accurate, and can be used even at high soot concentrations (i.e. when the value of $K_e L$ is high), unlike the LII technique, in which the induced laser light can be absorbed strongly by the dense soot particles. In particular, one-point laser extinction measurements provide rather accurate results if the beam steering effect and the contribution of flame luminosity are properly accounted for [15]. Two-dimensional laser extinction offers an advantage over one-dimensional methods because it can be used to measure soot concentrations or volume fractions at multiple points. However, two-dimensional laser extinction measurements under HP/HT conditions are wavelength-dependent because of PAHs and strong beam steering effects. This section discusses these issues, the choice of suitable wavelengths, and ways of minimizing beam steering effects.

The wavelength dependence of the extinction intensity has been studied in well-defined burners to investigate the contribution of PAHs to absorption [16-19]. As shown in Figure 3.6 (adapted from the work of Zerbs et al. [18]), the soot volume fraction (f_V) is overpredicted at shorter wavelengths (i.e. 532 nm and 632.8 nm) because of light absorption by PAHs. In addition, Migliorini et al. [9] observed wavelength dependence for the absorption of non-soot species at wavelengths below 700 nm in premixed atmospheric pressure ethylene/air flames. Similar findings were reported by Simonsson et al. [16].

Therefore, longer wavelengths (over 700 nm) should be used for laser extinction measurements of soot particles. On the other hand, Simonsson et al. [16] also reported that the wavelength dependence of the cross-sectional absorption function ($E(m)$) became weaker as the soot matured, being essentially wavelength independent for mature soot. Moreover, Krishnan et al. [19] found that the dimensionless extinction coefficients K_e and $E(m)$ were relatively independent of the fuel type over a wavelength range of 400–800 nm. This conclusion was based on buoyant turbulent diffusion flames with long residence times that allowed complete soot maturation. This implies that it is appropriate to measure the soot volume fraction using visible wavelengths under mature soot particle conditions or in the absence of PAHs. The works discussed above were performed using well-defined burners. Under diesel-like conditions, Skeen et al. [20] observed that the soot volumes determined using blue light (406 nm) were higher than those measured using green light (519 nm). In this study, a laser beam with a wavelength of 532 nm was used as the light source, and the sooting zone was defined by the flame luminosity area. However, it was possible that PAHs might be present in the sooting zone near the lift-off length. Further investigations will be required to determine how much light absorption by such PAHs contributes to the measured extinction.

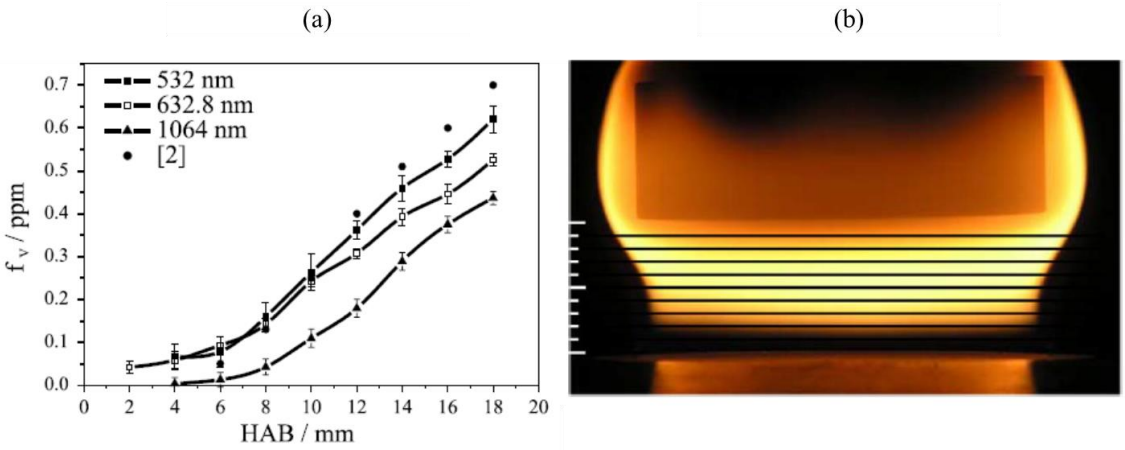

Figure 3.6. Measured soot volume fractions (a) at different wavelengths, and a photo of a C_2H_4/air flame from the work of Zerbs et al. [18]. The reference data with the label [10] in the left-hand figure are from Ref. [21].

Under high pressure ambient conditions, there are steep temperature gradients surrounding the reacting spray. This perturbs the refractive index of the medium, causing the deflected light beam to reflect onto the detector. An early study carried out in a single cylinder engine by Nakakita et al. [22] used a diffuser (a frosted glass plate) to suppress this beam steering effect. Similarly, Manin et al. [23] placed an engineered diffuser with a 50° circular pattern in front of the LED light to suppress the beam steering effect under HP/HT conditions. They claimed that this measure made the contribution of the beam steering effect to the detected light extinction negligible. Thomson et al. [24] conducted an excellent study on methods of reducing beam steering effects. As shown in Figure 3.7 (a), these authors observed ripple and circular structures when using collimated two-dimensional light extinction because of the beam steering effect. To mitigate this effect, Thomson et al. [24] used an integrating sphere to produce a diffuse light. Moreover, a large f-number (~f/40) was chosen to achieve near-parallel light collection from the flame. These measures substantially reduced the beam steering effect, as shown in Figure 3.7 (b). Another interesting finding from the work of Thomson et al. [24] is that, as shown in Figure 3.7 (c), the soot volume fractions measured with two different optical set-ups was nearly identical except for in the region in the edge of flame. This implies that the beam steering effect only introduces uncertainty near the edge of the flame.

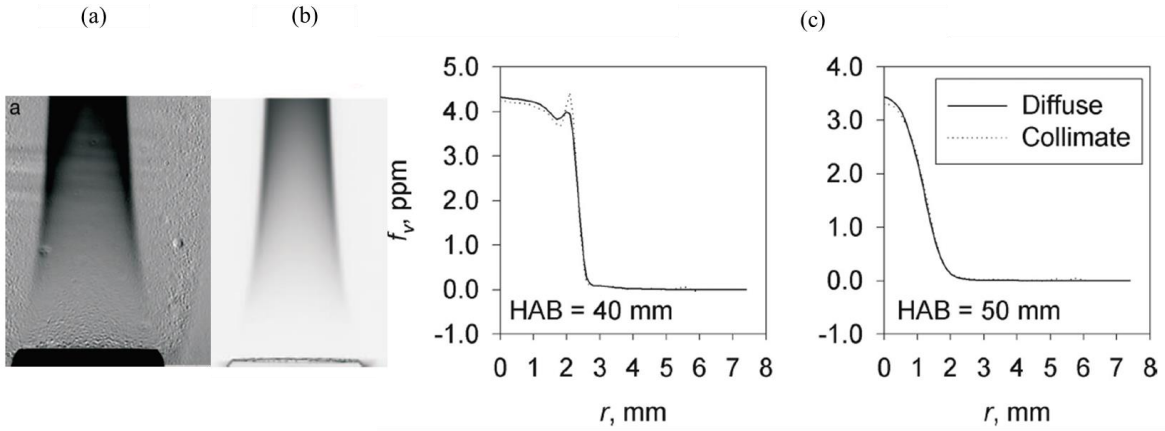

Figure 3.7. Transmissivity image of a sooting flame acquired by collimated two-dimensional light extinction from the work of Snelling et al. [25], (a). Transmissivity image of a sooting flame acquired by diffused two-dimensional light extinction from the work of Thomson et al. [24], (b). A comparison of the soot volume fractions determined using the collimated and diffused two-dimensional light extinction methods from the work of Thomson et al. [24] (c). All flames were formed from non-premixed laminar ethylene-air mixtures.

In this study, a ground glass diffuser (120 grit) was placed in front of the expanded laser beam. This significantly reduced the beam steering effect. In addition, the f-number set in appended paper VI (f/5.6) was greater than that in appended paper V (f/2.8). Therefore, less noise (i.e. beam steering effects) is seen around the sooting region in the soot shadowgraph images included in appended paper VI. Methods for further reducing the beam steering effect were not investigated, and should be prioritized in future work.

References

[1] Dasch, C. J. (1992). One-dimensional tomography: a comparison of Abel, onion-peeling, and filtered backprojection methods. *Applied optics*, *31*(8), 1146-1152.

[2] Walsh, K. T., Long, M. B., Tanoff, M. A., & Smooke, M. D. (1998, January). Experimental and computational study of CH, CH^*, and OH^* in an axisymmetric laminar diffusion flame. In *Symposium (International) on Combustion* (Vol. 27, No. 1, pp. 615-623). Elsevier.

[3] Schulz, C., & Sick, V. (2005). Tracer-LIF diagnostics: quantitative measurement of fuel concentration, temperature and fuel/air ratio in practical combustion systems. *Progress in Energy and Combustion Science*, *31*(1), 75-121.

[4] Melton, L. A. (1983). Spectrally separated fluorescence emissions for diesel fuel droplets and vapor. *Applied Optics*, *22*(14), 2224-2226.

[5] Idicheria, C. A., & Pickett, L. M. (2007). Quantitative mixing measurements in a vaporizing diesel spray by Rayleigh imaging (No. 2007-01-0647). *SAE Technical Paper*.

[6] Fansler, T. D., & Parrish, S. E. (2014). Spray measurement technology: a review. *Measurement Science and Technology*, *26*(1), 012002.

[7] Kosaka, H., Nishigaki, T., Kamimoto, T., & Harada, S. (1995). A study on soot formation and oxidation in an unsteady spray flame via laser induced incandescence and scattering techniques (No. 952451). *SAE Technical Paper*.

[8] Dec, J. E., & Espey, C. (1992). Soot and fuel distributions in a DI diesel engine via 2-D imaging (No. 922307). *SAE Technical Paper*.

[9] Bohren, C. F., & Huffman, D. R. (1983). Absorption and scattering of light by small particles. *John Wiley & Sons*.

[10] Hulst, H. C., & van de Hulst, H. C. (1957). Light scattering by small particles. *Courier Corporation*.

[11] Berrocal, E. (2006). Multiple scattering of light in optical diagnostics of dense sprays and other complex turbid media, *PhD thesis*.

[12] Valeur, B., & Berberan-Santos, M. N. (2001). Molecular fluorescence: principles and applications. *John Wiley & Sons*.

[13] Yadav, L. D. S. (2013). Organic spectroscopy. *Springer Science & Business Media*.

[14] Zhao, H., & Ladommatos, N. (1998). Optical diagnostics for soot and temperature measurement in diesel engines. *Progress in Energy and Combustion Science*, *24*(3), 221-255.

[15] Bejaoui, S., Mercier, X., Desgroux, P., & Therssen, E. (2014). Laser induced fluorescence spectroscopy of aromatic species produced in atmospheric sooting flames using UV and visible excitation wavelengths. *Combustion and Flame*, *161*(10), 2479-2491.

[16] Simonsson, J., Olofsson, N. E., Török, S., Bengtsson, P. E., & Bladh, H. (2015). Wavelength dependence of extinction in sooting flat premixed flames in the visible and near-infrared regimes. *Applied Physics B: Lasers & Optics*, *119*(4).

[17] Migliorini, F., Thomson, K. A., & Smallwood, G. J. (2011). Investigation of optical properties of aging soot. *Applied Physics B: Lasers and Optics*, *104*(2), 273-283.

[18] Zerbs, J., Geigle, K. P., Lammel, O., Hader, J., Stirn, R., Hadef, R., & Meier, W. (2009). The influence of wavelength in extinction measurements and beam steering in laser-induced incandescence measurements in sooting flames. *Applied Physics B: Lasers and Optics*, *96*(4), 683-694.

[19] Krishnan, S. S., Lin, K. C., & Faeth, G. M. (2000). Optical properties in the visible of overfire soot in large buoyant turbulent diffusion flames. *TRANSACTIONS-AMERICAN SOCIETY OF MECHANICAL ENGINEERS JOURNAL OF HEAT TRANSFER*, *122*(3), 517-524.

[20] Skeen, S. A., Manin, J., Dalen, K., & Pickett, L. M. (2013, May). Extinction-based imaging of soot processes over a range of diesel operating conditions. In *8th US National Combustion Meeting*.

[21] Axelsson, B., Collin, R., & Bengtsson, P. E. (2000). Laser-induced incandescence for soot particle size measurements in premixed flat flames. *Applied Optics*, *39*(21), 3683-3690.

[22] Nakakita, K., Nagaoka, M., Fujikawa, T., Ohsawa, K., & Yamaguchi, S. (1990). *Photographic and three dimensional numerical studies of Diesel soot formation process* (No. 902081). SAE Technical Paper.
[23] Manin, J., Pickett, L. M., & Skeen, S. A. (2013). Two-color diffused back-illumination imaging as a diagnostic for time-resolved soot measurements in reacting sprays. *SAE International Journal of Engines*, *6*(2013-01-2548), 1908-1921.
[24] Thomson, K. A., Johnson, M. R., Snelling, D. R., & Smallwood, G. J. (2008). Diffuse-light two-dimensional line-of-sight attenuation for soot concentration measurements. *Applied optics*, *47*(5), 694-703.
[25] Snelling, D. R., Thomson, K. A., Smallwood, G. J., & Gülder, Ö. L. (1999). Two-dimensional imaging of soot volume fraction in laminar diffusion flames. *Applied Optics*, *38*(12), 2478-2485.

Chapter 4

Summary of appended papers

Paper I

The effect of cavitation on the estimation of fuel injection rates based on momentum flux measurements

Chengjun Du, Sven Andersson, Mats Andersson

Submitted to the publication

This paper presents the effect of geometry-induced cavitation on the estimation of fuel injection rates based on momentum flux measurements. The effect of cavitation on the internal flow characteristics was investigated indirectly. As shown by the schematic presented in Figure 4.1 (a), for a cavitating nozzle orifice, the cavitating bubbles induce a non-uniform density and velocity at the orifice exit. To account for this behavior, the cross-sectional area of flow (A_{eff}) is assumed to be smaller than the area of the geometry orifice exit (A_o). In addition, it is assumed that the effective velocity profile (u_{eff}) of the flow through the effective area A_{eff} is uniform, and that the flow density equals the fuel density ρ_f. For a non-cavitating nozzle as shown in Figure 4.1 (b), the velocity profile is largely uniform. It is therefore assumed that the A_{eff} is almost identical to A_o. Under these assumptions, the measured fuel momentum flux was compared to the weighed fuel mass for a cavitating nozzle orifice (cylindrical) and a non-cavitating nozzle (convergent) orifices. The orifice inlets of in both nozzles were with hydro-grinding. Figure 4.2 shows the experimental set-up parts between the force sensor holder and the injector, which is not shown in Figure 2 in Paper I.

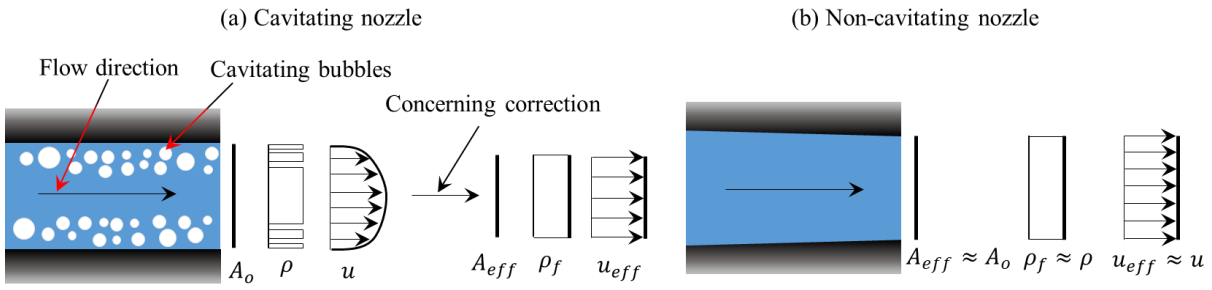

Figure 4.1. Simplified cross-sectional view of flow in the cavitating and non-cavitating nozzle orifices.

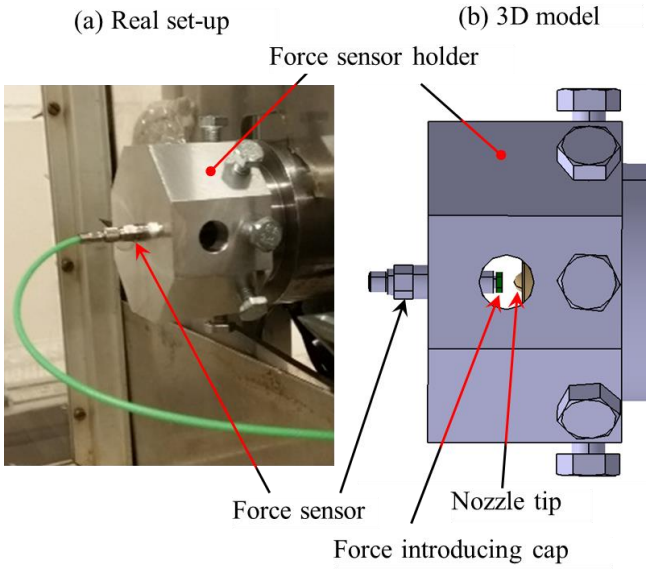

Figure 4.2. Experimental set-up for the momentum flux measurement.

Near-field microscopic images were captured to investigate the influence of cavitation on the liquid jet at the nozzle exit. The width of the liquid jet near the nozzle tip was found to be greater with the cylindrical nozzle (K0) than with the convergent nozzle (K2), as shown Figure 15 in Paper I. This confirmed the occurrence of cavitation inside the cylindrical nozzle orifice. Moreover, as shown in Figure 4.3, it was found that failure to account for cavitation caused the injection rate to be overestimated for the cavitating (cylindrical) nozzle but not for the non-cavitating (convergent) nozzle, validating the assumptions discussed above. We therefore recommend that cavitation should be accounted for when estimating injection rates for cavitating nozzles but not for non-cavitating nozzles. Further, the tendency of a given nozzle orifice to induce cavitation can be evaluated by measuring the nozzle's momentum flux under the assumption of zero cavitation and then comparing the estimated mass of injected fuel to the weighed mass.

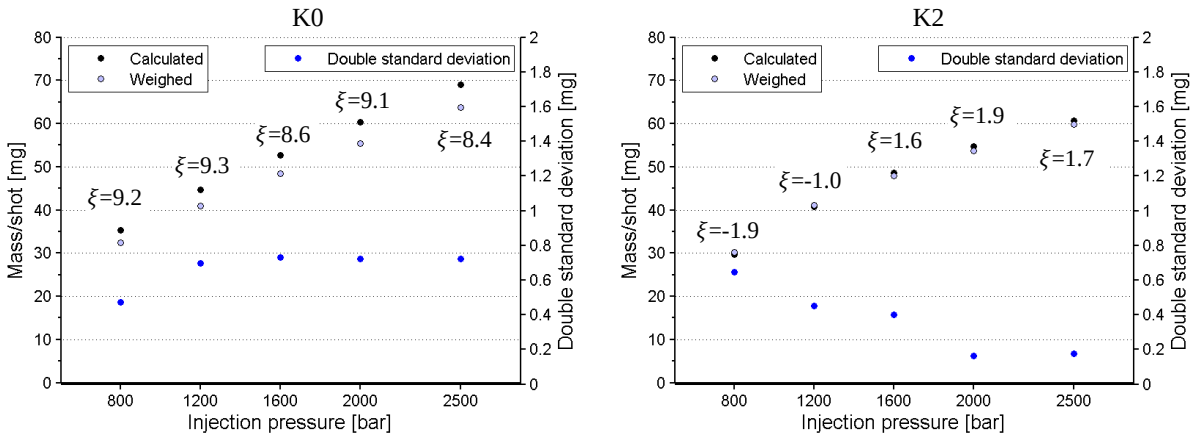

Figure 4.3. Weighed fuel masses (filled black circles) and masses calculated based on the method disregarded the cavitation (open circles) for nozzles K0 and K2. The double standard deviations (2σ) of the calculated mass values and the differences ξ are also shown (filled blue circles).

The author made the experimental plan with the support of Sven Andersson and Mats Andersson. The author performed the experiments, processed and analyzed the data, and wrote the paper with the support of Sven Andersson and Mats Andersson.

The research questions of Paper II and Paper III are discussed in ‘Section 1.3’. Prior to the experiments three nozzles were ordered, and the schematics of internal flow and primary internal orifice structures are shown in Figure 4.4. The illustrated liquid/vapor phase lengths for three nozzles are based on our experimental observations. However, these spray parameters were unknown prior to the experiments, and they would be measured to investigate the effects of nozzle geometry-induced cavitation on the liquid and vapor phase sprays. The ‘Research question (2)’ in ‘Section 1.3’ can be examined using the nozzle N1 and N2. However, this would be not sufficient for validating the ‘Research question (2)’, because the vaporization of the liquid fuel is affected by the fuel mass flow rate. Therefore, the nozzle N3 whose mass flow rate was similar to that of the nozzle N1 was also used. Using these nozzles, the liquid/vapor spray parameters were measured and compared.

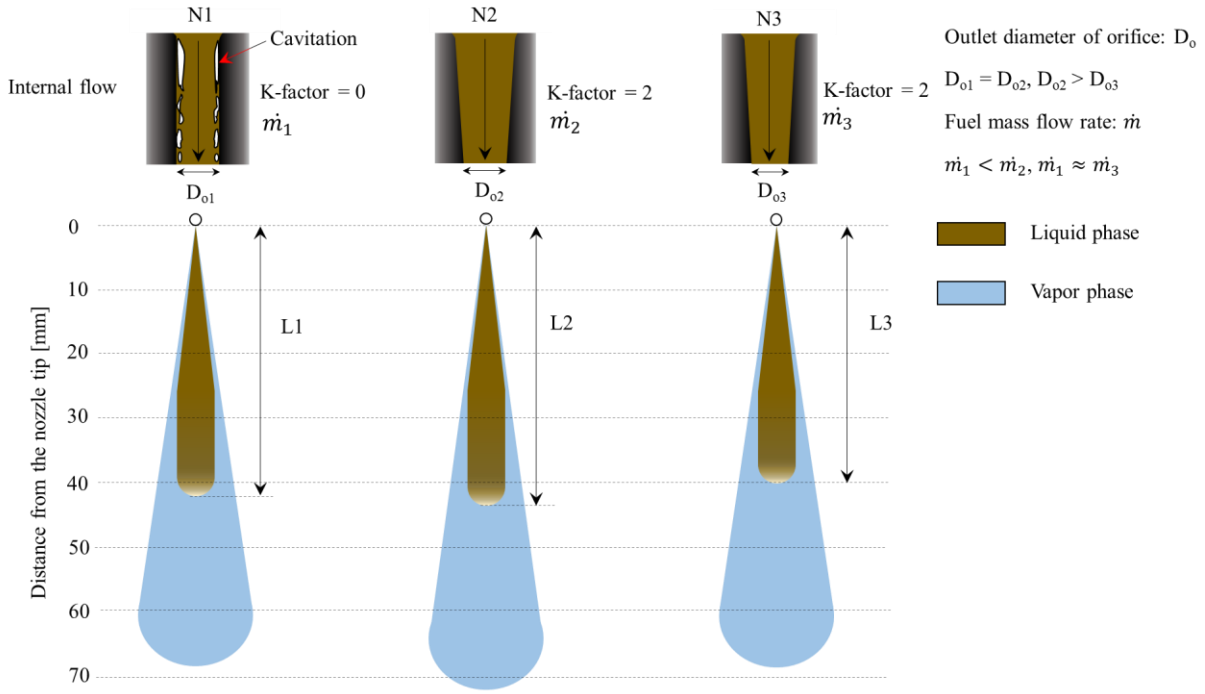

Figure 4.4. Internal flow and liquid/vapor phase sprays for the nozzle N1-N3 used in Paper II and Paper III. L1-L3 are liquid spray length.

Paper II

Effect of Nozzle Geometry on Diesel Spray Characteristics under Non-Evaporating and Evaporating Conditions

Chengjun Du, Mats Andersson, Sven Andersson

Presented the ICLASS 2015, 13th Triennial International Conference on Liquid Atomization and Spray Systems, Tainan, Taiwan, August 23~27, 2015.

In this paper, we investigated effects of nozzle geometry on liquid phase spray characteristics. Since the injection rate and spray properties are affected by the nozzle outlet diameter and k-factor, three different nozzles were used: N1 (outlet diameter 140 µm, k-factor 0), N2 (outlet diameter 140 µm, k-factor 2), and N3 (outlet diameter 136 µm, k-factor 2). Using these nozzles, the momentum flux was measured at ambient pressure, and liquid phase spray images were captured with a high-speed camera were analyzed

under evaporating and non-evaporating conditions. As shown in Figure 4.5 and Figure 4.6, the effects of nozzle geometry on the liquid phase length and local spray cone angle were found to depend on the gas density and injection pressure. Under non-evaporating conditions, cavitation in nozzle N1 (with no conicity) generated sprays with slightly shorter liquid phase length and larger local cone angles than both nozzles N2 and N3 (with conicity) at low density. These differences became more pronounced as the gas density or the injection pressure was increased.

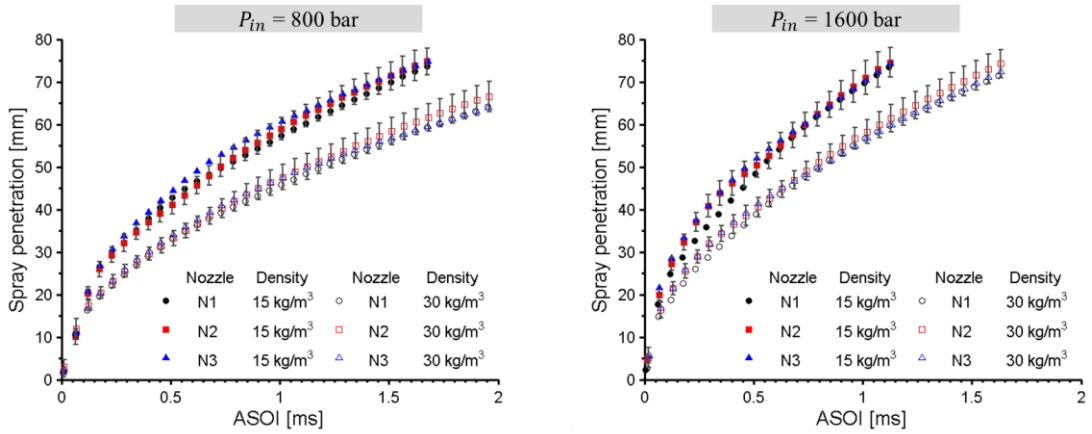

Figure 4.5. Liquid phase spray lengths obtained with each of the nozzles under non-evaporating conditions at ambient temperature 313 K. Error bars show 2σ of mean observations of sprays from nozzle N2.

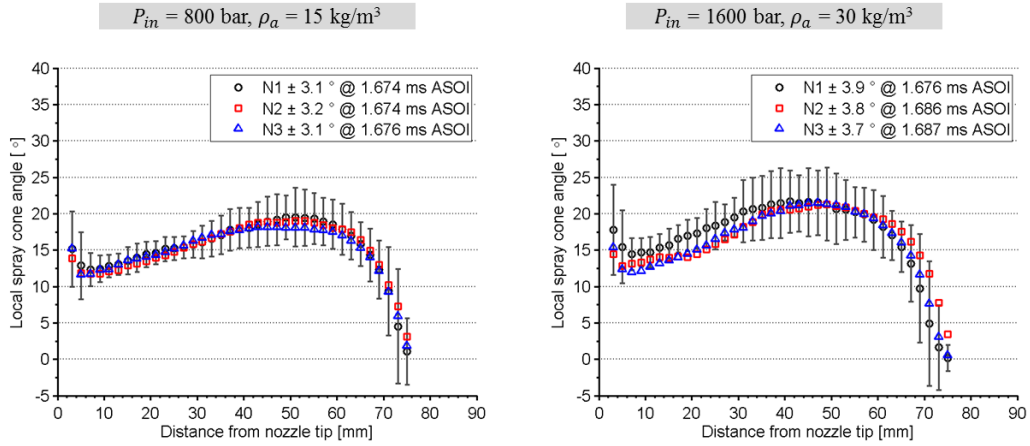

Figure 4.6. Local spray cone angles with nozzles N1-N3 during the steady injection period at ambient temperature 313 K. Error bars show 2σ of mean observations of sprays from nozzle N1, and mean values ± 2σ during the 1-2 ms (steady) period are shown in the legend.

Under evaporating conditions, the measured liquid spray lengths are presented in Figure 4.7. Before explaining the differences in liquid spray lengths between three nozzles, the liquid spray vaporization limited by the mixing process is briefly introduced, which is not covered in Paper II. According to the theory of liquid jet vaporization controlled by the turbulent mixing, the local interphase transport rates of mass, momentum, and energy control liquid jet breakup and the droplet vaporization is fast compared to turbulent mixing rates. In this limit, vaporization of the liquid spray is controlled by the turbulent mixing rate which determines the rate of thermal energy entrained into the spray for heating and vaporizing the liquid fuel. The liquid spray vaporization rate is therefore directly proportional to the gas mass entrainment rate. Applying the conservation of mass and momentum principles, the fuel mass flow rate at any axial distance ($\dot{m}_{f,x}$) and the mass rate of ambient gas entrained into a spray up to any axial distance from the orifice ($\dot{m}_{a,x}$) can be expressed:

$$\dot{m}_{f,x} = \dot{m}_f = \rho_f \cdot u_f \cdot A_f \propto \rho_f \cdot d_o^2 \cdot u_f \tag{4-1}$$

$$\dot{m}_{a,x} = \rho_a \cdot A_x \cdot u_x \propto \sqrt{\rho_a \cdot \rho_f} \cdot d_o \cdot x \cdot u_f \cdot tan(\theta/2) \tag{4-2}$$

where the parameters can be referred to the 'Section 2.3' and the uniform mixture profile shown in Figure 2.10. By the vaporization of liquid spray limited by the mixing, the liquid spray length (L) results from the mass and energy balances at the mixture of fuel and gas. Vaporized liquid fuel at the location (L) reaches a saturated condition in thermodynamic equilibrium with the ambient gas, both with a temperature T_s. At this location, the ratio of fuel and gas mass flow rate can be related to in terms of the specific enthalpies:

$$\frac{\dot{m}_{f,L}}{\dot{m}_{a,L}} = \frac{h_a(T_a, P_a) - h_a(T_s, P_a - P_s)}{h_f(T_s) - h_f(T_f, P_a)} \tag{4-3}$$

where P_s is the partial pressure of the vapor fuel at the saturation temperature T_s, and $P_a - P_s$ is the partial pressure of the entrained ambient gas. The enthalpy difference in the denominator is the specific enthalpy required to heat and vaporize the liquid fuel. The enthalpy difference in the numerator is the specific enthalpy transferred from the entrained ambient gas to heat and vaporize the fuel. It can be seen clearly from Equation (4-3) that the liquid spray length is directly related to the ambient gas entrainment rate. The differences in liquid phase length between three nozzles as shown in Figure 4.7 are due to the differences of the fuel mass flow rate and the air entrainment rate: nozzle N3 yielded shorter liquid phase length than nozzle N1, due to lower mass flow rates; nozzle N2 yielded longer liquid phase length than nozzle N1, partly because nozzle N2 provided higher mass flow rates, and partly because of higher air entrainment rate (due to larger local spray angle) in nozzle N1. This observation supports the liquid spray evaporation controlled by the mixing.

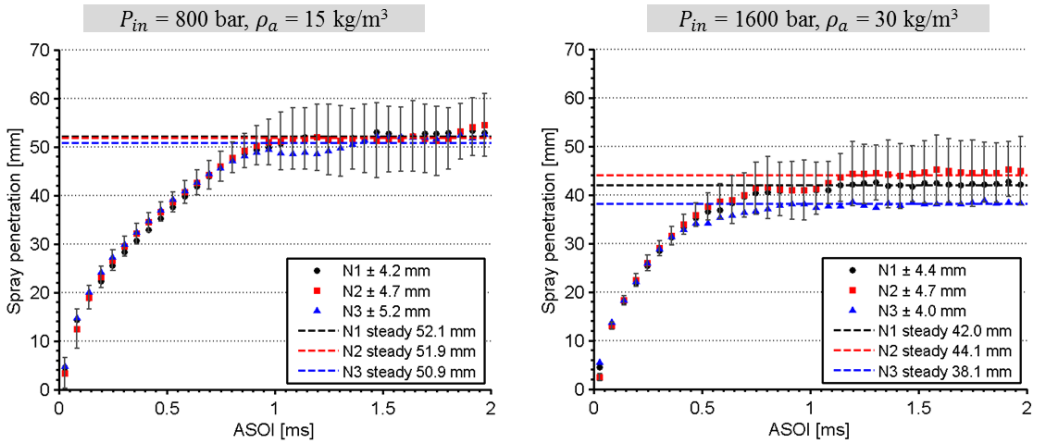

Figure 4.7. Spray penetration lengths obtained with nozzles N1-N3 under evaporating conditions (673 K ambient temperature). Error bars show 2σ of mean observations of sprays from nozzle N2. Mean penetration values (dashed lines) and means ±2σ during the 1-2 ms (steady) period are shown in the legend.

Sven Andersson, Mats Andersson and the author made the experimental plan. Mats Andersson was responsible for the optical set-up, and the author was responsible for the fuel injection system. The author processed and analyzed the data, and wrote the paper with the support of Sven Andersson and Mats Andersson.

Paper III

Effects of Nozzle Geometry on the Characteristics of an Evaporating Diesel Spray

Chengjun Du, Mats Andersson, Sven Andersson

Presented SAE 2016 International Powertrains, Fuels & Lubricants Meeting, Baltimore, Maryland, USA, October 24-26, 2016.

This paper is a continuation of Paper II and used the same nozzles. It presents time-resolved light absorption and scattering (LAS) measurements of the distribution of vapor sprays formed under evaporating conditions. It was found that the LAS technique with high-speed video recording was sufficient to qualitatively measure the vapor phase distribution of diesel sprays formed from a commercial diesel fuel. The cylindrical nozzle N1 (which has a high tendency towards cavitation) produced greater local cone angles than the convergent nozzles N2 and N3 in the upstream region of the vapor spray. Figures 4.8 shows the fuel volume fraction along the spray center line between the three nozzles. From the Equations (2-9) and (2-10), it can be seen that the centerline fuel volume fraction $\bar{X}_{f,c}$ is proportional to C_a, d_o and $1/tan(\theta/2)$. The nozzle N1 showed lower $\bar{X}_{f,c}$ than nozzle N2, due to larger spreading angle and smaller C_a in nozzle N1. The N3 showed similar or slightly lower $\bar{X}_{f,c}$ than nozzle N1, due to smaller d_o and spreading angle (see detailed explanation in Paper III) in nozzle N3. The differences in $\bar{X}_{f,c}$ between three nozzles were well explained by the one-dimensional transient diesel spray model. This justified describing the vaporization of the diesel spray as being controlled by turbulent air mixing. The effects of nozzle geometries on the spray properties were mainly due to differences in the fuel mass flow rate, spray momentum and spreading angle.

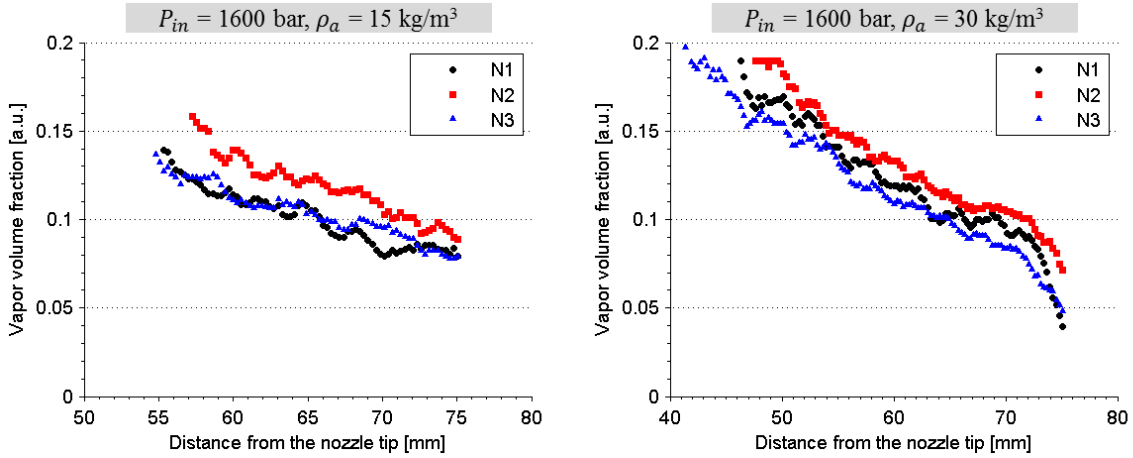

Figure 4.8. Relative vapor volume fraction along a line passing the center of spray based on averaged UV images. All images are selected at 2.0 ms ASOI, and the start distance is from the averaged steady liquid phase length. Ambient temperature 673 K.

Sven Andersson, Mats Andersson and the author made the experimental plan. Mats Andersson was responsible for the optical set-up, and the author was responsible for the fuel injection system. The author processed and analyzed the data together with Mats Andersson, and wrote the paper with the support of Sven Andersson and Mats Andersson.

Paper IV

Time-Resolved Liquid and Vapor Phase Distribution Measurement in Diesel Sprays Using a Light Absorption Scattering Technique

Chengjun Du, Sven Andersson, Mats Andersson

Presented ILASS – Europe 2016, 27th Annual Conference on Liquid Atomization and Spray Systems, Brighton, UK, September 4-7, 2016.

This paper showed that the LAS technique with continuous light sources can be used to measure time-resolved liquid and vapor distributions. Pure n-dodecane fuel mixed with tracer compounds (2% and 10% 1-methylnaphthalene (1-MN)) were used as model fuels. As shown in Figure 4.9, it was found that the details of the development of the liquid and vapor phase distribution could be captured clearly using UV and visible light, and using both fuel blends. The light extinction tended to be saturated in UV images acquired with the 10% 1-MN fuel at various ambient temperatures. However, no saturation was observed with the 2% 1-MN fuel.

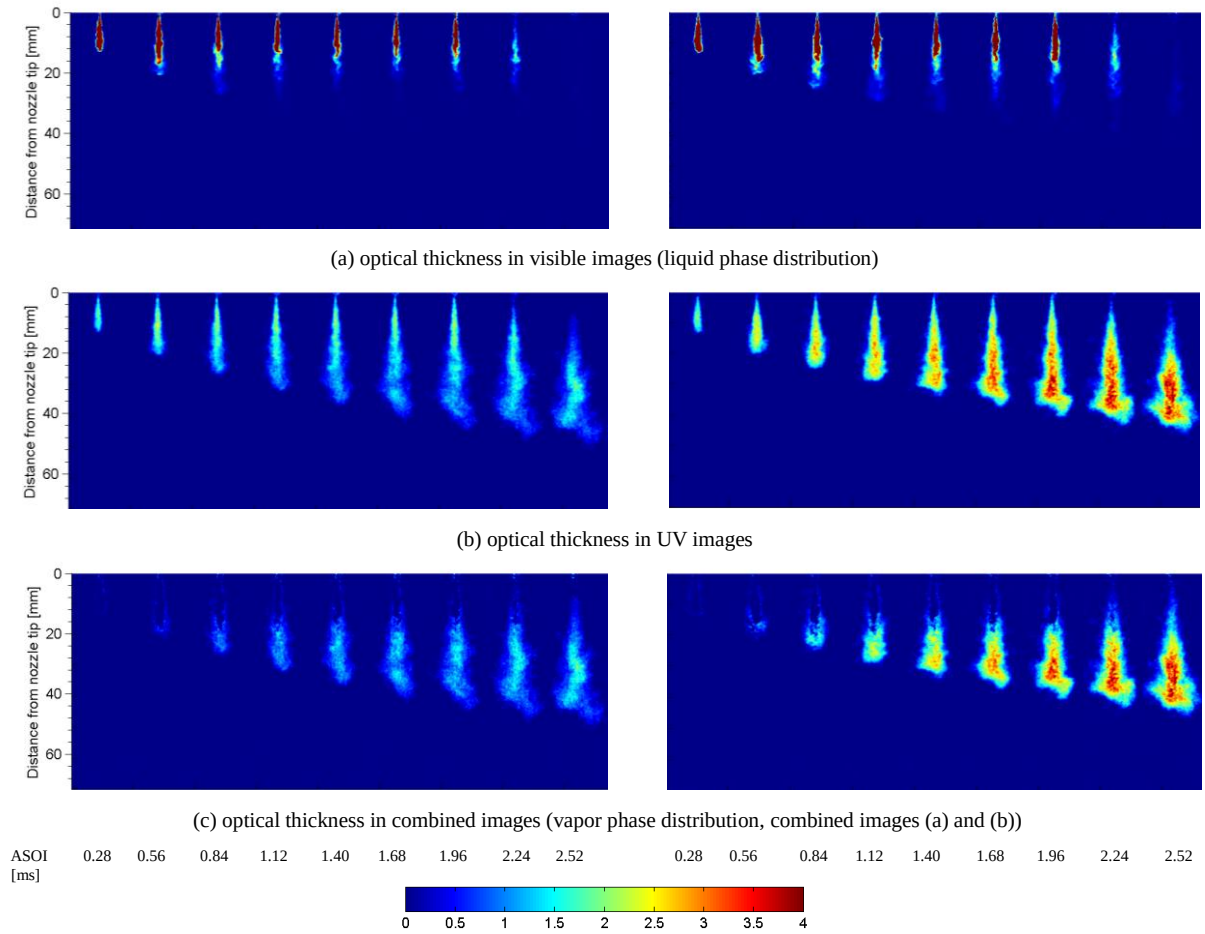

(a) optical thickness in visible images (liquid phase distribution)

(b) optical thickness in UV images

(c) optical thickness in combined images (vapor phase distribution, combined images (a) and (b))

Figure 4.9. Time-resolved liquid and vapor phase distribution using 2% 1-MN (left) and 10% 1-MN (right). Conditions: ambient temperature 563 K, ambient gas density 36 kg/m^3, injection pressure 800 bar

Mats Andersson made the experimental plan and performed the experiments. The author processed and analyzed the data together with Mats Andersson, and wrote the paper with the support of Mats Andersson.

The research questions of Paper V and Paper VI are discussed in 'Section 1.3'. In fact, the analytical methods used in Paper V were stimulated by the experimental results found in Paper V. Figure 4.10 shows the schematics of the OH^* chemiluminescence and sooting zone boundaries based on experimental observations. As shown in Figure 4.10 (a), the radial profile of OH^* chemiluminescence is independent of the injection pressures, and only the lift-off length moves to the downstream of jet as the injection pressure increases. However, as shown in Figure 4.10 (b), the boundary of sooting zone decreases in radial and axial directions as the injection pressure increases. This raises a question: what is the gap between the OH^* chemiluminescence and sooting zone boundaries in the radial direction? To seek the answers, the local equivalence ratio was predicted, and OH radical distribution was obtained. These two factors were correlated to the reduction of the soot formation and to the reduction of the sooting zone in radical direction. Detailed results and discussions are in appended Paper V. The experimental findings in Paper V are only based on a fixed nozzle outlet dimeter of 0.14 mm and a fixed ambient gas density, in which the soot concentrations were relatively low. This raises a question: whether if this finding will be influenced by the higher/lower soot concentration conditions? To seek this answer, experiments were carried out with a big nozzle orifice diameter (0.19 mm) and a small one (0.10 mm), and the gas density was varied. This study is appended in Paper VI.

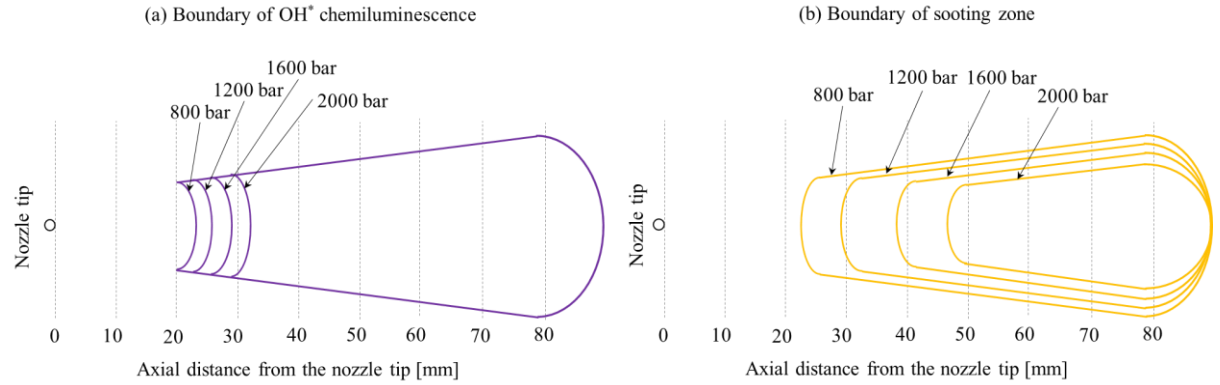

Figure 4.10. Schematics of OH^* chemiluminescence and sooting zone boundaries at different injection pressures.

Paper V

Soot formation and oxidation in a turbulent diffusion diesel flame: the effect of injection pressure

Chengjun Du, Sven Andersson, Mats Andersson

Submitted to the publication

This paper describes the use of an optically accessible HP/HT rig fitted with a single-hole nozzle injector (outlet diameter: 140 μm) to study the effect of the injection pressure on soot development in diesel flames at a gas density of 25.8 kg/m^3, a temperature of 823 K, and injection pressures of 800-2000 bar. The two-dimensional laser extinction method was used to measure the soot concentration and soot volume fraction. We demonstrated that the beam steering effect could be substantially reduced by using a ground glass diffuser, and the sooting zone in the soot shadowgraph images was successfully identified by analyzing natural flame (or soot) luminosity images. OH^* chemiluminescence images were acquired simultaneously with the laser extinction measurements, and the OH^* chemiluminescence images were reconstructed to delineate the distribution of OH radicals using Abel inversion. In addition, the local

equivalence ratio was predicted using the variable mixture profile model. As shown in Figure 4.11, it was found that the lift-off increased with the injection pressure, expanding the size of the low equivalence ratio region in which the high temperature reaction occurs. Consequently, the high temperature reaction zone (and the OH radical zone) were enlarged. This ultimately reduced the soot volume fraction within the jet. The sooting region's width declined in the soot formation region and in the downstream parts of the jet as the injection pressure increased. This implies that soot formation is reduced in the radial direction. The reduced soot formation in the radial direction is due to the widening of the high temperature reaction zone (i.e. the region containing OH radicals). The vortex in the jet head entrained oxygen around the sooting region, and soot particles were oxidized by high temperature reactions in the jet head. That is, the soot particles were attacked by the OH radicals that were formed.

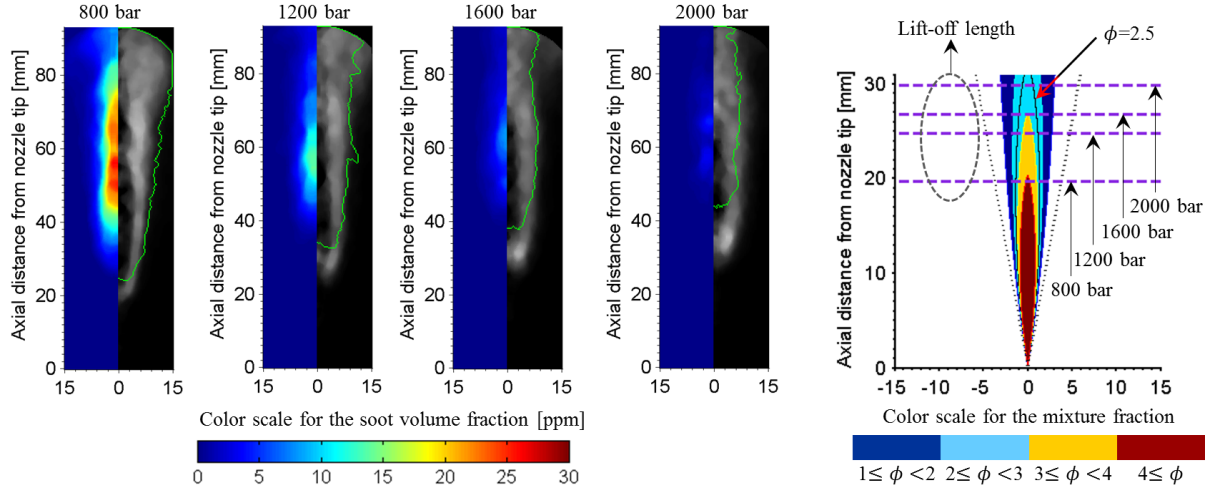

Figure 4.11. Soot volume fraction and reconstructed OH^* CL images recorded during the steady combustion phase at different injection pressures. The left-hand images in each pair show the soot volume fraction obtained using three-point Abel inversion from the averaged KL factor images. The right-hand images in each pair show the reconstructed OH^* CL images with the boundaries of the sooting zone indicated by green lines. All images were recorded at 3.704 ms ASOI. The graph on the right of the figure shows the predicted equivalence ratio ϕ in the lift-off region given an assumed spreading angle of 21.6°.

Mats Andersson, Sven Andersson and the author made the experimental plan, and Mats Andersson and the author planned the optical set-up. During the experiments, Mats Andersson was responsible for the optical set-up and the author was responsible for the fuel injection system. The author processed and analyzed the data, and wrote the paper with the support of Sven Andersson and Mats Andersson.

Paper VI

Two-dimensional measurements of soot in a turbulent diffusion diesel flame: the effects of injection pressure, nozzle orifice diameter and gas density

Chengjun Du, Sven Andersson, Mats Andersson

Submitted to the publication

This paper is a continuation of Paper V, and uses the same optical and analytical methods. Experiments were performed at a constant ambient temperature of 823 K and two gas densities (20, 26 kg/m^3), with

injection pressures of 800-2500 bar using injectors with nozzle orifices having diameters of 0.19 mm and 0.10 mm. It was found that the equivalence ratio in the jet center at the lift-off length (ϕ_{CL}) played a critical role in soot formation because it was generally slightly higher than the threshold value of 2.0 required for soot formation to proceed. Reductions in ϕ_{CL} thickened the OH zone in the upstream region of the jet, causing a reduction in the volume corresponding to the maximum soot volume fraction. The expansion of the OH zone also helped reduce the sooting zone's width. However, as shown in Figure 4.12, under high sooting conditions (e.g. ϕ_{CL}>3.5), the sooting zone width in the downstream region of the jet was independent of ϕ_{CL}. For non-sooting jets, the OH zone thickness peaked just downstream of the lift-off length. The location of maximum soot volume fraction in the jet depended on the nozzle orifice diameter, and was closer to the nozzle tip for the smaller orifices than for the larger ones.

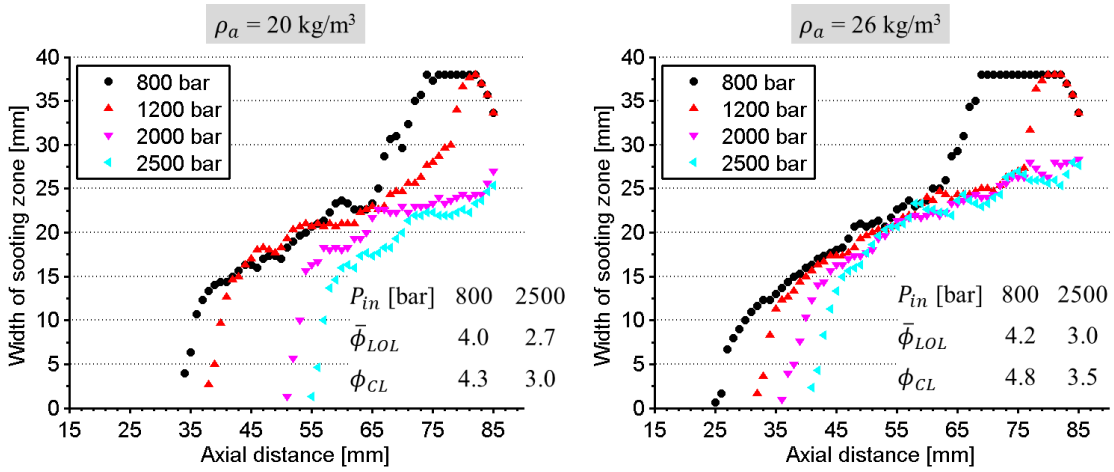

Figure 4.12. Sooting zone width for the nozzle orifice diameters of 0.19 mm. The predicted $\bar{\phi}_{LOL}$ and ϕ_{CL} are also shown under injection pressures of 800 and 2500 bar.

Mats Andersson, Sven Andersson and the author made the experimental plan, and Mats Andersson and the author planned the optical set-up. During the experiments, Mats Andersson and the author were responsible for the optical set-up, and the author was responsible for the fuel injection system. The author processed and analyzed the data, and wrote the paper with the support of Sven Andersson and Mats Andersson.

Paper VII

The Influence of Ethanol Blending in Diesel fuel on the Spray and Spray Combustion Characteristics

Chengjun Du, Mats Andersson, Sven Andersson

Presented SAE 2014 International Powertrains, Fuels & Lubricants Meeting, Birmingham, United Kingdom, October 20-23, 2014.

This paper described the influence of blending ethanol with Diesel fuel on sprays and spray combustion characteristics under non-evaporating, evaporating, and combusting conditions. Three fuels were investigated: (1) Diesel - a European Diesel based on the EN590 standard; (2) E10 - a blend of Diesel containing 10% ethanol and 2% emulsion additive; and (3) E20 - a blend of Diesel containing 20% ethanol and 2% emulsion additive. It was found that the differences in the fuels' composition did not significantly affect the liquid phase spray penetration or the cone angle under non-evaporating or evaporating conditions. However, under combusting conditions, E10 and E20 had longer ignition and soot formation delays than Diesel. As shown in Figure 4.13, as the ethanol content of the fuel was increased from 0% to 20%, the lift-off length increased and the detectable soot luminescence decreased. This indicates that soot formation declines as the fuel's ethanol content increases.

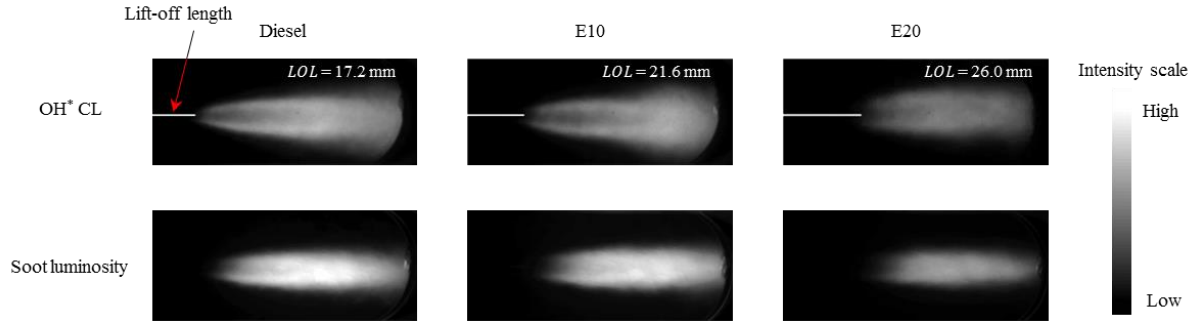

Figure 4.13. OH^* chemiluminescence and soot luminosity averaged images. Lift-off lengths (white line and value in the right upper side of the image). The left starting point of the white line corresponds to the nozzle tip. Experimental conditions: ambient temperature 873 K, gas density 24.3 kg/m^3 and injection pressure 1350 bar. Images are averaged under steady combusting period for each fuel.

Sven Andersson, Mats Andersson, and the author made the experimental plan. Mats Andersson was responsible for the optical set-up, and the author was responsible for the fuel injection system. The author processed and analyzed the data with the support of Mats Andersson and Sven Andersson, and wrote the paper with the support of Sven Andersson and Mats Andersson.

Chapter 5

Unpublished findings – OH^* chemiluminescence investigation

Two-dimensional line-of-sight OH^* chemiluminescence images were used extensively to analyze the experimental data presented in appended papers V, VI and VII. For hydrocarbon fuels undergoing stoichiometric combustion, the high temperature reaction produces excited OH radicals (OH^*). The primary kinetic path for OH^* formation is the exothermic reaction $CH+O_2 \rightarrow CO+OH^*$ [1]. Once formed, OH^* returns rapidly to its ground state through chemiluminescent emission and collisional quenching. OH^* emits light at wavelengths around 310 nm as it undergoes radiative relaxation to a lower energy state; this can be used to identify regions of high heat release and the flame front. Measurement of the OH^* chemiluminescence emission (referred to as OH^* CL for brevity below) intensity requires only a band pass filter with an appropriate detector, e.g. a photomultiplier tube or an intensified camera. Because it is so simple to measure, the OH^* CL signal has been extensively used in premixed combusting flames [2-6] and diesel combustion spray studies [7-12]. In lean premixed turbulent flames, although the turbulence intensity, strain rate, and curvature have a strong impact on the chemiluminescence intensity, a spatially resolved heat release rate can be determined by measuring the intensity of OH^* CL with a correction method applied [5]. However, this would be challenging for diesel flames because of high turbulence, signal trapping and strong soot incandescence.

In a turbulent premixed flame, OH^* CL is not the only source of light at wavelengths around 310 nm. Figure 5.1 shows a typical chemiluminescence spectrum of a non-preheated, turbulent methane-air flame at atmospheric pressure. As can be seen, CO_2^* emissions contribute to the measured light intensity in the OH^* CL wavelength range. In general, the collected light intensity in the OH^* CL wavelength range does not directly reflect the concentration of OH^*.

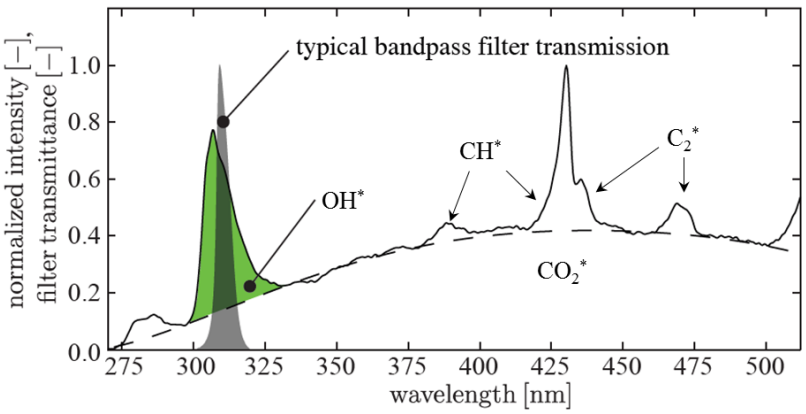

Figure 5.1. A typical chemiluminescence spectrum of a methane-air flame. The OH^* CL emissions are superimposed on those from CO_2^* (adapted from the work of Lauer [13]).

For sooting diesel flames, both CO_2^* and soot incandescence contribute to observed light emissions in the OH^* CL wavelength range. Soot particles act as black bodies, and their contribution is due to black body

radiation. Figure 5.2 depicts the method used to measure the line-of-sight OH* CL intensity in a sooting diesel flame. If one considers the flame as a three-dimensional entity, the OH*CL intensity from the jet's left edge is strongly absorbed by soot particles or PAHs in the jet center, so this part of OH* CL intensity is unlikely to be captured by the detector. In addition, the OH* intensity in the jet's upper and lower edges may be trapped to some extent by OH radicals [2]. The light collected at the detector will ultimately be equal to the sum of the light from these different regions.

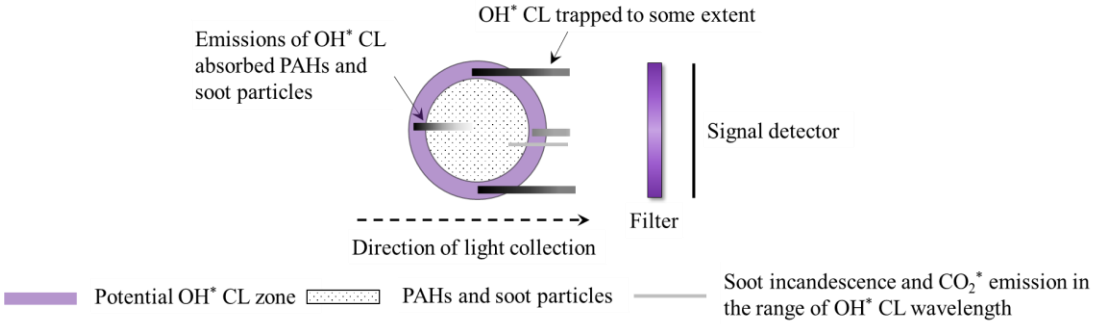

Figure 5.2. Cross-sectional view of the system for line-of-sight OH* CL imaging.

Despite the difficulties of recording the OH* CL intensity, several research groups have disregarded soot incandescence and the absorption of OH* CL in sooting flames [7, 9, 11] because they concluded that OH* CL emission is the dominant contributor in the OH* CL wavelength range. Appended paper V shows that the OH* CL intensity in the jet center is lower than at the jet edges. This could be partially because OH* CL emissions to the left of the center are artificially suppressed by soot absorption (see Figure 5.2). On other hand, there is less interference due to soot particles at the jet edges, leading to longer integrated OH* CL path lengths. The relationship between the contribution of soot incandescence and the absorption of OH* CL intensity by soot particles in the jet center is not well characterized. To address this issue, OH* CL images were collected from the side view in addition to the normal view; the optical set-up used for this purpose is shown in Figure 5.3. Spectroscopic data were acquired simultaneously with OH* CL images; the slit of the light collection window was ~1.5 mm thick and ~58.5 mm above the nozzle tip.

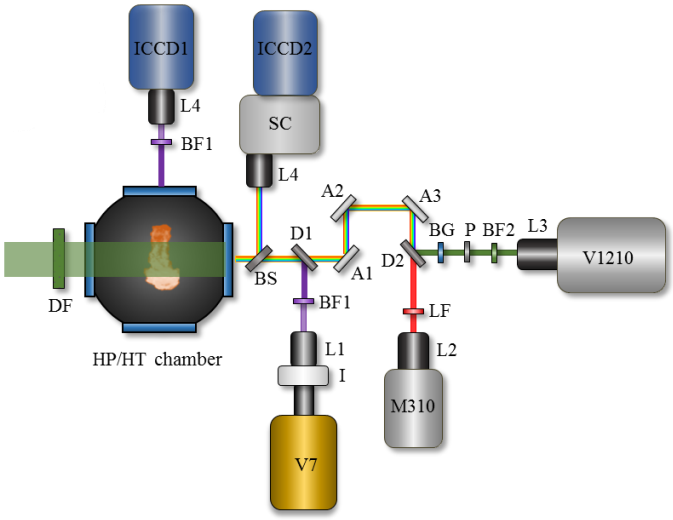

Figure 5.3. Schematic of the optical setup. DF: 120 grit ground glass diffuser, BS, UV beam splitter, D1: dichroic mirror (DM) with ≥ 96% reflectance at 308 nm, D2: longpass DM with >95% reflectance at 500-560 nm, A1-A3: aluminum mirrors, BF1: bandpass filter (BF) 307±10 nm, LF: longpass filter OG570, BG: BG39, P: polarizer, BF2: 532±1.5 nm, L1: Nikon UV lens fl=105mm, f/2, L2-3: Nikon lens, fl=105mm, f/2, I: Image intensifier. V7, M310 and V1210 are Phantom high speed video CMOS cameras, L4: UV lens, SC: spectroscopy, ICCD: LaVision intensified CCD camera.

The same narrow band pass filter was used in front of the ICCD1 and V7 cameras. Although the gate time and gain numbers were set differently for ICCD1 and the intensifier, this should not influence the qualitative interpretation of the effect of OH* absorption by soot particles and soot incandescence on OH* CL images. Figure 5.4 shows OH* CL images taken from two directions: the side-on OH* CL image was taken using the ICCD1 camera, and the normal OH* CL image was taken using the V7 camera. All images in Figure 5.4 are averaged over 5 injections acquired at the same time after injection. The black lines overlaid on the OH* CL images are contour lines corresponding to a KL factor of 0.5 in the corresponding KL factor images. Interestingly, the image structure and light intensity distribution in the OH* CL side and normal images are very similar; the OH* CL intensity is relatively low in the jet center and high near the jet periphery. If there was no absorption of OH* CL by soot particles in the jet center, one would expect similar OH* CL intensities in the center and periphery. In addition, the OH* CL intensities are significantly different between the side (high soot concentration) towards the jet center and the side outwards (low soot concentration) the jet center near the overlaid black line. If one assumes that the integrated path lengths of the OH* CL emissions are nearly identical on both sides, the difference in their OH* CL intensities must be due to strong absorption of OH* CL emissions by soot particles in the jet.

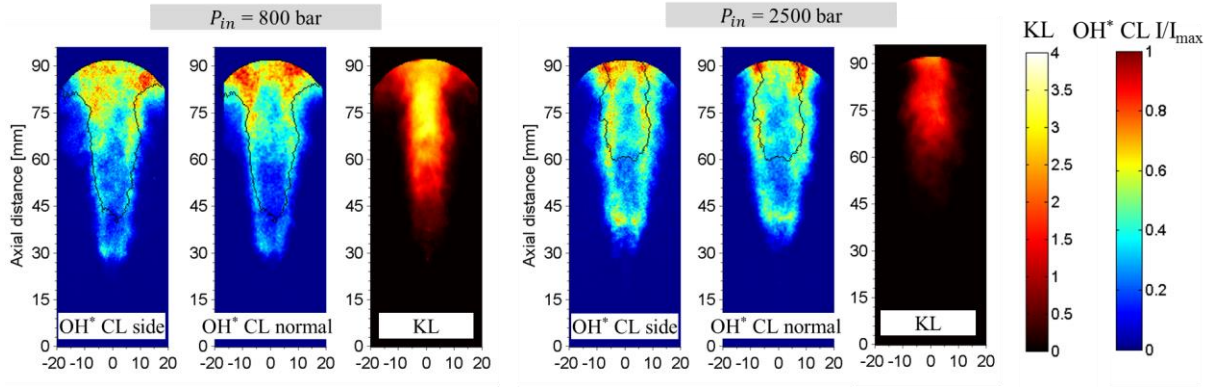

Figure 5.4. Side-on and normal OH* CL images overlaid with black lines enclosing all pixels with a KL factor above 0.5 in the corresponding KL factor images. Color scales for the OH* CL and KL images are shown on the far right. Experimental conditions: nozzle hole diameter 0.19 mm, ambient temperature 823 K, gas density 20 kg/m^3, 3.67 ms ASOI.

The contribution of soot incandescence and CO_2* emissions in the OH* CL wavelength range can be evaluated using the spectrum graph shown in Figure 5.5. The spectrum is integrated along the slit line in the radial direction as shown in Figure 5.5 (a), and the collected spectral intensities were corrected using the known irradiance of a standard tungsten lamp. As seen in Figure 5.5 (a), the soot incandescence and CO_2* emissions dominate over a wide wavelength range at all injection pressures. However, in the OH* CL emission range around 310 nm, the light intensity is around 3-4 times greater than the background intensity due to soot incandescence and CO_2* emissions at an injection pressure of 2500 bar. At an injection pressure of 800 bar, the background intensity of soot incandescence and CO_2* emissions around 310 nm is comparable to the OH* CL intensity because of the jet's high soot concentration. It should be noted that CO_2* emissions also contributes to the wide wavelength range seen in the spectra for high temperature reactions, as shown in Figure 5.1. In addition, as shown in Figure 5.4, the OH* CL intensity in the jet center is relatively low, where there is a maximum soot concentration in the jet center. It implies that the contribution from soot incandescence to the OH* CL images is relatively small.

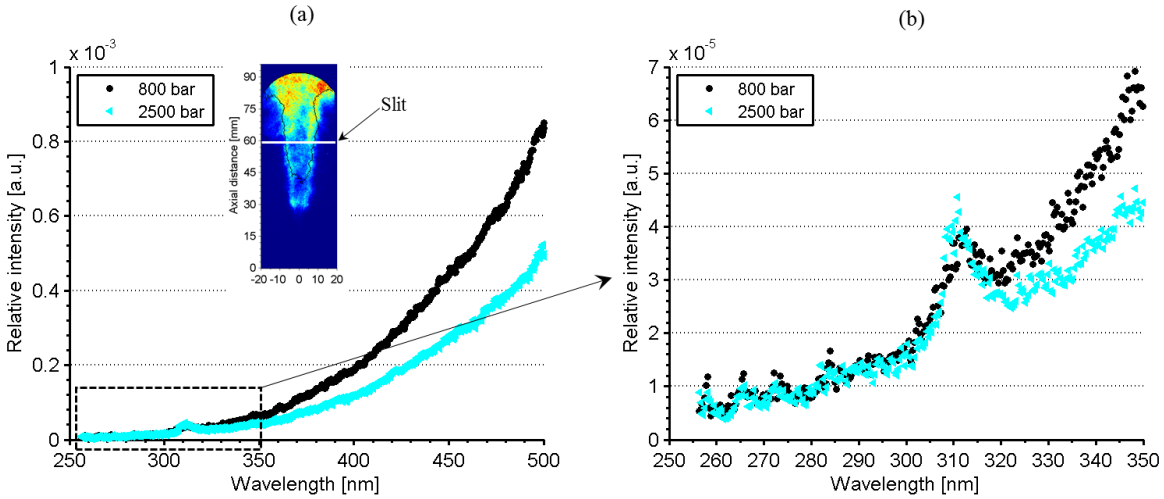

Figure 5.5. Integrated spectral intensity as a function of the wavelength at different injection pressures. (a): intensities over a wide range of wavelengths, (b) expansion of the region between 250 and 350 nm from figure (a). The position of the slit used to collect the emitted light is shown in the inset of figure (a). The experimental conditions are the same as those specified in the caption of Figure 5.4.

References

[1] Gaydon, A. G. "The spectroscopy of flames," 2nd. *Chapmann and Hall, London*, 1974.

[2] Sadanandan, R., Meier, W., & Heinze, J. (2012). Experimental study of signal trapping of OH laser induced fluorescence and chemiluminescence in flames. *Applied Physics B: Lasers and Optics*, 106(3), 717-724.

[3] Worth, N. A., & Dawson, J. R. (2012). Tomographic reconstruction of OH* chemiluminescence in two interacting turbulent flames. *Measurement Science and Technology*, *24*(2), 024013.

[4] Kojima, J., Ikeda, Y., & Nakajima, T. (2000). Spatially resolved measurement of OH*, CH*, and C2* chemiluminescence in the reaction zone of laminar methane/air premixed flames. *Proceedings of the Combustion institute*, *28*(2), 1757-1764.

[5] Lauer, M., Zellhuber, M., Sattelmayer, T., & Aul, C. J. (2011). Determination of the heat release distribution in turbulent flames by a model based correction of OH* chemiluminescence. *Journal of Engineering for Gas Turbines and Power*, *133*(12), 121501.

[6] Higgins, B., McQuay, M. Q., Lacas, F., Rolon, J. C., Darabiha, N., & Candel, S. (2001). Systematic measurements of OH chemiluminescence for fuel-lean, high-pressure, premixed, laminar flames. *Fuel*, *80*(1), 67-74.

[7] Jakob, M., Hülser, T., Janssen, A., Adomeit, P., Pischinger, S., & Grünefeld, G. (2012). Simultaneous high-speed visualization of soot luminosity and OH* chemiluminescence of alternative-fuel combustion in a HSDI diesel engine under realistic operating conditions. *Combustion and Flame*, *159*(7), 2516-2529.

[8] Pauls, C., Gruenefeld, G., Vogel, S., & Peters, N. (2007). Combined simulations and OH-chemiluminescence measurements of the combustion process using different fuels under diesel-engine like conditions (No. 2007-01-0020). *SAE Technical Paper*.

[9] Zhang, J., Jing, W., & Fang, T. (2012). High speed imaging of OH* chemiluminescence and natural luminosity of low temperature diesel spray combustion. *Fuel*, *99*, 226-234.

[10] Maes, N., Meijer, M., Dam, N., Somers, B., Toda, H. B., Bruneaux, G., ... & Manin, J. (2016). Characterization of Spray A flame structure for parametric variations in ECN constant-volume vessels using chemiluminescence and laser-induced fluorescence. *Combustion and Flame*, *174*, 138-151.

[11] Klein-Douwel, R. J. H., Donkerbroek, A. J., Van Vliet, A. P., Boot, M. D., Somers, L. M. T., Baert, R. S. G., ... & Ter Meulen, J. J. (2009). Soot and chemiluminescence in diesel combustion of bio-derived, oxygenated and reference fuels. *Proceedings of the Combustion Institute*, *32*(2), 2817-2825.

[12] Siebers, D. L., & Higgins, B. (2001). Flame lift-off on direct-injection diesel sprays under quiescent conditions (No. 2001-01-0530). *SAE Technical Paper*.

[13] Lauer, M. R. W. (2011). Determination of the heat release distribution in turbulent flames by chemiluminescence imaging, *PhD Thesis*. Technische Universität München.

Chapter 6

Outlook

During the author's PhD studies, optical diagnostic methods were used to perform a wide range of experiments. Optical diagnostics play a key role in enabling *in situ* measurements of sprays' physical properties, which can enhance the understanding of spray processes and their dependence on operating conditions. This chapter focuses on two issues: the outlook for the future development of optical diagnostic methods, and the influence of operating conditions on spray processes.

We have demonstrated the feasibility of using the time-resolved LAS technique to characterize vaporized sprays. The advantages of LAS techniques are high signal-to-noise ratios, low ambient temperature dependence and no fluorescence quenching. Moreover, it was shown that this technique can be used to perform vapor phase spray measurements even with commercial diesel fuels that contain UV light absorbents. In the most recent experimental campaign, a brighter light source was successfully applied, yielding noticeable improvements in the signal-to-noise level. However, this method has not yet reached a point at which it can be used for quantitative measurements. This is because the absorption coefficient was not measured at the studied UV wavelength, which would require the design of a sample cell that can be used under HT/HP conditions. In addition, it would be necessary to perform calibration measurements on vaporized fuel sprays formed with a known mass of injected fuel. Once the results of these measurements become available, it will be possible to use the LAS technique developed in our lab to quantitatively measure the mass of fuel vapor, and the local fuel equivalence ratio using a tomographic inversion algorithm method.

The two-dimensional laser extinction method developed in this work was successfully used to measure f soot concentrations and soot volume fractions. The laser light wavelength used in this work was 532 nm, which can be absorbed by PAHs. In particular, there is relatively high uncertainty in the data for the region downstream of the lift-off length, where soot particles co-exist with PAHs. To avoid interference due to PAHs, longer wavelength laser beams are preferred, such as commercially available 600 - 800 nm beams. Although the soot volume fraction was calculated using the Abel inversion method, the uncertainty in the calculated soot volume fraction was not determined. To clarify this, a point laser beam could be set up to calibrate the soot volume fraction at specific points in sooting jets. In addition, we observed that the use of camera lenses with smaller apertures (i.e. larger f-numbers) reduced the impact of beam steering effects. The effects of beam steering could be analyzed in more detail using simple ray tracing [1], which would provide robust theoretical guidelines on configuring optical equipment for two-dimensional laser extinction measurements.

In the appended papers V and VI, the OH radical distribution was predicted based on OH^* chemiluminescence images by using the Abel inversion method. The possibility of using this method in this way was only recently discovered [2], and we implemented it to better understand the effects of operating conditions on soot formation and oxidation. However, it should be noted that this approach has not yet been validated in our lab; we are currently investigating its general applicability and robustness.

This will be done by using OH planar laser induced fluoresce (OH PLIF) to investigate the correlation between the OH radical distribution and the OH^* CL images obtained after Abel inversion. We also predicted the spreading angle of the reacting spray using the penetration lengths determined from OH^* CL images, and accounted for the reduced air entrainment at the lift-off length in the variable mixture profile. To better understand the differences between reacting and non-reacting jets, the spreading angle and penetration can be measured for both jet types at the same gas densities. In addition, the penetration for the reacting jet can be predicted by using the one-dimensional transient approach in a way that accounts for the properties of reacting jets [3] – specifically, the effect of heat release.

Appended paper I discusses the limitations of the method of measuring transient mass flow rates based on momentum flux measurements. It would be interesting to compare the temporal variation in the mass flow rate recorded using a standard injection rate meter to flow rate measurements based on momentum flux measurements. This would reveal and help explain differences between the two methods, and allow the effects of cavitation on flow rate measurement to be investigated further.

It was also demonstrated that soot-free reacting jets could be formed by using a small nozzle hole coupled with high injection pressures. However, the use of small nozzle holes reduces the fuel mass flow rate. This drawback can be overcome by increasing the number of holes in the nozzle. In addition, it was reported [4] that both nitrogen oxides (NO_x) and soot emissions were considerably reduced in a single cylinder engine using an injector with very small and numerous orifices and a redesigned combustion system. This approach could be investigated in the spray chamber using a nozzle with two small holes. So far, optical combustion experiments have only been performed using a single injection and without wall impingement. However, modern diesel engines use multiple injections during a working cycle. Moreover, reacting jets interact strongly with the cylinder and piston walls. These aspects could be investigated in the future. Finally, this work is based solely on experimental work and one-dimensional models. Three-dimensional numerical simulations could provide valuable complementary data, yielding information on the details of the studied sprays' structures and the evolution of the spray processes.

References

[1] Westlye, F. R., Penney, K., Ivarsson, A., Pickett, L. M., Manin, J., & Skeen, S. A. (2017). Diffuse back-illumination setup for high temporally resolved extinction imaging. *Applied Optics*, 56(17), 5028-5038.

[2] Maes, N., Meijer, M., Dam, N., Somers, B., Toda, H. B., Bruneaux, G., ... & Manin, J. (2016). Characterization of Spray A flame structure for parametric variations in ECN constant-volume vessels using chemiluminescence and laser-induced fluorescence. *Combustion and Flame*, *174*, 138-151.

[3] Desantes, J. M., Pastor, J. V., García-Oliver, J. M., & Pastor, J. M. (2009). A 1D model for the description of mixing-controlled reacting diesel sprays. *Combustion and Flame*, 156(1), 234-249.

[4] Inagaki, K., Mizuta, J., Fuyuto, T., Hashizume, T., Ito, H., Kuzuyama, H., & Kono, M. (2011). Low emissions and high-efficiency diesel combustion using highly dispersed spray with restricted in-cylinder swirl and squish flows. *SAE International Journal of Engines*, *4*(2011-01-1393), 2065-2079.